

()

/ /

ان الهدف الأساسي من إدارة الموارد إمداد ودعم عمليات الموقع بالموارد اللازمة بحيث يمكن تحقيق التوقيتات المطلوبة تسليم الأعمال فيها وكذلك الوصول الى التكلفة الواقعية في حدود الموازنة المقدرة . يهدف البحث إلى معرفة الفائدة من استخدام نظم المعلومات الجغرافية في إدارة الموارد كأحد الأدوات الجديدة التي تواكب التطور الحاصل في مختلف دول العالم وأيضاً جمع الكم الهائل من البيانات المكانية المتعلقة بالموارد في بيئة واحدة يسهل التعامل معها والوصول إليها بسرعة وهذه يساعد على اتخاذ القرار السليم فيما يتعلق بالموارد في مشاريع التشييد المختلفة . إن عملية استخدام نظم المعلومات الجغرافية في إدارة الموارد وتحديد لها أهمية بالغة في عملية التخطيط والبرمجة وإدارة وكلفة الموارد ومن ثم عملية متابعة الكلفة والوقت لمشاريع التشييد المختلفة كما وان واقع الحال يوشح حالة ملحة لاستخدام أدوات جديدة تساعد عملية إدارة المشاريع ضمن منهاج واضح وسليم وتقييم مدى الاستفادة من تلك الأدوات في ضوء ما هو متوفر في ذلك المجال .

ونتيجة للخطوات المتبعة في تطبيق منهجية البحث تم التوصل إلى إثبات مدى الفائدة من استخدام نظم المعلومات الجغرافية بتحسين إدارة وتخطيط الموارد للمشاريع المختلفة مما يساعد على تقليل عمر المشروع ويساعد أيضاً على السرعة في التنفيذ ويهيئ بيئة جيدة لإدارة الكم الهائل من البيانات المكانية ضمن مكان واحد يسهل التعامل معها وتحديثها . لذا من الضروري تطوير ثقافة إدارة المشاريع الإنشائية والاستفادة من الطرق والأساليب والتقنيات الحديثة في محاولة للالحاق بركب التطور الحاصل في مجال التشييد في العالم.

Use of Gis for Creating a Project Management Data Base in Baghdad Al-Rissfa

Assist. Prof.: Dr. Sawsan Rasheed Mohammed
University of Baghdad
College of Engineering
Department of Civil Engineering

Ayad abdulamer shaqate
University of Baghdad
College of Engineering
Department of Civil Engineering

Abstract

The main objective of resources management is to supply and support the site operation with necessary resources in a way to achieve the required timing in handing over the work as well as to achieve the cost-realism within the budget estimated. The research aims to know the advantage of using GIS in management of resources as one of the new tools that keep pace with the evolution in various countries around the world also collect the vast amount of spatial data resources in one environment easily to handled and accessed quickly and this help to make the right decision regarding management of resources in various construction projects.

The process of using GIS in the management and identification of resources is of extreme importance in the process of planning, programming, management and cost of resources and therefore a scientific follow-up cost and time to projects construction different as that fact indicates

an urgent need to use new tools to help the process of projects within clear curriculum and assess the benefit of those Tools according to what is available in the same field

As a result of the steps used in the application of research methodology it has been achieved to prove the benefit of using geographic information systems for better management and resource planning for various projects which help to reduce the duration of the project and help Italy national on the speed-up the execution and provides a new environment for the management of the vast quantity of spatial data in one place which make it easy to handle and to update. It is therefore necessary to develop a culture of management of construction projects and take advantage of the methods and techniques and modern ways in an attempt to catch up with progress in the field of Construction in the world

-1

-2

-3

-1



() ()
 (1995)
 (1995) -2

(Software & Hardware)

-3

-4

(2005)

(GIS)(Geographical Information Systems)

:

(1986)

-:

-: (Bolstad, Paul2003) .

- 1

(1992)

-2

-3

-4

(GIS)

(2005) .

(Software)

(Database

-2

(M.Y.Cheng,and C.Y. Yang,2001)

(2005)

-:

(H.W.G.Meyer,and A.P.Vonderohe,1993)

-1

(C.V.Camp,and

(M.C.Brown,1993

-3

(TFs)

(Cheng,and,J.T.O Connor,1996)

Arcsite

(TFs)

(DBMS)



-4

(M.Y.Cheng and,

C.Y.Yang.2001)

-7

(V.K.Bansal.2007)

-:

-5

(M.Y. Cheng and, J.C.Chen.2002

()
() (

(Global positioning system) (GPS)

-6

(K.Varghese,and,J.T.O Connor,1995

()
() (

)

(

-

-3

()

:

:

-1)

(

()

:

(Arc info 9.3) -1

(1)

1-1

(ESRI)

15 (GPS 72) -2

:

Fid

()

)

()

(

()

(2)

2-1

()

()

()

(Fid)

()

()

()

:(3)

3-1

()

()

Fld

()

()

:

-2

()

)

()

(



(6) . -2) (GPS
 (7) . -3 ((decimal degrees)
 (8) . -4

:() -3

)

(4

:

-1

(5,9)

FID	Shape					

(1)

ID	Shape				

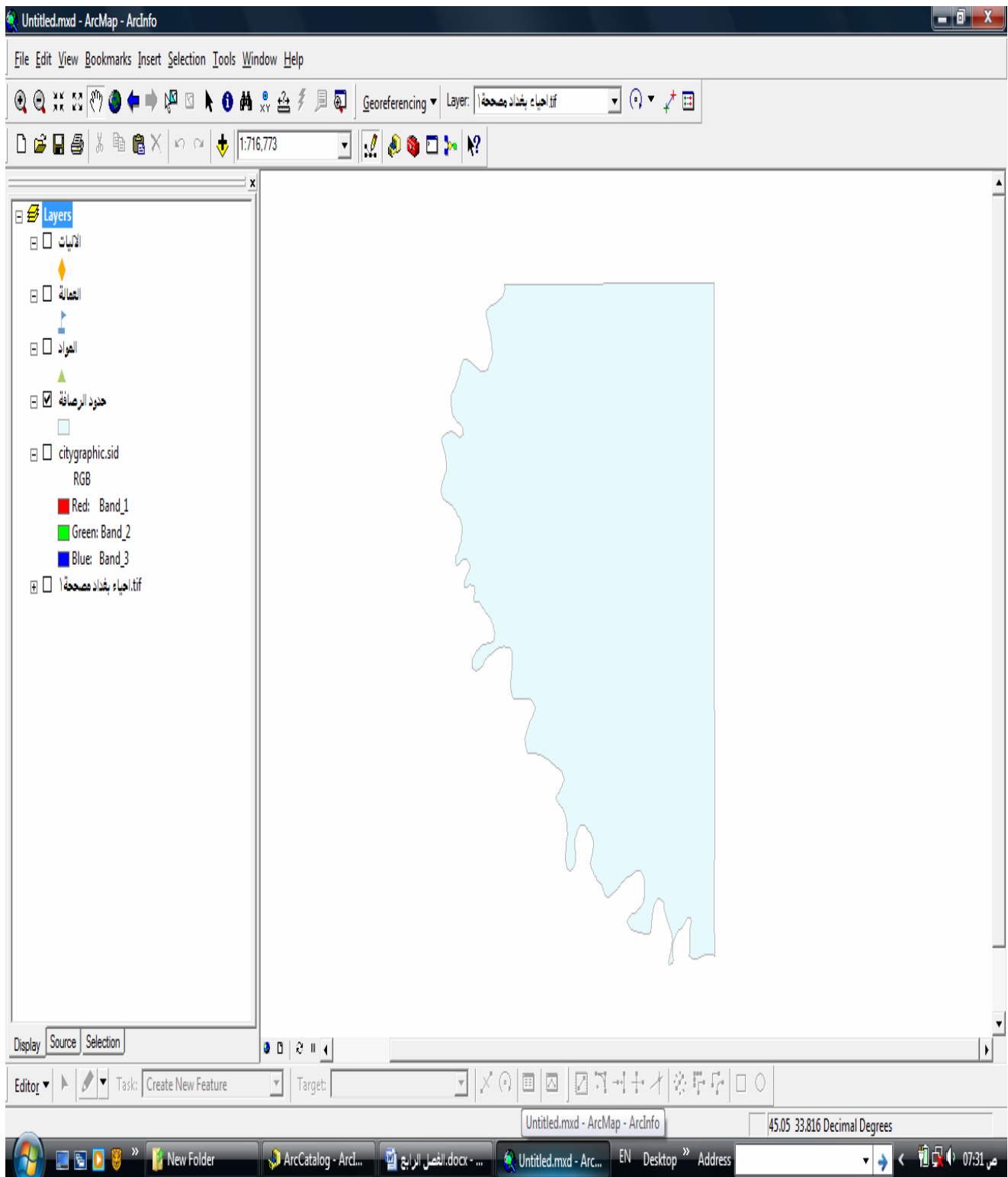
(2)

FID	Shape				

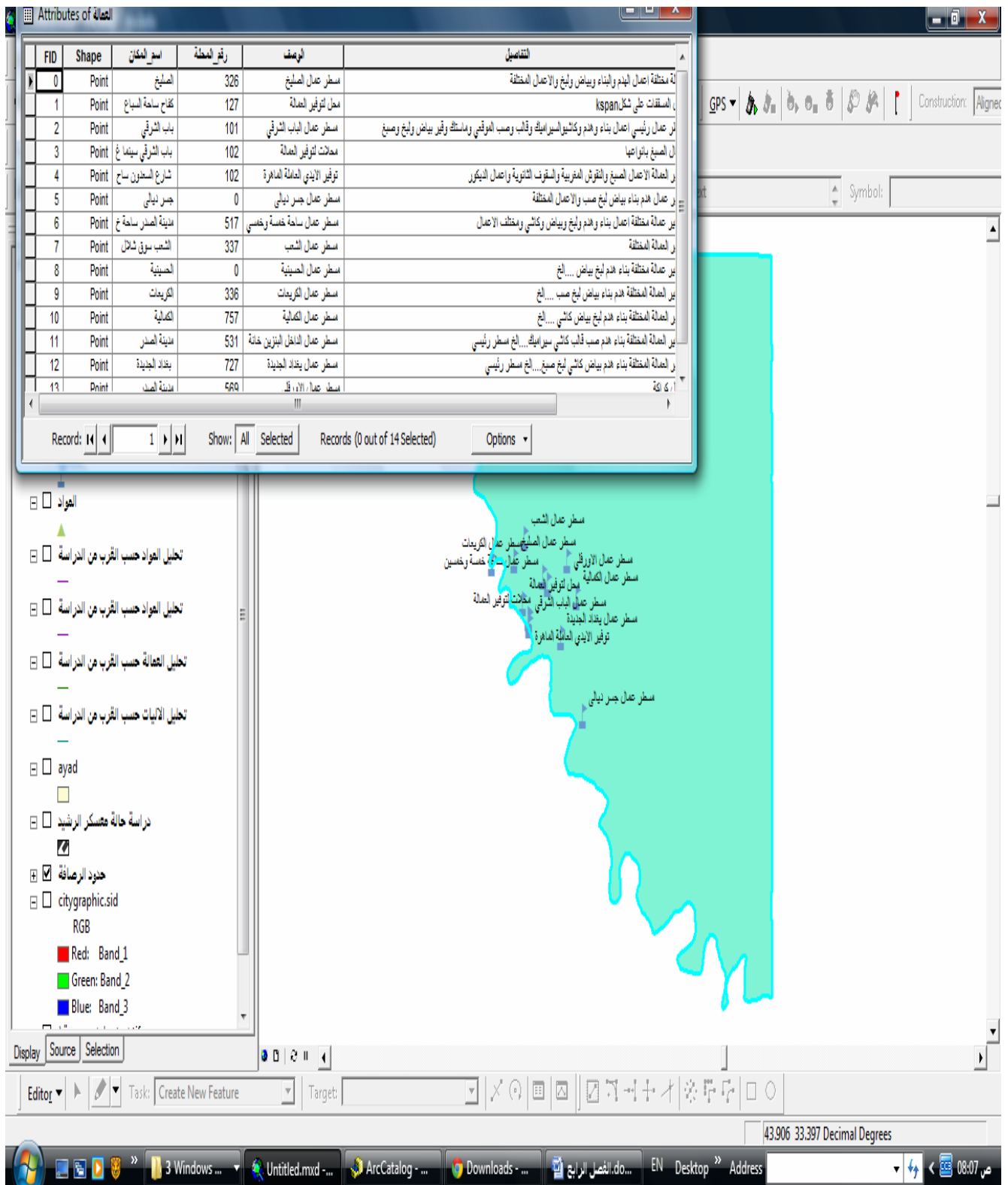
(3)



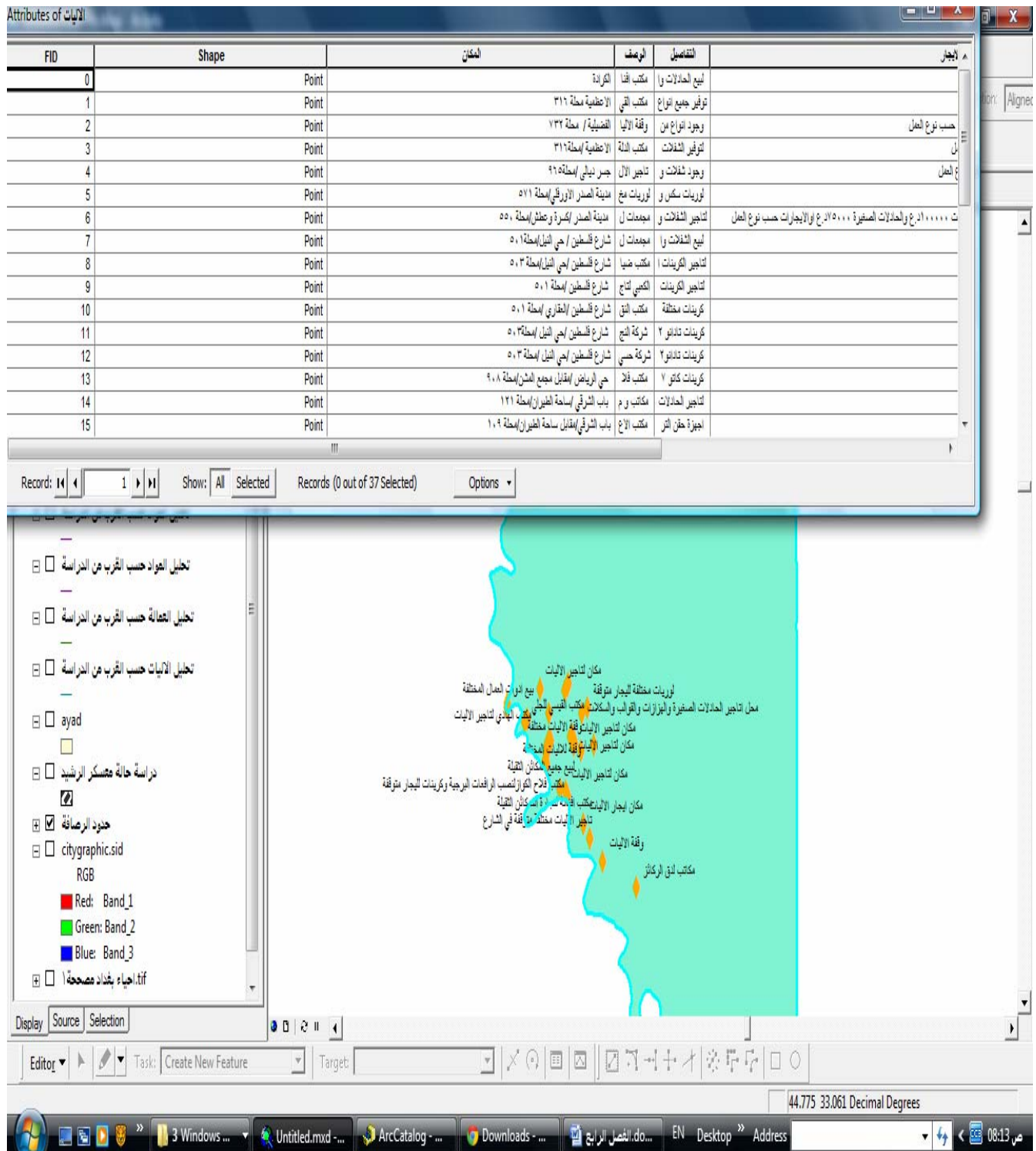
(4)



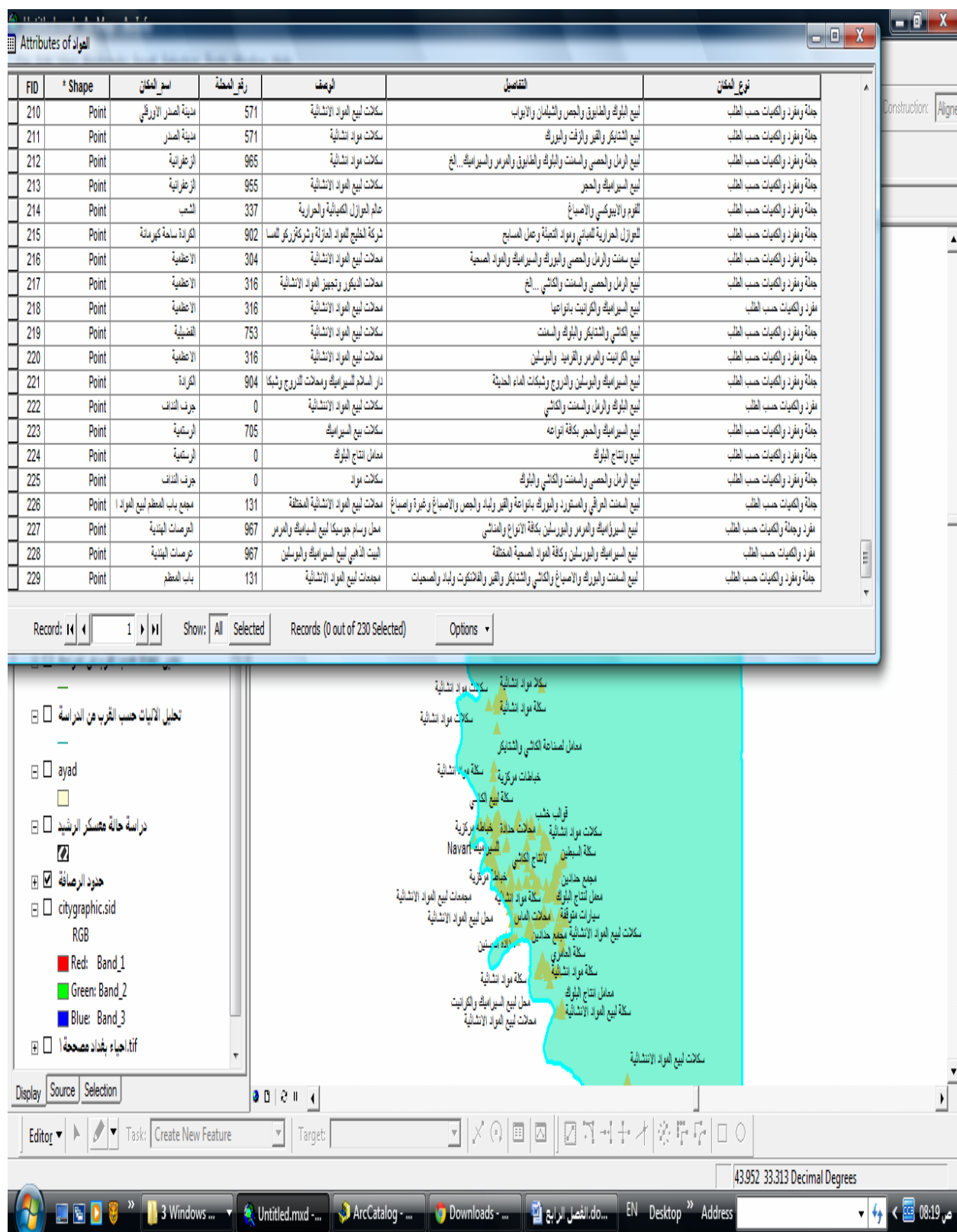
(5)



(6)



(7)



(8)



:

()

()

()

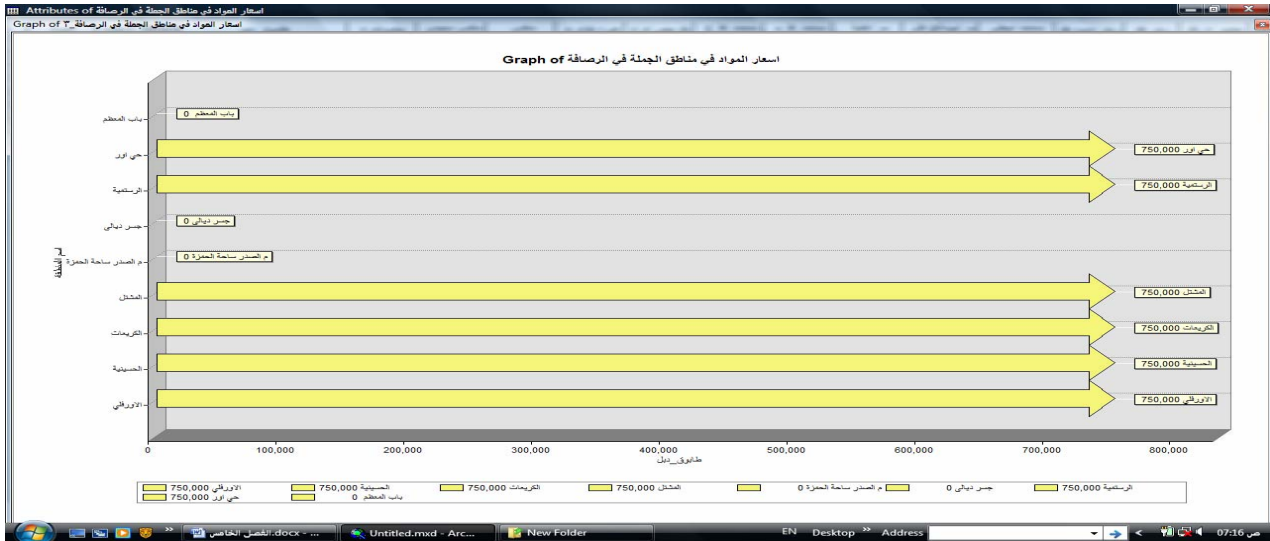
-:

(GPS)

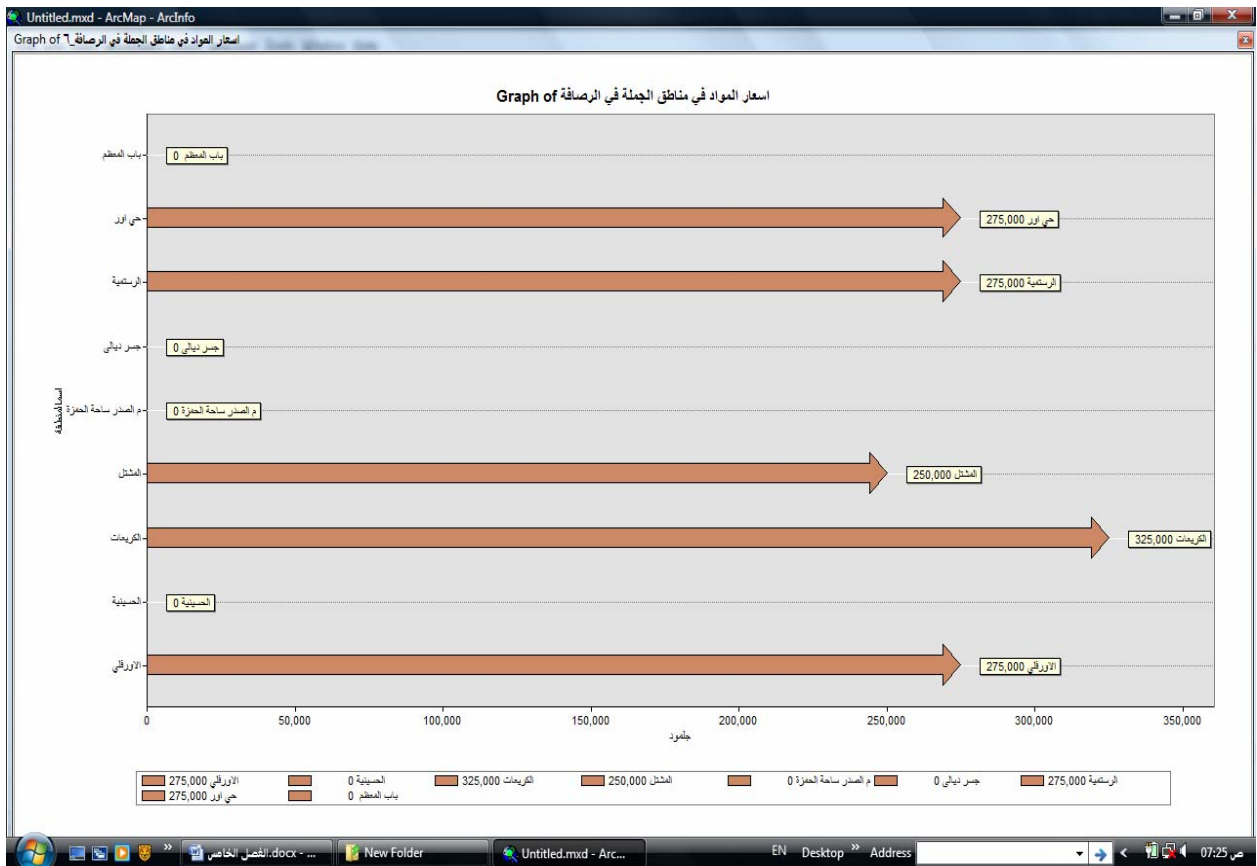
()

-:

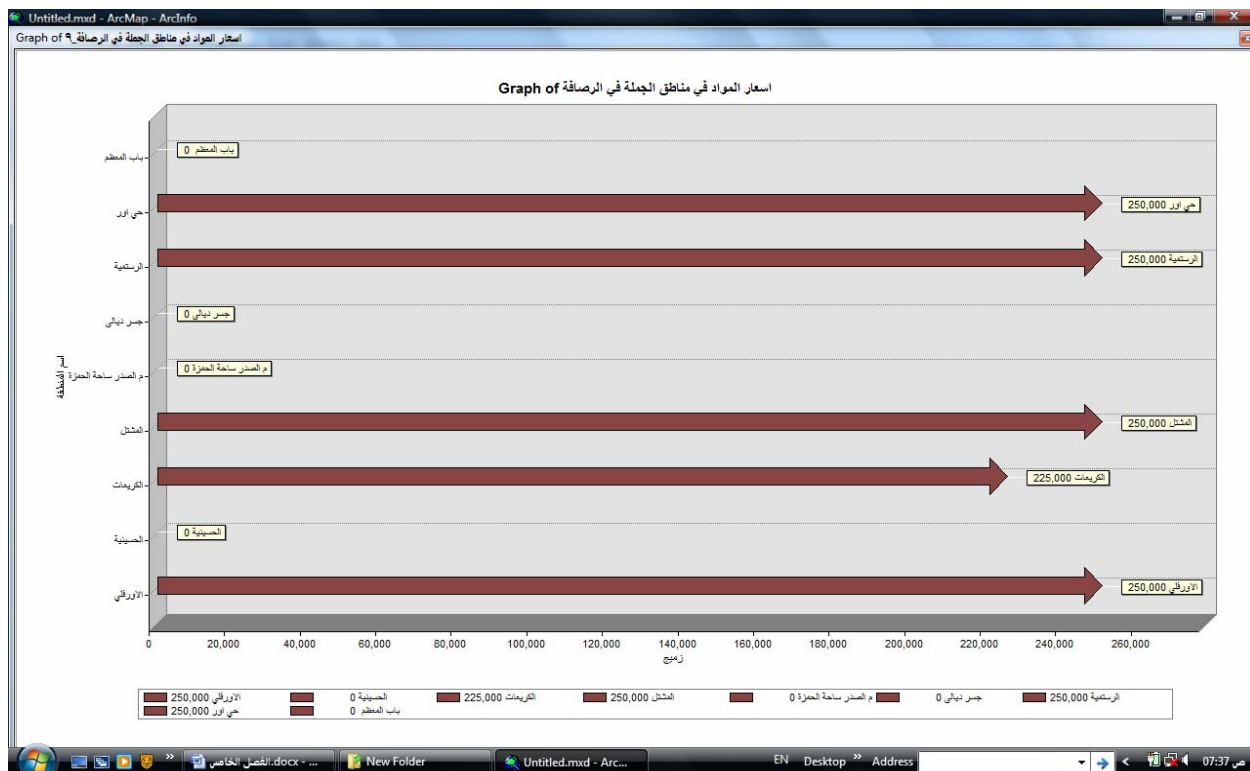
()



(.) (10)

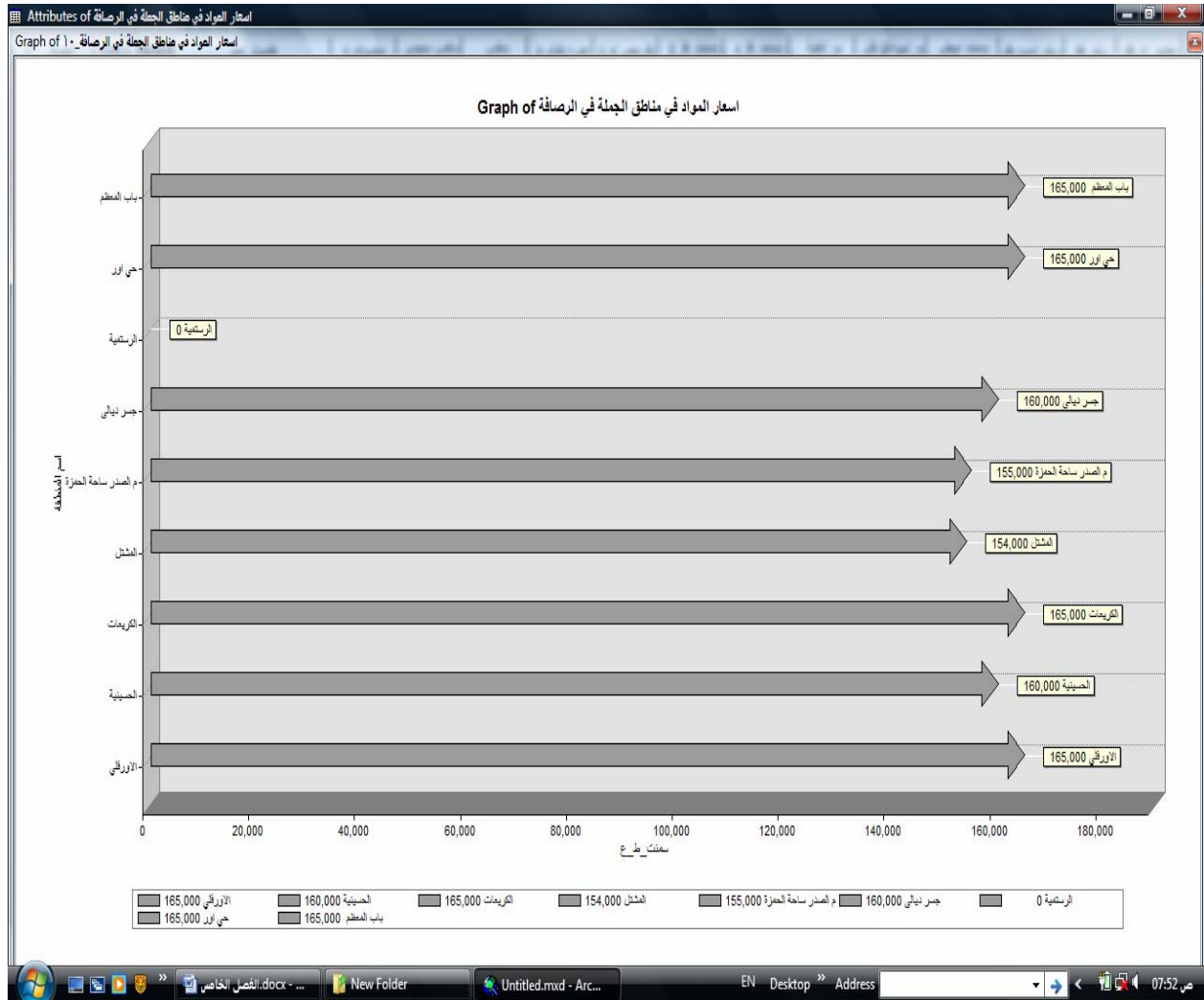


(.) (11)



(.)

(12)



(.)

(13)



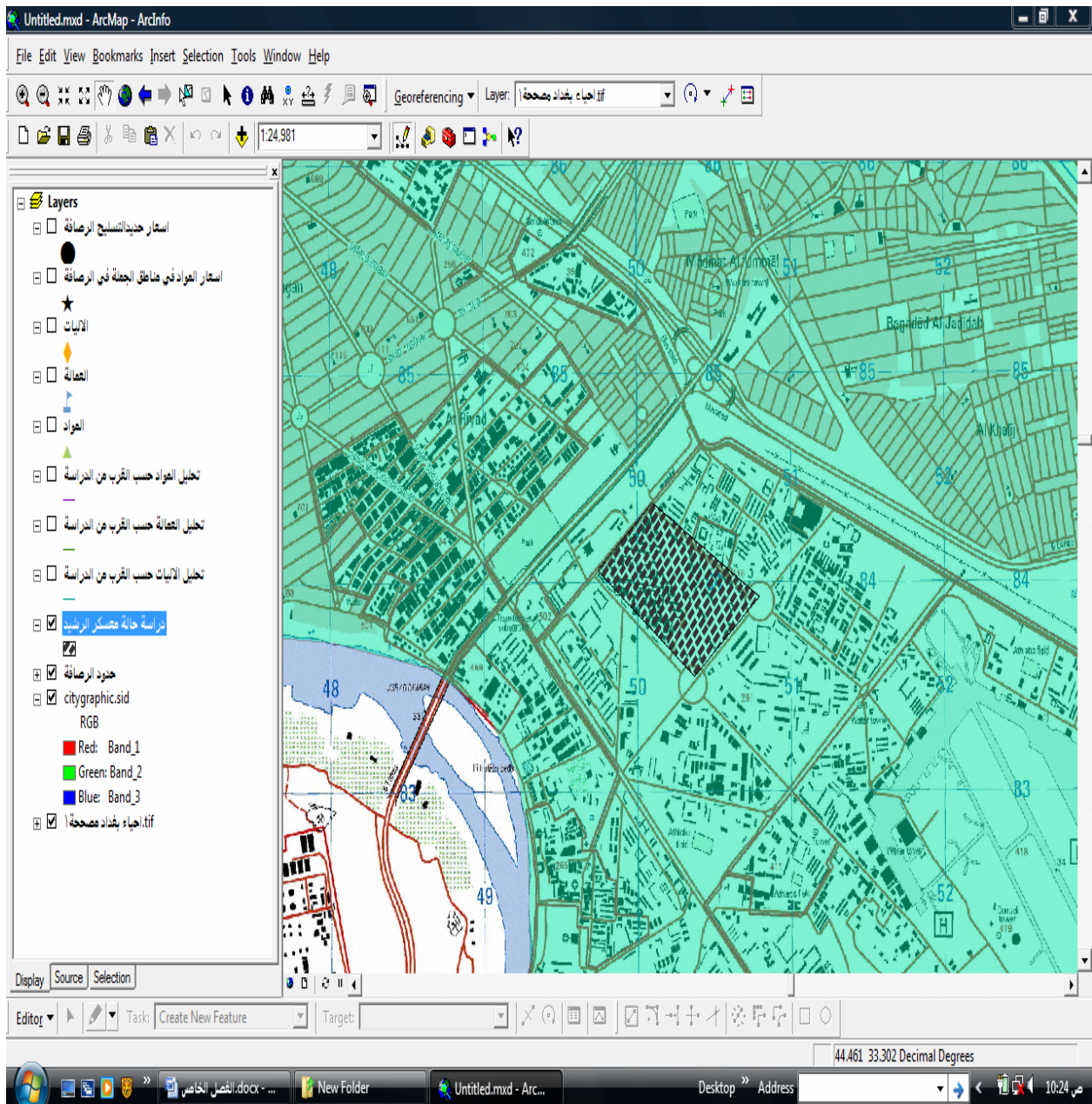
(1)

ت	اسم المادة	وحدة القياس	المنطقة التي تحتوي اقل سعر	السعر (دينار عراقي)
1	حديد تسليح 10 (ملم)	طن	شارع فلسطين (العقاري)	860000
2	حديد تسليح 12 (ملم)	طن	الكمالية	820000
3	حديد تسليح 16 (ملم)	طن	شارع فلسطين (العقاري)	850000
4	حديد تسليح قياسات أخرى	طن	الكريعات، العقاري، الكمالية	850000
5	بلوك	عدد	المشتل، الكمالية	700
6	سمنت باكستاني (مقاوم)	طن	مدينة الصدر (ساحة الحمزة)، حي اور	160000
7	طابوق جمهوري	دبل	من اي مكان مذكور يوجد فيه طابوق	750000
8	سمنت جسر (عادي)	طن	المشتل	160000
9	سمنت سعودي (عادي)	طن	اورفلي، مشتل، حي اور	200000
10	سمنت ايراني مقاوم	طن	المشتل	135000
11	سمنت ايراني (عادي)	طن	المشتل، حي اور	135000
12	رمل عادي	سكس	الحسينية	350000
13	رمل عادي	تك	الحسينية	150000
14	حصو مكسر	سكس	الاورفلي، المشتل	325000
15	حصو مكسر	تك	من اي مكان مذكور يوجد فيه حصو	200000
16	رمل اسود	تك	الحسينية	250000
ت	اسم المادة	وحدة القياس	المنطقة التي تحتوي اقل سعر	سعر (دينار عراقي)
17	الجلمود	تك	المشتل	250000
17	جص فني ابو المالح	طن	المشتل	205000
18	سمنت ابيض	تك	باب المعظم، ساحة الحمزة	200000
19	جص فني أهلية	طن	المشتل	145000
20	سمنت طاسلوجة (مقاوم)	طن	المشتل، مدينة الصدر (ساحة الحمزة)	172000
21	سمنت طاسلوجة (عادي)	طن	المشتل	154000
22	جص	تك	باب المعظم	340000
23	غبرة	تك	مدينة الصدر (ساحة الحمزة)	50000
24	زميچ	سكس	الكريعات	225000
25	سبيس	سكس	كريعات، رستمية، اورفلي	250000

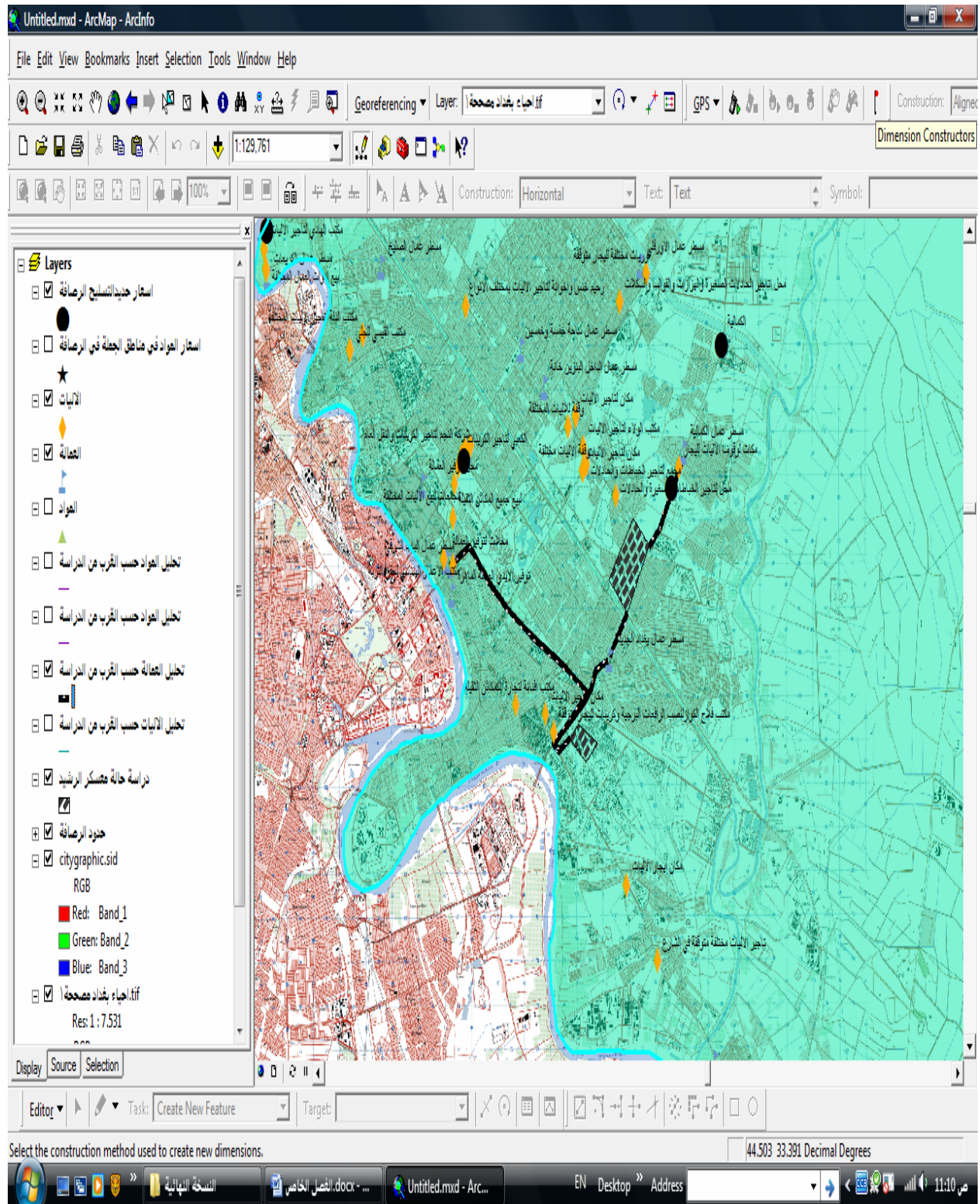
() :-

()

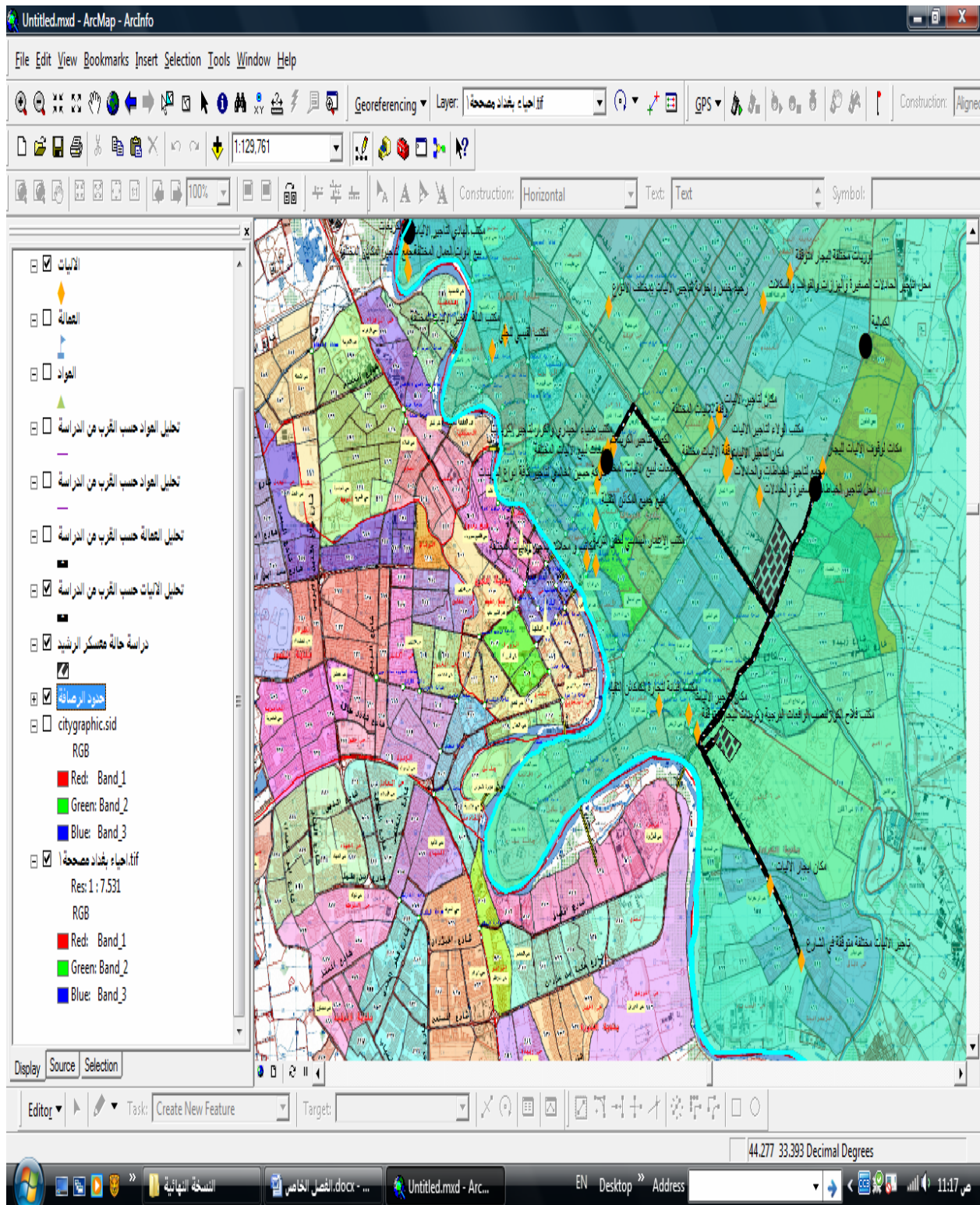
()



() () (15)



(16)



(17)



() -:

()

-:

13.265

-1

3.616

9.14

.(9-5)

-2

4.974

6.11

8.832

دراسة حالة مصنع الرغيد Attributes of									
FID	Shape	Id	اسم المنطقة	NEAR_FID	NEAR_X	NEAR_Y	NEAR_ANGLE		
0	Polygon	0	مشروع قنطرة الرغيد (مصنع الرغيد)	12	44.476856	33.310843	61.774666		
1	Polygon	0		12	44.476856	33.310843	125.768133-		

الاستنتاجات:-

- 1- اختصار الكم الهائل من البيانات إلى رقميات يسهل التعامل معها مع إمكانية استنتاج مجموعة من التقارير الهامة بشكل مبسط.
- 2- إمكانية على إدارة كم هائل من المعلومات الوصفية والمكانية ذات مصادر متعددة ومواقع مختلفة ضمن بيئة واحدة مما يسهل العمل عليها وإدارتها بشكل سهل ومبسط.
- 3- عرض المعلومات التي تم الحصول عليها بشكل سهل ومبسط وسرعة عالية ووقت قليل وإمكانية الحصول على معلومه عن مورد معين ومكان تواجده ونوعه وهل هو مكان جملة او مفرد بدقه وسرعة عاليه.
- 4- يمكن الاستنتاج بان نظم المعلومات الجغرافية أداة تحليلية وإحصائية جيدة يمكن استخدامها في تحليل الأسعار وقياس الطرق والتحليلات الإحصائية المختلفة بشكل سريع ومبسط مقارنة مع البرمجيات الأخرى.
- 5- جعل البيانات التي تم الحصول عليها على شكل طبقات في برنامج نظم المعلومات الجغرافية تتيح حرية التحكم في إظهار الطبقة المطلوبة أو جميع الطبقات في إن واحد ومن ثم السيطرة على المعلومة وإظهارها عند الحاجة إليها من قبل الإداريين أو أصحاب القرار بسهولة وسرعة.
- 6- يعد البحث أول قاعدة بيانات تم إنشاؤها (بحسب علمي) خاصة بتوزيع الموارد في جانب الرصافة لذلك يمكن الاستفادة منها في جميع دوائر المختصة وشركات المقاولات وشركات الاستثمارية لمعرفة أماكن تواجد الموارد وانسب الأسعار وأحسن الأماكن بنسبة لأي مشروع.
- 7- استخدام برمجيات نظم المعلومات الجغرافية يحسن في إدارة وتخطيط الموارد للمشاريع المختلفة ويقلل من عمر المشروع ويساعد على السرعة في التنفيذ. وذلك من خلال تحديد تفاصيل الموارد المطلوبة لتنفيذ العمل والتي يمكن توفيرها والبدائل لهذه الموارد في حالة عدم توفرها وحسب مراحل المشروع والبيانات التي أدخلت لبرنامج نظم المعلومات الجغرافية عن الموارد المختلفة يمكن الاستفادة منها بشكل كبير في هذه الجانب لانه يمتلك بيئة سهلة للتعامل مع أماكن تواجد الموارد وبدائلها.

- 8- يمكن اعتبار كلفة الموارد (المواد، الآليات، العمالة) أو الكلفة المباشرة هي من أهم الكلف لأي مشروع أو هي تمثل نسبة عالية من كلفة المشروع الكلية واثبت الباحث باستخدام برمجيات نظم المعلومات الجغرافية انه يمكننا اختيار الكلفة الأمثل للموارد وبالتالي اختيار الكلفة الأمثل للمشروع.
- 10- سهولة التعامل مع برمجيات نظم المعلومات الجغرافية وسهولة تغيير أي معلومة بسهولة وبساطة.
- 11- بتحديد أماكن تواجد الموارد على خارطة بغداد جانب الرصافة بواسطة برمجيات نظم المعلومات الجغرافية يسهل على المستثمرين الأجانب معرفة كل المعلومات عن تخطيط الموارد قبل تقديم عطاءهم لأي مشروع (مرحلة دراسة الجدوى).

التوصيات :-

- 1- الاستفادة من برمجيات نظم المعلومات الجغرافية في عملية التخطيط للموارد وتخمين الكلفة للمشاريع المختلفة.
- 2- تنمية الكوادر للعمل على برمجيات نظم المعلومات الجغرافية للاستفادة منها في إدارة المشروعات الهندسية ومجالات الهندسية الأخرى وتوجيه الشركات والمؤسسات لاستخدام برمجيات نظم المعلومات الجغرافية.
- 3- عمل جمع البيانات يجب ان تكون عالية الدقة وذلك للحصول على نتائج تحسّل مقبولة لكونه العنصر الأكثر تأثيراً على الجودة النهائية للعمل وكذلك وجوب استخدام خرائط ذات دقة عالية.
- 4- قاعدة البيانات الخاصة بتحديد الموارد في محافظة بغداد جانب الرصافة تحتاج الى عملية تحديث مستمرة لكل فترة لأن الأسعار والأمكنة تعتمد على العرض والطلب.

المصادر باللغة الانكليزية :

8. Layout.” Journal Construction Engineering and Management, Vol. 122, no.4, , Dec.1996.

9 .M.Y. Cheng, and J.C. Chen, “Integrating barcode and GIS for Monitoring construction progress.” Automation in Construction, Vol. 11, , Jan. 2002.

10. V.K. Bansal, and M. Pal, “Potential of geographic information systems in building cost estimation and visualization.” Automation in Construction, Vol. 16, no.3, , May 2007.

11. What is GIS?” GISLinx, USA, 2002, WWW.gislinx.com/what is GIS.html.

12. www.amesremote.com/section4.htm.

13. WWW.gislinx.com/what is GIS.html

المصادر باللغة العربية: -

1- الخزامي – محمد عزيز "نظم المعلومات الجغرافية" مجلة "PC-Magazine" ، النسخة العربية ، العدد 1 مايس ، 1995.

2- مرجان، رمضان، "الإسناد التخطيطي لمتخذي القرار باستخدام نظم المعلومات الجغرافية" ، جامعة بغداد، رسالة دكتوراه ، مقدمة الى المعهد العالي للتخطيط الحضري والإقليمي، 2005.

1. .Bolstad, Paul,”GIS Fundamentals”, Minnesota University, 2003, WWW.bolstad.gis.umn.edu/GISbook.html.

2. [British standard, BS 6079-2:2000 ,Project management.](http://www.britishestandard.com/BS_6079-2:2000_Project_management)

3. C.V. Camp, and M.C. Brown, “GIS procedure for developing three dimensional subsurface profile.” Journal of Computing in Civil Engineering, Vol. 7,no3 , July 1993.

4. Duekar, K.J, 1987,” GIS & computer Aid Mapping”, American Planning Association Journal”.

5. K. Varghese, and J.T. O’Connor, “Routing large vehicles on industrial construction site.” Journal Construction Engineering and Management, Vol. 121, no.1, , March 1995.

6. M.Y. Cheng, and C.Y. Yang, “GIS-Based cost estimate integrated with material layout planning.” Journal Construction Engineering and Management, Vol. 127, no. 4, , Jul./Aug. 2001.

7. M.Y. Cheng, and J.T. O’Connor, “ArcSite: Enhanced GIS for construction site

Effect of Steel Fibers on the Properties of Refractory Free Cement Concrete

Dr. Abeer Abdulqader Salih

University of Baghdad / College of Engineering

Department of Civil Engineering

drabeersalih@yahoo.com

Haneen Adel mohammed

University of Baghdad / College of Engineering

Department of Civil Engineering

Abstract

Free cement refractory concrete is a type of refractory concrete with replacing alumina cement by bonding materials such as white kaolin, red kaolin and fumed silica. The free cement refractory concrete used in many applications like Petrochemicals, iron furnaces and cement production industries.

The research clarifies the effect of steel fibers with two types crimped steel fibers and hooked steel fibers with percentages 0.5%, 1% and 1.5% by volume from weight of bauxite aggregates.

The additions of steel fibers with two types gave good properties in high temperatures where the specimens keep the dimension without failure and the properties made the best. the percentage of increasing for thermal conductivity was 44% for 1.5% crimped fibers and 42.8% for 1.5% hooked end fibers and the percentage increasing in bulk density of free cement refractory concrete was 30% for 1.5% crimped fibers and 27% for 15% hooked end fibers .

From this study can be concluded that the best types of steel fibers which used in free cement refractory concrete is the crimped type with percentage 1.5%.

Key words: Refractory concrete, steel fibers, free cement, fumed silica, white kaolin

الخرسانة الحرارية الخالية من السمنت هي احد انواع الخرسانة الحرارية والتي يتم انتاجها باستبدال السمنت الالوميني بأي مادة رابطة مثل الكاؤولين الابيض والكاؤولين الاحمر ومسحوق ابخرة السليكا. تستخدم الخرسانة الحرارية في العديد من التطبيقات الهندسية المختلفة مثل افران معامل السمنت و افران معامل انتاج الحديد والبتروكيماويات. البحث تتضمن دراسته تأثير الالياف الحديدية وبنوعيتها المجعده والمعقوفه النهايات وبنسب 0,5%، 1% و 1,5% من حجم الخليط بعد اختيار النسبه المثلى للمواد الرابطة على خواص الخرسانة الحرارية الخالية من السمنت. اوضحت نتائج الفحوصات ان الخرسانة الحرارية الخالية من السمنت بأن اضافته الالياف الحديدية وبنوعيتها المجعده والمعقوفه النهايات اعطت الخرسانة الحرارية الخالية من السمنت خواص جيده بسبب خواصها المطيلية وتقليل نسبة الفشل للنماذج حيث حافظت النماذج على تماسكها دون ان تشظي او تشقق. وصلت نسبته الزيادة في الموصلية الحرارية الى 44% عند اضافته 1,5% من الالياف المجعده و 42,8% عند اضافته 1,5% من الالياف المعقوفه النهايات كما وصلت نسبته الزيادة في الكثافة الكليه الى 30% عند اضافته 1,5% من الالياف المجعده و 27% عند اضافته 1,5% من الالياف المعقوفه النهايات.

من خلال هذه الدراسة نستنتج انه بالامكان انتاج خرسانة حرارية خالية من السمنت ذات خواص جيده عند اضافة الالياف الحديدية
المجعه بنسبه 1,5%.

1.0 Introduction

Refractories defines as "non-metallic materials having those chemical and physical properties that make them applicable for structures, or as components of systems, that are exposed to environments above 1000 °F (811 K; 538 °C).

Refractory materials are used in linings for furnaces, kilns, incinerators and reactors. They are also used to make crucibles

The refractory concrete suitable for use at high temperatures is composed of hydraulic cement (calcium aluminates cement) as the binding agent, combined with heat resistant refractory aggregates and or fillers. (Newman and Choo 2003)

Lee et al 2004 found that the refractories are composite materials used in large volumes in extreme, usually corrosive, environments as furnace linings for high temperature materials processing and other applications in which thermomechanical and thermochemical properties are critical. Many types of refractories range from relatively density (up to 90%) bricks to low density (10%) fibrous thermal insulation.

Hosseini et al 2008 studied the refractory concrete and presented it as a special type of concrete for high temperature usage, which consists of refractory aggregates, binders, plasticizer liquid and special admixtures if needed. Special binders are used in this type of concrete which are different in ordinary concrete structures. In normal or low temperatures, reaction between plasticizer liquid and binder harden the mixtures. In these concretes, like other types of concretes, water is necessary for forming and hardening process.

During heating process, the excess water will flow out of the concrete and by this reason, the amount of water should be carefully optimized in mixture design. Using admixtures and other chemical compounds can improve the curing process and reaching to some special properties.

Free cement refractory concrete (FCRC) is a type of refractory concrete made without cement using additives and different material bonds. It has a good volume stability and less vulnerable to the

main destructive forces in service slags, molten metals and chemical attack.

Peng et al 2007 studied the advantages of adding microsilica to bauxite based on low cement castables (LCC) and ultra low cement castables (ULCC) by reducing cement content and it affects the rheology and packing of refractory concrete.

The use of microsilica in refractory concrete provides better particle packing, it allows less water to be used while maintaining the same flow characteristics. It also promotes low temperature sintering and the formation of mullite in the matrix of the refractory concrete. This produces a refractory concrete that has a low permeability to avoid gas, slag and metal penetration.

Badiee and Sasan 2009 concluded that the addition of colloidal silica on refractory concrete decreases the bulk density of refractory concrete at all temperature because colloidal silica content leads to higher liquid content in the refractory concrete composition. Therefore the removal of moisture during drying causes increasing in porosity in the body. Also they found that the higher contents of colloidal silica have disadvantage in the strength development where the mechanical strength increases and the highest strength value at 1500 C° because of a higher degree of sintering and high ceramic bond.

1.2 Objective of this Research

The research aims for studying the effect of two types of steel fibers such as crimped steel fibers and hooked end steel fibers with different percentages on the properties of free cement refractory concrete.

1.3 Fiber Reinforced Refractory Concrete

Lankard and sheets 1971 showed that the history of adding steel fibers to ceramic materials begin in 1954, where this material showed an improvement in tensile strength and impact resistance and thermal stresses. This improvement was not effective at high temperatures due to fiber damage

during the smelting process of the ceramic fiber ferrous oxidation result.

ACI 544.1R-1996 Stainless steel fibers have been used as reinforcement in monolithic refractories since 1970. Steel fiber reinforced refractories (SFRR) have shown excellent performance in a number of refractory application areas including ferrous and nonferrous metal production and processing. Historically, steel fibers have been added to refractory concretes to provide improvements in resistance to cracking and spalling in applications where thermal cycling and thermal shock have limited the service life of the refractory. Also clarified that the fiber strength, stiffness, and the ability of the fibers are important for bond the refractory concrete.

Bond is dependent on the aspect ratio of the fiber. Typical aspect ratios range from about 20 to 100, while length dimensions range from 0.25 to 3 in. (6.4 to 76 mm). Steel fibers have a relatively high strength and modulus of elasticity, they are protected from corrosion by the alkaline environment of the cementitious matrix, and their bond to the matrix can be enhanced by mechanical anchorage or surface roughness.

Samadi and Fard 1999 observed that the refractory concrete was a brittle materials but it has high temperature resistance, chemical stability and thermal, mechanical shock. This happens because of rigid bond in ceramic. A rigidity of ceramic is considered a problem affect the properties of refractory and to solve this problem need steel fibers to increase toughness. They concluded that increasing fiber amount lead to:

1. Flow ability and workability decrease.
2. Modulus of rupture (MOR) and cold crushed strength (CCS) increase.
3. Hot modulus of rupture (HMOR) does not increase.
4. Thermal shock resistance increases up to 3% wt and then decreases.
5. Bulk density and apparent porosity make no change.

Alrawi 2000 found that the addition f steel fiber on refractory concrete improved the properties of refractory concrete in temperature reaching to 1000°C and it increases the density of refractory concrete. The compressive strength and the hot properties, because the steel fibers work to

decrease the cracks and limit it and also increasing the force of bond between the matrix.

Samadi 2003 presented the factors affecting the fibers functions, they are:

1. Fiber length.
2. Fiber orientation.
3. Amount of fiber.

The figure below show the stress-strain curve for refractory concrete with and without steel fibers

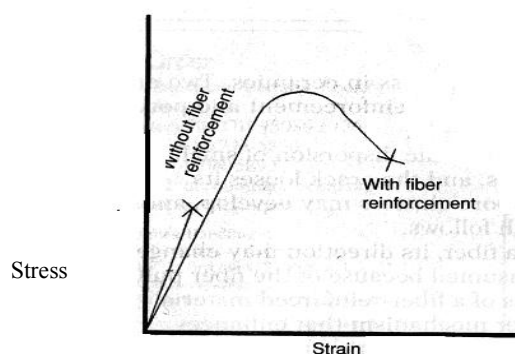


Fig 1 The stress-strain curve for reinforced refractory by **Samadi 2003**

Regin et al 2011 found that refractory concrete reinforced with steel fibers and adding microsilica observed increasing in density about 2% at 100 °C and it reaches to 7% at 800 °C. also referred that the reinforcement with steel fibers and microsilica leads to increase cold crushed strength from (22% to 47%) at 100 °C. This increase decreases in high temperature at 1000 °C where the increase becomes 9% with microsilica and steel fiber, they also observed that the optimum value of fiber 1% and microsilica 5% to increase strength

2. Raw Materials

2.1 Bauxite Aggregate

It is a fine aggregate produced by a State Company for the manufacture of refractories and it equipped from Building Research Center. It is available in the west area of Iraq.

Tables (1) and (2) show the sieve analysis and chemical analysis of bauxite aggregate. The sieve analysis indicates that the aggregate has a maximum size 4.75mm according

to the requirement of **ACI report 547-2008** and the chemical analysis shows the compound of

2.2 White kaolin

It is used as a bonding material in refractory concrete free cement (FCRC) with percentages 5, 10, 12 and 15 % by weight of bauxite aggregate and the chemical composition $Al_2Si_2O_5(OH)_4$ which transfer to metakaolin $Al_2Si_2O_7$ at $600\text{ }^{\circ}\text{C}$ and later formed mullite $3Al_2O_3.2SiO_2$ at $1050\text{ }^{\circ}\text{C}$.

It is available at Ardama region in west of Iraq and equipped from Building Research Center.

Table (3) shows the result of sieve analysis of white kaolin with maximum size 0.15 mm. It also shows thermal withstand of white kaolin at $1400\text{ }^{\circ}\text{C}$.

Table (4) shows the result of chemical analysis for white kaolin which mainly consist of silica SiO_2 with percent 48.10% and alumina Al_2O_3 with percent 35.55%. It also contains a little percentage of Fe_2O_3 , CaO and MgO which are considered as fluxes. This test made in the Laboratories of General Direction of Geological survey and Mining.

2.3 Fumed Silica

Fumed silica is produced by a vaporphase hydrolysis process by using chlorosilanes such as: silicon tetrachloride in a flame of hydrogen and oxygen. Fumed silica is described as a white and fluffy powder **ACI 234R-(1996)**. It is produced by Wacker Silicones Company in Germany and it is obtained from local markets with 10kg in one sack.

Fumed silica used as a bonding material with percentages 2, 3, 4 and 5% by weight of bauxite aggregate.

Chemical compositions are tested in the Laboratories of General Direction of Geological Survey and Mining is given in Table (5) and the physical information about this product is given in Table (6).

4. Steel Fiber

The steel fibers are used type of 309 with two forms: hook end and crimped fibers. These fibers are associated with others with adhesive material separate from other at mixing, it is used

according to **ACI 5441-R -1996**.

These fibers are known as Dramix with rectangular section $0.5*0.4\text{mm}$. The length of

crimped fiber is 30mm and 34mm for hooked end fiber. The Ultimate Tensile Strength 1050 MPa, Elastic Modulus 210 kN/mm^2 , Aspect ratio $l/d=80$ and Specific Gravity 8. It equipped from Building Center Research.

In this research three percentages are used for each type of fibers (0.5%, 1% and 1.5%) by volume.

3. Program of Experimental Laboratory

There is no standard method to design the mixes of free cement refractory concrete so depending on the previous research and some limitation like:

1. The modulus of rupture for refractory concrete after drying on $110\text{ }^{\circ}\text{C}$ not less than 2 MPa according to **ASTM C401-2000**.
2. The apparent porosity for drying samples is not greater than 45% according to **BS 1902: 3.8:1989**.

3.1 Preparation of Free Cement Refractory Concrete

In this research, the material has been mixed as a manual mix to obtain a homogenous mixture and good workability where the materials mixed in drying stage for 3 min, which begins with bauxite aggregate, adding white or red kaolin, fumed silica, steel fibers and later adding water with 4.5-5.5% by weight of aggregate. Table (7) shows the percentages of materials and water for each mixture.

For manual mixing, limited the percentage of water/dry weight according to **ASTM C860-2000** which is named as Ball- in- Hand which gave the standard consistency for refractory concrete. It is obtained for each percentage of white, red kaolin, fume silica and steel fibers. Where the percentage of water/dry weight is changed when adding fume silica and steel fibers where the fume silica need more water because of high surface area and when added steel fibers needs to increase water demand to increase workability of mixture. This process needs at least 5 min.

3.2 Molding and Compaction Models

The mixture placed in moulds after finishing from mixed where the dimensions of mould are $50*50*50\text{ mm}$ for cubic specimens and $40*40*160\text{ mm}$ for prism specimens. The moulds must be coated from the internal interface with a



thin layer of oil to prevent adhesion of mixture to aspects of mould.

The mixture compact in moulds with two layers by small steel hammer to obtain specimens with homogenous frame and with two shapes cubic and prisms. This process is done according to **ASTM C 862-2001**.

6.3.2 Drying and Firing

After compacting the specimens leave for 24 hours at laboratory temperature, after that open the molds and place the specimens in oven for drying at 110 C° for 24 hour according to **ASTM C865-1995**.

After drying the specimens are placed for firing until they reach the temperature 1200C° with burn rate 3.33 C°/min according to **ASTM C865-1995** then leave the specimens at this temperature for 2 hours known as soaking time where the specimens withstand high temperatures without sintering. The firing for FCRC effective on increasing the bonding force between the matrix. Fig 2 show the X-ray diffraction analysis for free cement refractory concrete with white kaolin and fume silica.

4. Experimental Tests

The tests are due to American Standard for Testing and Materials, where the Bulk Density is made according to ASTM C 20, the compressive strength due to ASTM C133 and thermal shock resistance according to BS1902: Section 7.6-1987 and reheat test according to ASTM C 113.

5. Result and Discussion

The steel fibers used with two types and different percentage 0.5%,1% and 1.5% by volume with white kaolin with different percentage 5%, 10%,12% and 15% by weigh of bauxite aggregate and 2% by weight bauxite aggregate of fumed silica and study the effect of fibers on properties of free cement refractory concrete.

5.1 Bulk Density

Table (8) and table (9), Figure (3,4) show the results of the density of free cement refractory concrete which increases with adding steel fibers because the high density of steel fibers reaches to 7.86 gm/cm³that increase the density .The presence

of white kaolin with fume silica forming mullite which improved the bonding force of matrix. The type of fiber also increases the bonding between matrix, the crimped steel fibers increase the density of free cement refractory concrete more than the hooked end fibers. The percentage of increasing was 30% for 0.5-1.5% crimped fibers and 27% for 0.5-1.5% hooked fibers.

5.2 Permanent Linear Change

From table (10) and table (11) figures (5), (6) show the result of permanent linear change of reinforced free cement refractory concrete. The additions of steel fibers on free cement refractory concrete lead to limited thermal shrinkage through retard. The attraction exists between particles of free cement refractory concrete in high temperature but the steel fibers with two types work to distribute the stresses which lead to keep the dimensions of samples. The permanent linear change decreases at adding the crimped steel fibers where reaches to 71.3% at increased from 0.5-1.5% and the percentage of decreasing for hooked end fibers reaches to 75.5% when increased from 0.5-1.5%.

5.3 Compressive Strength

Figures (7), (8) and table (12), (13) show that the compressive strength of free cement refractory concrete increased when the steel fibers adding. The steel fibers withstand the stresses that act on refractory concrete without breakage because the steel fibers failure in pullout which lead to increase the compressive strength. Different types of steel fibers affect on increasing compressive strength where the hooked end fiber have higher compressive strength than crimped fibers because of hooked end fibers make more strength bonds with matrix than crimped fibers result from the length of fibers that affect on Flexural Toughness Index which limit the force caused the first crack according to **ACI 5441-R 1996**. The percentage of increasing was 22.7% for 0.5-1.5% crimped fibers and 28.4% for 0.5-1.5% hooked end fibers.

5.4 Reheat Test

Figures (9) and (10) and table (14),(15) show that the reheat test of free cement refractory concrete decreased because the permanent linear change when steel fiber content increased where the fibers may decrease the cracks which may cause decreasing in shrinkage and expansion of specimens that also result from increasing the bonding force of matrix.

The decrease reaches to 84% for crimped steel fibers and 75% for hooked steel fibers.

5.5 Thermal Conductivity

The additions of steel fibers with the two types of fibers increase the thermal conductivity of free cement refractory concrete where steel fibers have a good thermal conductivity. It formed a continuous phase of steel fibers. This phase increased when the steel fiber content increased also the increasing in density for free cement refractory concrete improved the property of thermal conductivity. Thermal conductivity measured by lee disk device. Figure (11),(12) and table (16),(17) show the test result of thermal conductivity of free cement refractory concrete with two types of steel fibers.

The percentage of increase of thermal conductivity reaches to 44.7% for crimped fibers and 42.8% for hooked fibers.

5.6 Thermal Shock Resistance

Figures (13) and (14) and table (18),(19) below shows that the steel fibers work to decrease the cracks which are caused through the 20 cycles of cooling and heating for the specimens of free cement refractory concrete and distribute the stresses that lead to increase the resistance for spalling and bind the cracking parts which improve the thermal shock resistance.

The percentage of decreasing 50% when using 0.5-1.5% crimped fibers 46% for 0.5-1.5% hooked end fibers.

5.7 Modulus of Rupture

The modulus of rupture increased when the steel fibers content increased which work to increase density and bond strength between matrix. But this increasing was limited because of the oxidation of fibers at high temperatures where

the steel fibers loss the ductility at high temperatures.

The crimped steel fibers have percentage of increasing was 19.7% for 0.5-1.5% and the percentage of increasing for 0.5-1.5% hooked end steel fibers was 25.4% as shown in Figure (15) and (16) and table (20),(21).

6. Conclusions

Based on the field work and the testing technique adopted, the following conclusions can be drawn:

1. Bulk density of FCRC increased when using two types of steel fibers because of high density of steel fibers the percentage of increasing was 30% for 1.5% crimped fibers and 27% for 1.5% hooked end fibers.
2. Permanent linear change decreased when using two types of steel fibers for FCRC, the percentage of decreasing was 71.3% for 1.5% crimped fibers and 75.5% for 1.5% hooked end fibers.
3. Compressive strength of FCRC increased when using steel fibers with two types where the percentage of increasing was 22.7% for 1.5% crimped fibers and 28.4% for 1.5% hooked end fibers.
4. Permanent linear change decreasing after reheat test when using two types of steel fibers and the percentage of decreasing was 84% for 1.5% crimped fibers and 75% for 1.5% hooked end fibers.
5. Thermal conductivity of FCRC improved when using two types of steel fibers where the percentage of increasing was 44.7% for 1.5% crimped fibers and 42.8% for 1.5% hooked end fibers.
6. Thermal shock resistance improved with addition of two types of steel fibers where the specimens keep their dimension after 20 cycles of heating and cooling without failure.



Refrances

Alrawi .A 2000 "Improvement of Properties of Refractory Castables Using Steel Fibers" M.Sc., thesis, Department Of Civil Engineering, University of Baghdad 2000.

Alselmi .Z 2009 "Use of White Cement Instead of Alumina Cement to Produce Refractory Castables" M.Sc., thesis, Department Of Civil Engineering , University Of Baghdad 2009.

American Concrete Institute, ACI Committee 547- 2008 "Refractory Concrete ".

American Concrete Institute, ACI Committee 234-R-1996 "Guide for the use of silica fume in concrete" ACI manual of concrete practice, part (1), pp. (1-51).

American Concrete Institute, ACI 544.1R-1996 "Fiber Reinforced Concrete".

American Society for Testing and Materials C71-2008 "Standard Terminology Relating to Refractories" Vol. 15.1.

American Society for Testing and Materials C862 – 2001, "Standard Test Methods for Preparing Refractory Concrete Specimens by Casting" Vol. 15.1.

American Society for Testing and Materials C860 – 2000, "Standard Test Methods for Determining the Consistency of Refractory Castable Using the Ball – In – Hand Test" vol. 15.1.

American Society for Testing and Materials C133 –1997, "Standard Test Methods for Cold Crushing Strength and Modulus of Rupture of Refractories " Vol. 15.1

American Society of Testing and Materials C 865-1995 "Standard Practice for Firing Refractory Concrete Specimens" Vol. 15.1.

American Society of Testing and Materials C 20-2000 "Standard Test Method for Apparent Porosity, Water Absorption, Apparent Specific Gravity and Bulk Density " Vol. 15.1.

American Society for Testing Materials C401-2000 "Standard Classification of Castables Refractories " Annual book of ASTM standards vol. 15.01, pp. 98 Vol. 15.1.

British Standard Inst: BS 1902: Section 7.6: 1987, "Refractory Materials, Testing of Materials As Performed Test Pieces ".

British Standard Inst: BS 1902: section 3.8: 1989 "Refractory Materials, Determination of Bulk Density, True Porosity, and Apparent Porosity of Dense Shaped Products".

Hosseini .P, E. Eslami, M. Poorjafari, S. Vahidi, A. Madari 2008 "The Comparison Of Silicate Binder Refractory Concretes With Alumina Binder Concretes" First International and 14th National Studentship Conference on Civil Engineering August, Semnan University, I.R.IRAN.

Ismael M.R , R.D. des Anjas, R. Salomao and V.C. Pandolfelli 2006 " Colloidal Silica as a Nanostructured Binder for Refractory Concrete" Refractories Applications and News vol. 11 no. 4.

Kenneth Shaw, 1972" Refractories and Their Uses ", Applied Science Publishers Ltd, London.

Lankared. D.R and sheets. H.D 1971 "Use of Steel Wire Fibers in Refractory Concrete" published in American Ceramic Society Vol 50, No.5 1971.

Lee .W.E, S. Zhang, M. Karakus 2004 "Refractories: Controlled Microstructure Composites For Extreme Environments" Journal Of Materials Science 39, 6675 – 6685.

Lee. W. E., W. Vieira, S. Zhang, K. Ghanbari Ahari, H. Sarpoolaky, and C. Parr 2001" Castable Refractory Concretes " International Materials Reviews Vol. 46 No. 3.

Mohammed . H 2011 " effect of steel fibers on the properties of refractory concrete without alumina cement " M.Sc., thesis, department of civil engineering , university of Baghdad 2011

Newman John, Choo Ban Seng 2003 "Advance Concrete Technology", published in UK.

Regina Kalpokaite-Dickuviene, Kristina Brinkiene, Jūratė Česniene, Algis Makstys 2011" Effect of Fiber and Microsilica Incorporation on High Temperature Resistance of Cementitious Complex Binder" ISSN 1392–1320 Materials Science (MEDŽIAGOTYRA). Vol. 17, No. 1.

Samadi Hamed 2003 " Use of Steel Fibers in Refractories "American Ceramic Society Bulletin. Vol. 82 No.3 march

Samadi Hamed 1999 "The effect of particles size distribution on physical properties of castables " Sales Engineer PARS Refractories Co., Tehran, IRAN.
<http://individual.utoronto.ca/hamedsamadi/interceram03.pdf>

Samadi Hamed, Fard F. Golestani 1999 "the effects of fibers addition on low cement castables". Sales Engineering Dept., PARS Refractories Co. Tehran, Iran.

http://individual.utoronto.ca/hamedsamadi/THE_EFFECT_OF_FIBER_ADDITION_ON_LOW_CEMENT_CASTABLES.pdf

Tecommentaty 1999 "Elctrochnology use for drying of modern castable refractories" Electric power research institute Tec. commentary EPRI 1999.
http://www.energy.ca.gov/process/pubs/et_use_drying_tc114623.pdf

**LIST OF NOTATIONS**

ACI	American Concrete Institute
ASTM	American Society for Testing and Materials
B.S	British Standard
CAC	Calcium Alumina Cement
CCS	Cold Crush Strength
FCRC	Free Cement Refractory Concrete
HMOR	Hot Modulus of Rupture
LCC	Low Cement Castables
MOR	Modulus of Rupture
PLC	Permanent Linear Change
SFC	Self Flow Castables
SFRR	Steel Fiber Reinforced Refractories
ULCC	Ultra Low Cement Castables

Table .1 Sieve analyses for bauxite aggregate

Sieve size	%Passing	ACI report 547 requirements
4.75mm	100	
2.36mm	87.3	
1.18mm	64.2	
600 µm	46.6	
300 µm	24.5	Retaining on this sieve 75%
150 µm	12.8	Passing on this sieve 10-15%
Specific gravity	2.49	

Table .2 chemical analyses for bauxite aggregate

(The National Center Construction Laboratories)

Oxides	Percent
Al ₂ O ₃	66.1
SiO ₂	27.4
Na ₂ O+K ₂ O	0.61
CaO	2.46
MgO	0.95
Fe ₂ O ₃	1.21
L.O.I	0.14
Total	99.42

Table .3 Sieve analysis and thermal properties for white kaolin

Sieve size	%Passing
0.3 mm	100
0.15 mm	96
0.075 mm	55
Thermal bearing	>1400 C°

Table .4 Chemical analysis for white kaolin
(The National Center Construction Laboratories)

Oxides	Percent
Al ₂ O ₃	35.00
SiO ₂	48.10
Fe ₂ O ₃	0.85
CaO	1.42
MgO	0.45
SO ₃	0.68
L.O.I.	13.50
Total	100.00

Table .5 Chemical analysis of fumed silica

Oxides	Percent
SiO ₂	99.1
Fe ₂ O ₃	0.0035
Al ₂ O ₃	<0.035
TiO ₂	<0.006
MgO	0.0052
CaO	0.03
SO ₃	<0.7
L.O.I.	0.7

Table .7 The percentages of materials in mixture as %of weight of aggregate

Mix no.	White kaolin %	Fumed silica %	Steel fibers %	Water %	Bauxite aggregate %
1	5	2	0.5	4.5	88
			1	5	87
			1.5	5.5	86
2	10		0.5	4.5	83
			1	5	82
			1.5	5.5	81
3	12		0.5	4.5	81
			1	5	80
			1.5	5.5	79
4	15		0.5	4.5	78
			1	5	77
			1.5	5.5	76

Table.6 Physical properties of fumed silica
(weaker company 47 *)

Physical properties	Test result
Density gm/cm ³	2.2
SiO ₂ (when firing at 1000 C° for 2hours)	>99.8
Loss of weight (when firing at 1000 C° for 2 hours)	< 2%
Surface area m ² /gm	(170-230)
PH	3.9-4.3
Loss at drying for two hours at 105 C°	< 1.5%
Moisture %	0.82
% retained on 40 µm sieve	< 0.04

*Technical data

Table .8 Test result of bulk density of reinforced free cement refractory concrete with crimped

White kaolin %	Bulk Density gm/cm ³		
	Fumed silica 2%		
	0.5% crimped fiber	1% crimped fiber	1.5% crimped fiber
5	1.83	1.86	1.9
10	1.92	1.95	1.99
12	2	2.1	2.15
15	2.14	2.22	2.38

fibers

Table .9 Test result of bulk density of reinforced free cement refractory concrete with hooked fibers

White kaolin %	Bulk Density gm/cm ³		
	Fumed silica 2%		
	0.5% hooked fiber	1% hooked fiber	1.5% hooked fiber
5	1.81	1.85	1.88
10	1.9	1.92	1.96
12	1.98	2.06	2.12
15	2.08	2.16	2.3



White kaolin %	Permanent Linear Change %		
	Fumed silica 2%		
	0.5% crimped fiber	1% crimped fiber	1.5% crimped fiber
5	0.08	0.06	0.034
10	0.045	0.024	0.021
12	0.033	0.016	0.013
15	0.015	0.0043	0.002

Table .10 Test result of permanent linear change of reinforced free cement refractory concrete with crimped fibers

Table .11 Test result of permanent linear change of reinforced free cement refractory concrete with hooked fibers

White kaolin %	Permanent Linear Change %		
	Fumed silica 2%		
	0.5% hooked fiber	1% hooked fiber	1.5% hooked fiber
5	0.11	0.12	0.146
10	0.032	0.066	0.08
12	0.022	0.046	0.066
15	0.013	0.022	0.053

Table .12 Test result of compressive strength of reinforced free cement refractory concrete with crimped fibers

White kaolin %	Compressive Strength MPa		
	Fumed silica 2%		
	0.5% crimped fiber	1% crimped fiber	1.5% crimped fiber
5	5	5.12	5.25
10	5.4	5.6	5.76
12	5.81	5.9	6.24
15	6.2	6.35	6.56

Table.13 Test result of compressive strength of reinforced free cement refractory concrete with hooked fibers

White kaolin %	Compressive Strength MPa		
	Fumed silica 2%		
	0.5% hooked fiber	1% hooked fiber	1.5% hooked fiber
5	5.1	5.2	5.32
10	5.39	5.53	5.68
12	5.65	5.8	6.2
15	6.23	6.44	6.65

Table .14 Test result of Permanent Linear Change after reheat of reinforced free cement refractory concrete with crimped fibers

White kaolin %	Permanent Linear Change %		
	Fumed silica 2%		
	0.5% crimped fiber	1% crimped fiber	1.5% crimped fiber
5	0.35	0.24	0.15
10	0.18	0.1	0.08
12	0.083	0.077	0.046
15	0.038	0.04	0.024

Table .15 Test result of permanent linear change after reheat of reinforced free cement refractory concrete with hooked fibers with hooked fibers

White kaolin %	Permanent Linear Change %		
	Fumed silica 2%		
	0.5% hooked fiber	1% hooked fiber	1.5% hooked fiber
5	0.18	0.15	0.13
10	0.14	0.11	0.083
12	0.12	0.1	0.075
15	0.08	0.053	0.02

Table .16 Test result of thermal conductivity of reinforce free cement refractory concrete with crimped fibers

White kaolin %	Thermal Conductivity wt/k.m		
	Fumed silica 2%		
	0.5% crimped fiber	1% crimped fiber	1.5% crimped fiber
5	0.35	0.42	0.5
10	0.4	0.45	0.58
12	0.45	0.52	0.61
15	0.47	0.57	0.67

Table .19 Test result of % decreasing compressive strength after 20 cycles of cooling and heating of reinforced free cement refractory concrete with crimped fibers

White kaolin %	% of decreasing in Compressive Strength		
	Fumed silica 2%		
	0.5% hooked fiber	1% hooked fiber	1.5% hooked fiber
5	58.8	55	54.3
10	56.5	54.2	52.8
12	55.6	52.6	51.9
15	51.3	50.2	48.1

Table .17 Test result of thermal conductivity of reinforce free cement refractory concrete with hooked fibers

White kaolin %	Thermal Conductivity wt/k.m		
	Fumed silica 2%		
	0.5% hooked fiber	1% hooked fiber	1.5% hooked fiber
5	0.3	0.38	0.45
10	0.35	0.43	0.5
12	0.4	0.47	0.58
15	0.46	0.55	0.63

Table .20 Test result of modulus of rupture for reinforced free cement refractory concrete with crimped fibers

White kaolin %	Modulus of Rupture MPa		
	Fumed silica 2%		
	0.5% crimped fiber	1% crimped fiber	1.5% crimped fiber
5	4.25	4.38	4.61
10	4.7	4.79	4.97
12	4.88	5.06	5.19
15	5.01	5.18	5.33

Table .18 Test result of compressive strength after 20 cycles of cooling and heating of reinforced free cement refractory concrete with crimped fibers

White kaolin %	% of decreasing in Compressive Strength		
	Fumed silica 2%		
	0.5% crimped fiber	1% crimped fiber	1.5% crimped fiber
5	59	56	55
10	53.5	53	52.3
12	52.6	52.2	51.1
15	51.3	50.7	48.3

Table .21 Test result of modulus of rupture for reinforced free cement refractory concrete with hooked fibers

White kaolin %	Modulus of Rupture MPa		
	Fumed silica 2%		
	0.5% hooked fiber	1% hooked fiber	1.5% hooked fiber
5	4.56	4.73	4.94
10	4.83	5.02	5.08
12	5.16	5.24	5.37
15	5.2	5.38	5.46

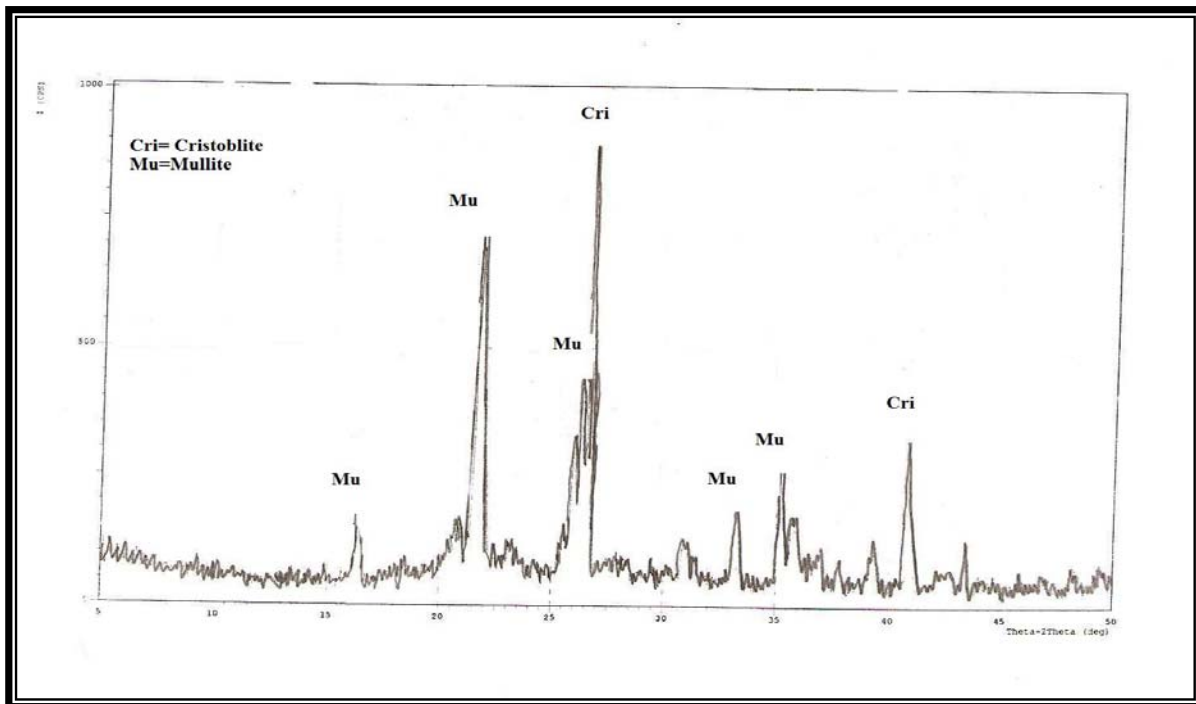


Fig. 2 X-ray diffraction analysis for free cement refractory concrete with white kaolin and fume silica

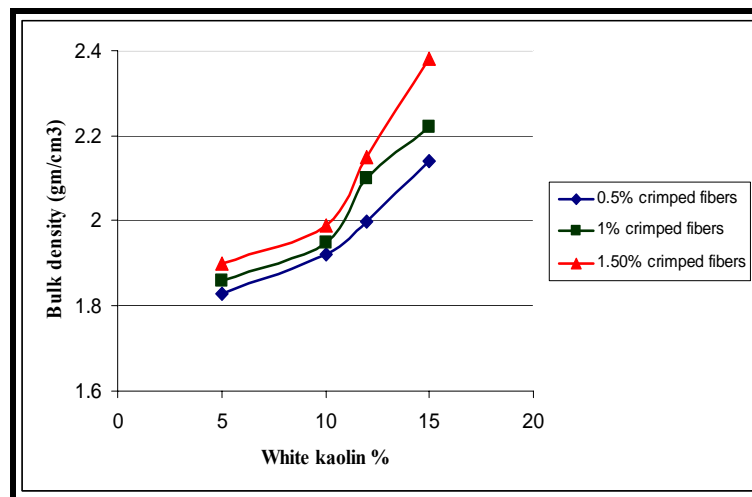


Fig.3 The relation between bulk density of reinforced free cement refractory concrete with crimped fibers and white kaolin

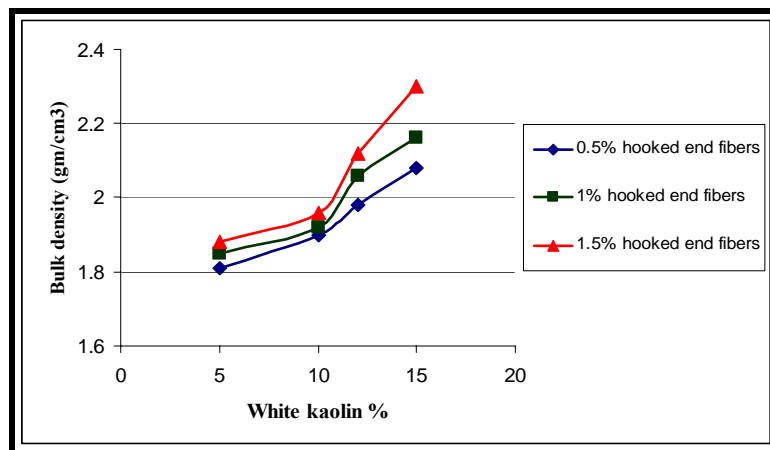


Fig. 4 The relation between bulk density of reinforced free cement refractory concrete with hooked end and white kaolin

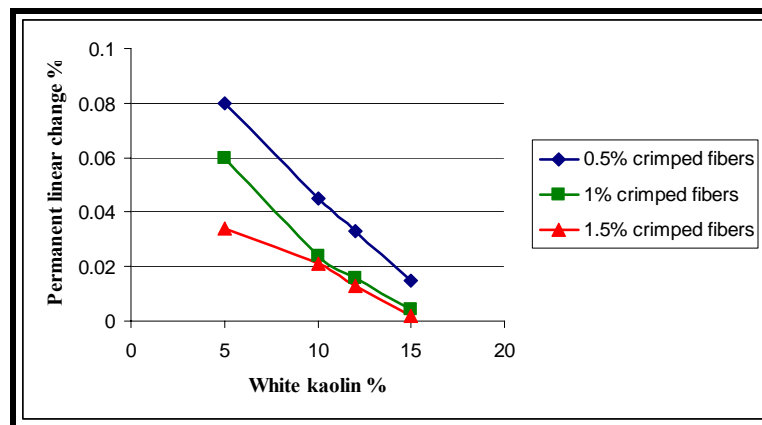


Fig. 5 The relation between permanent linear change of reinforced free cement refractory concrete with crimped fibers and white kaolin

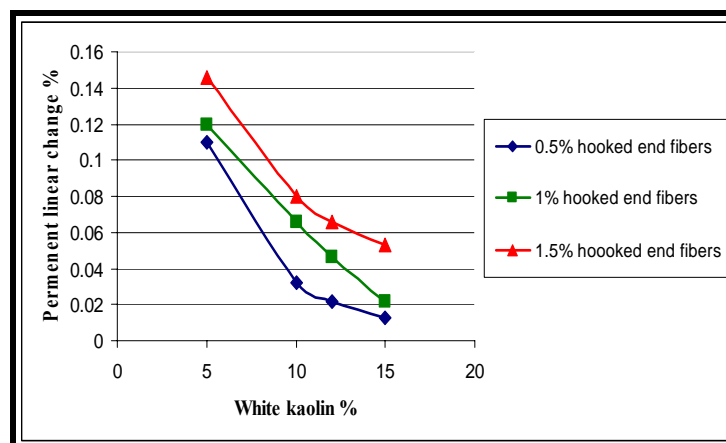


Fig. 6 The relation between permanent linear change of reinforced free cement refractory concrete with hooked fibers and white kaolin

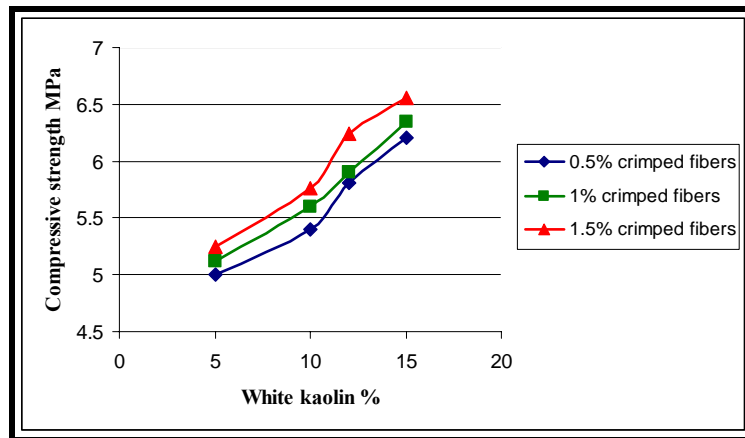


Fig .7 The relation between compressive strength of reinforced free cement refractory concrete with crimped fibers and white kaolin

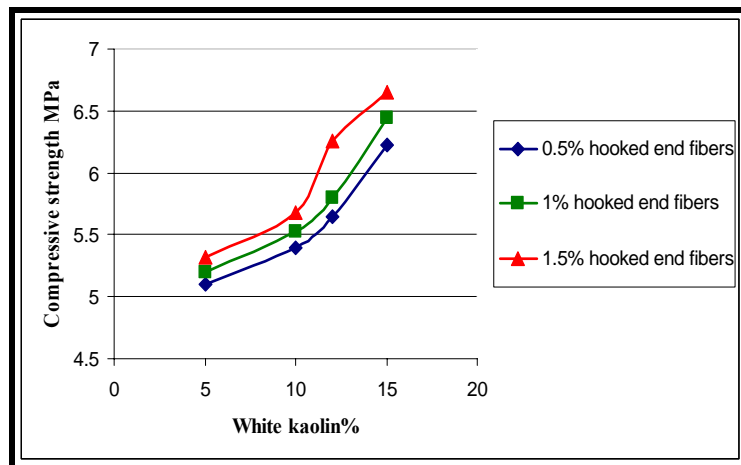


Fig .8 The relation between compressive strength of reinforced free cement refractory concrete with hooked fibers and white kaolin

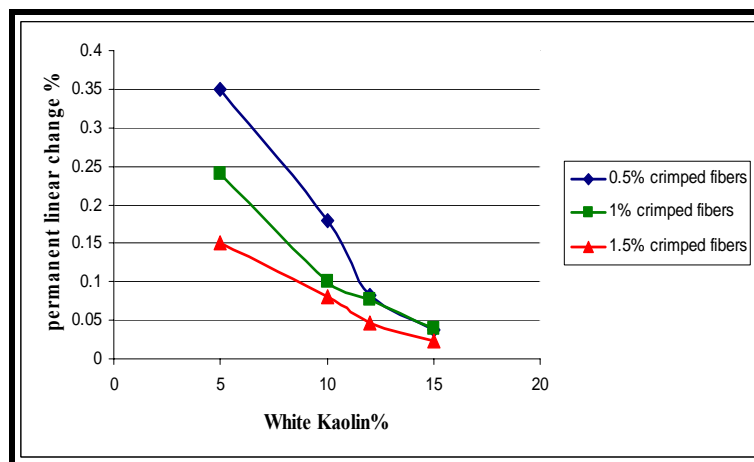


Fig .9 The relation between permanent linear change of reinforced free cement refractory concrete with crimped fibers and white kaolin after reheating

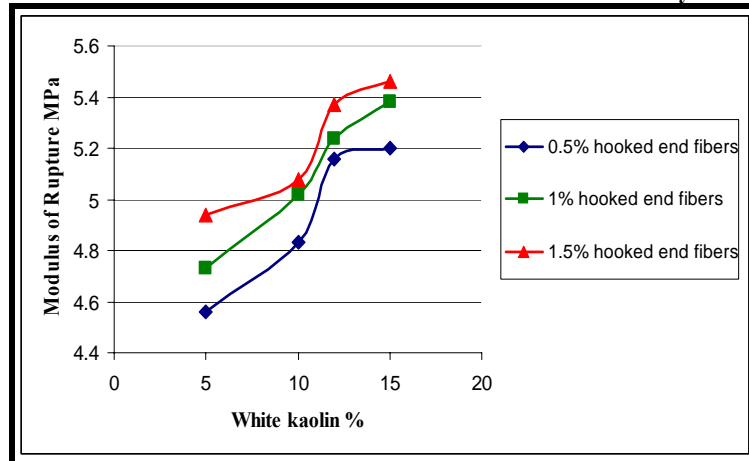


Fig .10 The relation between modulus of rupture of reinforced free cement refractory concrete with hooked fibers and white kaolin

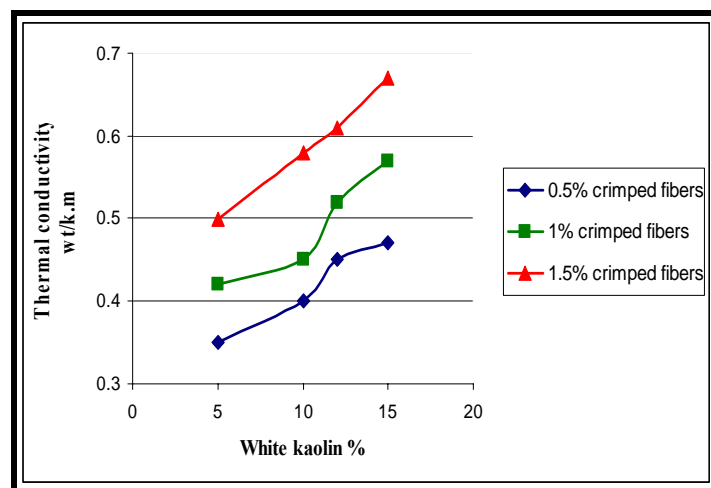


Fig .11 The relation between thermal conductivity of reinforced free cement refractory concrete with crimped fibers and white kaolin

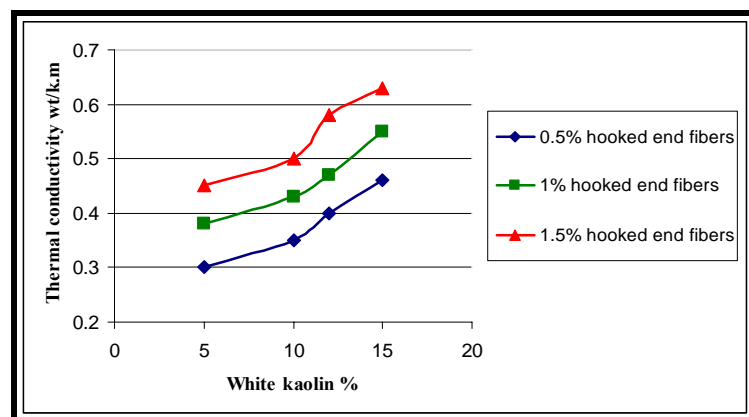


Fig .12 The relation between thermal conductivity of reinforced free cement refractory concrete with hooked fibers and white kaolin

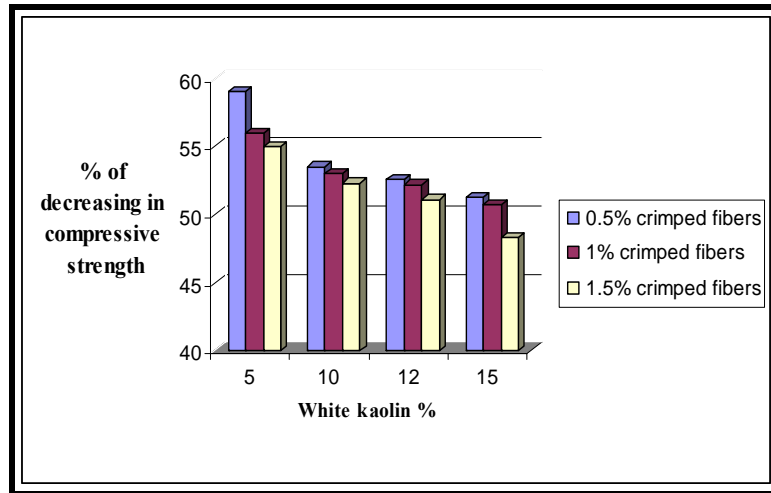


Fig .13 The relation between compressive strength of reinforced free cement refractory concrete with crimped fibers and white kaolin

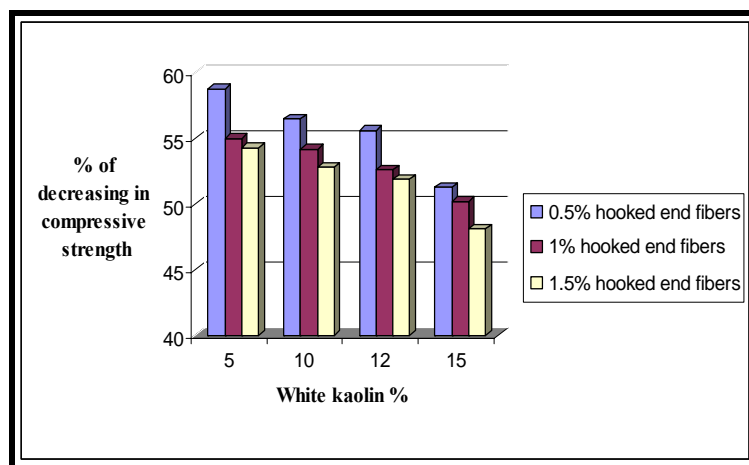


Fig.1 4 The relation between compressive strength of reinforced free cement refractory concrete with hooked fibers and white kaolin

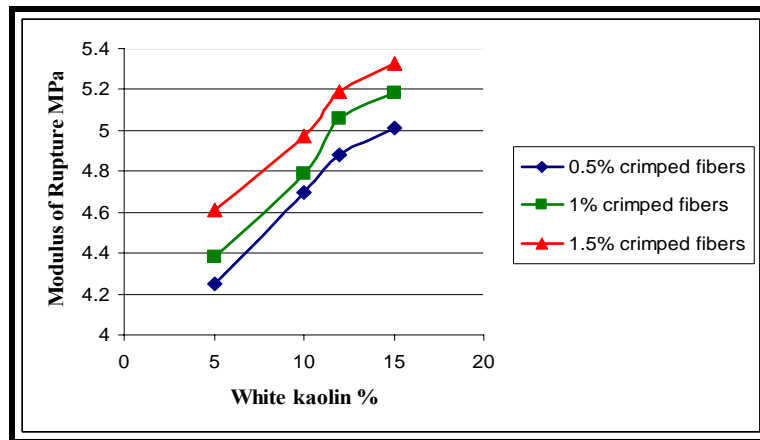


Fig .15 The relation between modulus of rupture of reinforced free cement refractory concrete with crimped fibers and white kaolin

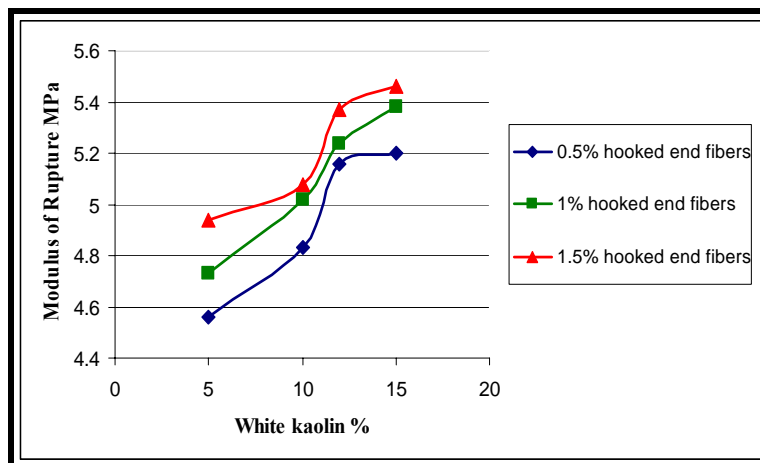


Fig .16 the relation between modulus of rupture of reinforced free cement refractory concrete with hooked fibers and white kaolin

Effect of Fire Flame (High Temperature) on the Self Compacted Concrete (SCC) One Way Slabs

Ammar A. Hammadi

University of Anbar

M. Sc. student

Ammaliyak@yhoo.com

Amer F. Izzat

University of Baghdad

Lecturer in Civil Engineering Dept.

AmerFarouk@yhoo.com

Jamal A. Farhan

University of Anbar

Lecturer in Civil Engineering Dept.

Jamal_alesawi@yhoo.com

Abstract:

Experimental work was carried out to investigate the effect of fire flame (high temperature) on specimens of one way slabs using Self Compacted Concrete (SCC).

By using furnace manufactured for this purpose, twenty one reinforced concrete slab specimens were exposed to direct fire flame. All of specimens have the same dimensions. The slab specimens were cooled in two types, gradually by left them in the air and suddenly by using water. After that the specimens were tested under two point loads, to study, the effect of different: temperature levels (300°C, 500°C and 700°C), and cooling rate (gradually and sudden cooling conditions) on the concrete compressive strength, modulus of rupture, flexural strength and the behavior of reinforced concrete slab specimens and comparing the results with specimens without burning (reference specimens). The results showed that, the concrete compressive strength, concrete modulus of rupture and the flexural strength decreases while the maximum (central) deflection increases with increasing the fire flame temperature. For suddenly cooled specimens the residual flexural strength is less than that of gradually cooled specimens while the deflection is greater. For slabs with 20 MPa concrete strength and gradually cooled, the residual bending strength percent is 81.5%, 75% and 62.3% ,while the increase in central deflection is 5%, 33%, and 105% at burning temperature 300°C, 500°C and 700°C respectively. For suddenly cooled specimens of the same strength and exposed to the same temperatures above the residual flexural strength is 77.9%, 68.3% and 58.3% while the increase in central deflection is 25%, 52%, and 118% respectively. When the strength of concrete specimens increase, the residual flexural strength experiences small increase and the increase is of lower rate in the central deflection for 300 °C and 500 °C burn temperatures while the decrease is significant for 700 °C burning temperature.

Key words: SCC, elevated temperature, fire flame

الخلاصة:

تم اجراء بحث عملي لبحث تأثير درجات الحرارة العالية (الحريق) على نماذج من البلاطات المسلحة باتجاه واحد والمصنعة من الخرسانة ذاتية الرص. باستخدام فرن تم تصنيعه لهذا الغرض، تم تعريض واحد وعشرون نموذج بلاطة خرسانية الى حرارة اللهب المباشر ، وجميع النماذج لها نفس الابعاد . ثم تبرد النماذج بطريقتين، تبريد بطيء بتركها في الهواء، وتبريد فجائي باستخدام الماء وتحميلها بنقطتي تحميل لدراسة تأثير مختلف: درجات الحرارة المختلفة (300°C, 500°C و 700°C) ، و معدل التبريد (تدريجي ، فجائي) على مقاومة الخرسانة، معامل الكسر، مقاومة الانحناء وتصرف البلاطات الخرسانية ومقارنة النتائج مع النماذج غير المحروقة (نماذج السيطرة). أظهرت النتائج أن مقاومة الخرسانة، معامل الكسر، ومقاومة الانحناء تقل بينما يزيد الانحراف الأقصى بزيادة درجة حرارة الحريق . كما أظهرت النتائج أنه لحالة التبريد الفجائي فان مقاومة الانحناء المتبقية تقل بينما يزيد الانحراف الأقصى مقارنة مع حالة التبريد التدريجي حيث تبين أن نسبة مقاومة الانحناء المتبقية للبلاطات ذات مقاومة (20MPa) والمبردة تدريجيا هي 81.5% ، 75% و 62.3% بينما كانت نسبة الزيادة في الانحراف الأقصى 5% ، 33% و 105% للنماذج المعرضة الى 300°C, 500°C و 700°C على التوالي . أما لحالة التبريد الفجائي ولنفس المقاومة ودرجات الحريق أعلاه فان مقاومة الانحناء المتبقية هي 77.9% ، 68.3% و 58.3% بينما كانت الزيادة في الانحراف الأقصى 25% ، 52% و 118% على التوالي. كما أظهرت النتائج أن الزيادة في مقاومة الانضغاط تؤدي الى زيادة في نسبة مقاومة الانحناء المتبقية بمقدار قليل بينما تزيد نسبة الانحراف الأقصى بمقدار ضئيل عند الحرق بدرجات حرارة (300 °C و 500 °C) وتقل بمقدار مهم عند الحرق بدرجة حرارة 700 °C .

Introduction:

High temperature due to fire have a significant effect on the strength and deformation characteristic of various structural components such as columns, beams, slabs, etc. But the slab member is the most affected member, because of its wide exposed surface area with respect to its thickness. Also, the fire may at one side of the slab; this causes a gradation in temperature across the slab depth.

At the beginning researchers were focusing on the chemical and physical changes within the concrete, such as the decomposition of calcium hydroxide (Ca(OH)_2), the incompatibility at the aggregate–cement paste boundary and the crystal transformation of quartz (SiO_2) [Lau A. and Anson M., 2006]. [Peter J. Moss et al., 2008] studied the fire behaviour of two-way reinforced concrete slabs. He found that the concrete and the reinforcing steel near the bottom of the slab heat up well before the top reinforcing steel and the top of the concrete, and once the bottom steel temperature exceeds 300°C , the yield strength of the steel decreases with increasing temperature, so that the negative (sagging) bending strength of the concrete section diminishes, as does its membrane strength. [Mehrafarid Ghoreishi et al., 2010] studied the response of flat plate concrete slab systems to fire exposure, they concluded that the combined fire and imposed loading can severely change structural behavior. [Jeremy Changi et al., 2006] studied the analyses of hollow-core concrete floor slabs exposed to fire to reduce the effect of temperature. Most of the researchers deal with heat without flame or gasses which accomplished to the fire, little researchers deal with the effect of exposing reinforced concrete slabs to direct fire flame and the time of concrete in direct contact with fire flames.

[Harada et al 1972] found that the residual bond strength between the

concrete and the reinforcement was 44% of the control specimen at a temperature 300°C , while the residual strength of compression strength was 60% at the similar temperature.

Material Properties:

Cement:-

Ordinary Portland Cement (OPC) produced at Al-Sharkiya factory from the Kingdom of Saudia Arabia was used in this work. It was stored in a semi-dry place (Laboratory conditions) to avoid exposure to atmospheric condition. The physical properties and chemical composition of cement are shown in **Tables 1 and 2** respectively. Test results indicate that the adopted cement conform to the [Iraqi specification No.5/1984].

Fine aggregate:-

The used sand was from Al-Khirbeet factory. It was of (4.75mm) maximum size. **Table 3** shows the chemical and physical properties for sand. The sieve analysis of sand used throughout this work lies within the range defined by [ASTM C33-03].

Coarse aggregate:-

Crushed aggregate with (10mm) maximum size from Al-Suleiman factory for land concrete blocks was used as coarse aggregate in all mixes. The grading obtained from the results of sieve analysis of the aggregate lies within the range defined by [ASTM C33-03]. **Table 4** shows the chemical and physical properties for gravel.

Superplasticizer (SP) :-

For the production of self-compacting concrete, super plasticizer (high water reducing agent HWRA) based on poly carboxylic ether is used. One of a new generation of polymer-based super plasticizer designed for the production of SCC (Glenium 51) is used. (Glenium 51) has been primarily developed for the applications in the ready mixed concrete

industries where the highest durability and performance are required. It is specific gravity is 1.1, at 20°C, PH=6.5 as issued by the producer. In this study, the dosage of (G51) was (3%) of cement weight mixes.

Silica fume:

Silica fume mineral admixture or micro silica: composed of ultrafine, amorphous glassy spheres of silicone dioxide (SiO₂), produced by Crosfield Chemicals, Warrington, England.

Concrete mix proportions:

There were three types of compressive strength of self-compacted concrete in this study, thus three mix types are required. The ratios of mixes were resulted by casting trial mix cubes and testing in (7 days) age. Every trial mix had three cubes of (100*100*100 mm). The details of mixes for SCC concrete samples are shown in **Table 5** below. Plain bars of 3mm diameter are used in each direction at the bottom of slab. The properties of the bars are shown in **Table 6**. The three types of concrete were mixed by horizontal drum laboratory mixer with a capacity of 0.05 m³. In all the mixes, the aggregates and cement were first mixed dry for about 1 minute. The water, silica fume and the superplasticizer together were mixed externally in a pan then added to the mixer, after that mixing continued for a further 1 minute.

Experimental program:

Twenty one reinforced concrete slabs were tested. All of specimens have the same dimensions, length is 500mm, width is 250mm and the thickness is 40mm. The reinforcement is the same for all specimens which is (6 – ϕ 3mm) in long direction and (8 – ϕ 3mm) in short direction. The dimensions and reinforcement details of the slabs are shown in **Figs. 1 and 2**. Specimens were tested in the structural laboratory of the College of Engineering at Baghdad University.

The specimens are divided into three groups A, B and C. Group A contains three specimens which are not exposed to temperature representing the reference specimens; each specimen has a different strength (20, 30 or 40 MPa). Each of the groups B and C have nine specimens; the difference between them is in the method of cooling after exposing to high temperature. Group B is gradually cooled while group C is suddenly cooled by water. Each of the group B or C is divided into three subgroups; each of them has a different strength (20, 30 or 40 MPa). The three specimens of each subgroup are exposed to a different temperature (300, 500 or 700 C). The detailed classification of groups is shown in **Table 7**. The control samples were two types. First type was cubes (100x100x100)mm to test the compressive concrete strength and second type was prisms (100x100x500)mm to test modulus of rupture of concrete.

The furnace was manufactured by using 3mm thick steel plate to burn one specimen in each time, as shown in **Fig. 3**. The specimens were cast, then moist cured for seven days, after that dried by air in the laboratory. Eighteen specimens were burned by exposing to fire flame at age 45 days at three temperatures levels 300, 500 and 700 C and for similar exposure period of 1 hour after reaching the target temperature.. After this period, the fire flame was turned off, the slab specimens were removed and the specimens was cooled either gradually by left in air or suddenly by using splash of water till reaching the normal temperature. The temperature was monitored by using digital thermometer inside the furnace and a thermocouple wire (Type K) made of Nickel-Chromium covered with cement to resist the temperature, with a digital temperature reader.

Results and discussions:

Compressive strength:

The test results of compressive strength as shown in **Table 8** of the cubes (100*100*100mm) after burning by fire flame furnace showed that, increasing the temperature resulted in reducing the compressive strength with approximately the same percentage in all strengths of concrete ($f'_c=20, 30$ and 40MPa) grade with respect to each group of cooling type until (500°C). Also, the cooling method had a clear effect on compressive strength of the cubes, where the cubes cooled suddenly by spraying them with water were less strength than the others which cooled gradually by leaving them in air (laboratory condition), as shown in **Figs. 4-A, 4-B & 4-C**. The average percentage of residual the compressive strength for all strength groups was (89%) for the cubes cooled gradually in air and (84.4%) for the cubes cooled suddenly by water. The results of gradual cooling agreed with [Anagnostopoulos N. et al., 2009] dealing with normal concrete. The values of the decreases in compressive strength depend on the nature of the aggregate and the initial moisture content of the concrete. The changes in strength have been attributed to a combination of decomposition of the hydrated pastes, deterioration of the aggregates and the thermal incompatibilities between paste and aggregate leading to stress concentrations and microcracking [Mindess S et al., 2003]. Concrete is a brittle composite material that consists of binder (cement) paste and aggregates (fine and coarse aggregates). These materials have different mechanical and physical properties, including different coefficients of thermal expansion. At a lower elevated temperature, the thermal expansion of the cement paste is slightly greater than that of the aggregate. Consequently, in the concrete matrix, the cement paste is

under hydrostatic compression, and the aggregates are under biaxial compression and tension. As the temperature further increases, the thermal strain of the cement paste changes to negative (shrinking) due to chemical changes, whereas the aggregate continues to expand. The corresponding stresses in concrete are that, the aggregates are under hydrostatic compression and the cement paste is under biaxial compression and tension. Also, the development of micro-cracks increases beyond (300°C) and firstly occurs around calcium hydroxide $\text{Ca}(\text{OH})_2$ crystals, and partial volatilization of calcium silicate hydrate gel commenced at about (500°C). The pore size and porosity of the hydrate matrix will increase, and the mechanical properties (compressive strength and modulus of rupture) of the hydrates will be weakened [Piasta J., 1984]. For the cubes of 20 MPa nominal compressive strength, the percent of residual strength after exposing to 300, 500 and 700°C was 92%, 77% and 47% respectively for the specimens cooled gradually. The results agreed with that obtained by other researchers deals with normal concrete, [Neville and Brooks 1987] and [Al-khafaji 2010] and for the specimens which cooled suddenly (high rate of cooling), the residual compressive strength was slightly lesser than that for gradual cooled specimens, it was 86%, 70% and 40% respectively for the same burning temperature. This may be due to the grading progression of decreasing temperature (cooling), which will never be uniformly through the concrete cross section, because losing temperature will delay for the inner concrete than that of the outer concrete, this process will create internal damaged stresses, and it will be worse with increasing the cross section of the concrete member. [Mohamedbhai 1986] conclusions agreed with these results till 500°C (for the normal concrete) but in contrast with that at 700°C , his conclusion

was, cooling rate affects on the residual concrete strength till 600 °C temperature, but it had no effect at more than this temperature, this may be because of using electrical furnace which can not allow to control the real cooling rate because of the delay time between the end of the exposure temperature and the cooling process.

When the strength of concrete cubes increased, the residual compressive strength percent is decreased, generally, this decrease is little. The maximum decrease in the percent of residual strength when the concrete strength increased from 20 MPa to 30 MPa is 6% for gradual cooling and 3% for sudden cooling, while the maximum decrease in this percent when the concrete strength increase from 20 MPa to 40 MPa is 9% for gradual cooling and 7% for sudden cooling.

Modulus of Rupture:

The effect of the elevated temperature and method of cooling on the modulus of rupture is similar to the effect of these factors on the compressive strength, these effects are shown in **Figs. 5-A, 5-B and 5-C**. For the prisms of 20 MPa nominal compressive strength, the percent of residual modulus of rupture after exposing to 300, 500 and 700 °C was 93%, 80% and 40% respectively, for the slab specimens cooled gradually. While for the specimens which cooled suddenly (high rate of cooling), the residual modulus of rupture was slightly lesser than that for gradual cooled specimens, it was, 90%, 74% and 35% respectively at the same above elevated temperatures. This because of the formation of cracks due to increase in temperature, and a net of surface cracks appeared in all faces of prisms due to increase the difference in thermal expansion between the aggregate and cement paste. This difference in thermal expansion increased during the cooling process and had a big effect in sudden cooling method.

When the strength of concrete increased, the residual modulus of rupture percent is

decreased, generally, the decrease in modulus of rupture percent is little. The maximum decrease in the percent of residual modulus of rupture when the concrete strength increased from 20 MPa to 30 MPa is 6% for gradual cooling and 7% for sudden cooling, while the maximum decrease in this percent when the concrete strength increase from 20 MPa to 40 MPa is 9% for gradual cooling and 13% for sudden cooling.

Deflection:

All slab specimens were tested under two point loads as shown in **Fig. 6**. The exposing temperature and method of cooling affected the value of central deflection greatly. **Fig.7** shows the effect of temperature and cooling method on the central (maximum) deflection for specimens of 20, 30 and 40 MPa strength. The test results showed that the increasing of temperature resulted in increasing the deflection as shown in **Fig.7**. Also, the cooling method (rate of cooling) of specimens has a clear effect on the deflection values of burned specimens. Where the specimens cooled suddenly by spraying them with water have more deflection than the others cooled gradually by leaving them in air (for the specimens of the same concrete compressive strength and the elevated temperature). Slab specimens with 20 MPa concrete strength and gradually cooled, the increase in central deflection compared with the reference specimen is 5%, 33%, and 105% at burning temperature 300°C, 500°C and 700°C respectively. But for suddenly cooled specimens the deflection was greater than that of gradually cooled specimens, the increase in deflection compared with that of the reference was 25%, 52% and 118% at burning temperature of 300°C, 500°C and 700°C respectively. This because of the formation and propagating of the cracks due to the burning process, which had a great effects on the rigidity of the slab specimens, causing a high mid span deflection. Also,

the rate of cooling effects on this propagation and growing of cracks, where it increased as the rate of cooling increased, result in decrease the rigidity and increase in deflection. When the concrete strength of specimens increased, the central deflection decreased (for the same burning temperature and cooling method), as shown in **Fig. 8**, meaning that enhancing in rigidity by decreasing the deflection.

Flexural strength:

The results of testing the specimens after burning by fire flame furnace showed that the increasing of burning temperature resulted in reducing the flexural strength. Also, the cooling method of specimens gives an important effect on flexural strength values of burned specimens. This may be because of the debonding between the reinforcement and the damaged concrete due to the difference in the thermal expansion them; also, the concrete may loss its compressive strength at the compression zone. The specimens cooled suddenly by spraying them with water they have less strength than the others which cooled gradually by leaving them in air, these effects are shown in **Table 9**. For the specimens of 20 MPa nominal compressive strength, the percent of residual strength after exposing to 300 , 500 and 700° C was 81.5%, 75% and 62.3% respectively, for the specimens cooled gradually. While it is for the specimens which cooled suddenly (high rate of cooling), the residual bending strength was slightly lesser than that of gradual cooled specimens, it was 77.9%, 68.3% and 58.3% respectively. When the strength of concrete specimens increased, the residual flexural strength percent is increased. Generally, the increase in flexural strength is little. The maximum increase in the percent of residual strength when the concrete strength increased from 20 MPa to 30 MPa is 6% for gradual cooling and 3% for sudden cooling, while the maximum increase in this percent when the concrete strength increase from 20

MPa to 40 MPa is 9% for gradual cooling and 7% for sudden cooling. The nominal bending strength is calculated from the equation:

$$\therefore M_n = \rho b d^2 f_y (1 - 0.59 \rho f_y / f'_c)$$

Where:

Mn= nominal bending strength.

ρ = percent of steel with respect to effective sectional area (b*d)

b= slab width

d=effective slab depth.

From the results above, there is a good agreement between theoretical and actual bending strength for the control specimens, the maximum difference between them is 6 % .

Conclusions

Based on the results obtained in this investigation, the following can be concluded:

- The strength of concrete, degree of burning temperature, method of cooling affect the residual compressive strength of concrete, modulus of rupture of concrete, deflection and flexural strength of slab specimens.
- The increase in the degree of burning temperature decreased the residual compressive strength of concrete , modulus of rupture of concrete and flexural strength of slab specimens, while it increased deflection. For (20 MPa) nominal compressive strength, the percent of residual compressive strength after exposing to 300C, 500C and 700 C and cooling gradually was 82%, 77% and 47% respectively. While for the same exposing temperature and the same method of cooling ,the percent of residual modulus of rupture was 93%, 80% and 40% respectively, the percent of residual flexural strength of slab specimens was 81.5%, 75% and 62.3% respectively, the increase in



- Central deflection of slab specimens was 5%, 33%, and 105% respectively.
- When the strength of concrete cubes increased, the residual compressive strength after burning is decreased, while there is a little increase in flexural strength of slab specimens. For central deflection percent there is a slight increase for burning temperature 300C and 500C and a significant decrease for 700C burning temperature.
- When the specimens were cooled suddenly, there is an decrease in the residual compressive strength percent, residual modulus of rupture percent and residual flexural strength percent, while there is an increase in the central deflection percent compared with the gradual cooling. Generally the decrease in residual strengths and increase in central deflection percent was little.
- The results showed that there is a good agreement between theoretical and actual flexural strength of reference specimens, the maximum difference between them is 6%.

Reference:

- Al Khafaji, M., 2010, "Effect of Burning on Load Carrying Capacity of Reinforced Concrete Columns", Ph.D. Thesis submitted to the University of Baghdad.
- ASTM Designation C33-03 "Standard Specification for Concrete Aggregate", 2002 Annual Book of ASTM Standard, American Society for Testing and Material, Philadelphia Pennsylvania, Section4, Vol. 4.02. PP 10-16
- Harada, T., Takada, J., Vamane, S., and Furumura, F., 1972, " Strength,
- Elasticity and Thermal Properties of concrete Subjected to Elevated Temperature ", ACI Special Publication, SP-34, V.1, pp337-401.
- Jeremy Chang, Andrew H. Buchanan, Rajesh Dhakal and Peter J. Moss, 2006, "Analysis of Hollowcore Concrete Floor Slabs under Fire", University of Canterbury, Department of Civil Engineering, Private Bag 4800, Christchurch, New Zealand

- Lau A. and Anson M., 2006, "Effect of High Temperatures on High Performance Steel Fibre Reinforced Concrete", *Cement and Concrete Research*; 36:1698–1707
- Mehrafarid Ghoreishi, Ashutosh Bagchi and Mohamed A. Sultan, 2010, " Estimating the Response of Flat Plate Concrete Slab Systems to Fire Exposure", *SIF'10 - Structures in Fire, Proceedings of the Sixth International Conference*, East Lansing, MI, USA, pp. 286-293
- Mohamadbhai, G.T.G., 1986, "Effect of Exposure Time and Rates of Heating and Cooling on Residual Strength of Heated Concrete", *Magazine of Concrete Research*, V136, September, pp 151-158.
- Neville, A. M. and Brooks, J. J., 1987, "Concrete Technology", First Edition, P318.
- Peter J. Moss, Rajesh Dhakal P., Way G. and Andrew H. Buchanan, 2008, " The Fire Behaviour of Multi-Bay, Two-Way Reinforced Concrete Slabs", Department of Civil Engineering, University of Canterbury, Private Bag 4800, Christchurch, New Zealand, Arup Fire, 1 Nicholson St, Melbourne, Victoria 3000, Australia
- Piasta, J., Sawiez. And Rudzinski, L., 1984, "Change in the Structure of Hardened Cement Paste Due to High Temperature", *RILEM. Materials and Struct.* V.17 No.100, pp291-296.
- Robiston, T.D., "High- Alumina Cement and Concrete ", *Construction Record Ltd. London*, 1962, pp 34-40.
- Venecanin, S.D., 1997, "Influence of Temperature on Deterioration of Concrete in Middle East", *Concrete Journal*, V.11, No.8, August, pp31-33.



Table 1: Physical properties of cement*

<i>Physical Properties</i>	<i>Test results</i>	<i>Limits of (I.O.S.) No.5/1984</i>
Specific surface area (Blaine method), m ² /kg	483	≥230
Setting time (Vicate apparatus), Initial setting, h:min Final setting, h:min	2:50 4:30	≥00:45 ≤10:00
Compressive strength, MPa 3 days 7 days	35.60 40.70	≥15.00 ≥23.00
Soundness (Autoclave) method, %	0.25	≤0.8

* Physical analysis was conducted by National Center for Construction Laboratories and Research.

Table 2: Chemical composition and main compounds of Cement*

<i>Oxides composition</i>	<i>Content %</i>	<i>Limits of (I.O.S.) No.5/1984</i>
CaO	62.21	-
SiO ₂	20.18	-
Al ₂ O ₃	5.00	-
Fe ₂ O ₃	3.60	-
MgO	2.31	<5.00
SO ₃	1.44	<2.80
L.O.I.	3.29	<4.00
Insoluble residue	1.11	<1.5
Lime Saturation Factor,L.S.F.	0.94	0.66-1.02
Main compounds (Bogue's equations)		
C ₃ S	57.04	-
C ₂ S	14.83	-
C ₃ A	8.60	-
C ₄ AF	10.95	-

- Chemical analysis was conducted by National Center for Construction Laboratories and Research.

Table 3: Chemical and physical sand test results. *

<i>Properties</i>	<i>Test results %</i>
Absorption%	0.82
Specific gravity	2.49
Sulfate content (SO ₃)%	0.32

*Test was conducted in the laboratories of engineering college-al -Anbar University

Table 4: Chemical and physical gravel test results. *

<i>Properties</i>	<i>Test results %</i>
Absorption%	0.64
Specific gravity	2.62
Sulfate content (SO ₃)%	0.05
Dry loose-unit weight kg/m ³	1562
Material finer than 75 µm%	1.36

*Test was conducted in the laboratories of engineering college-al-Anbar University

Table 5: Details of SCC mixes

<i>No.</i>	<i>Mix of strength(MPa)</i>	<i>Cement Kg/m³</i>	<i>Fine agg. Kg/m³</i>	<i>Coarse agg Kg/m³.</i>	<i>SP (Glenium51) Lit/m³</i>	<i>S.F Kg/m³</i>	<i>Water Lit/m³</i>
1	19.6 ≈ 20	400	600	640	12	8	228
2	28.8 ≈ 30	400	600	640	12	8	200
3	37.8 ≈ 40	500	600	640	15	10	200

Table 6: Properties of steel bars

<i>Approximate diameter(mm)</i>	<i>Measured diameter</i>	<i>Yield stress f_y (MPa)</i>	<i>Modulus of Elasticity(GPa)</i>	<i>Ultimate stress (MPa)</i>
3	2.93	800	195.924	950

*Test was conducted in the laboratories of engineering college-al-Anbar University

Table 7. Details of concrete slab specimens.

Group	Concrete Strength												Type of cooling
	20MPa				30MPa				40MPa				
	Temp. (°C)				Temp. (°C)				Temp.(°C)				
	NE	300	500	700	NE	300	500	700	NE	300	500	700	
A	1	-	-	-	1	-	-	-	1	-	-	-	-
B	-	1	1	1	-	1	1	1	-	1	1	1	Gradual.
C	-	1	1	1	-	1	1	1	-	1	1	1	Sudden.

NE = Note Exposed to Fire (Reference Specimen)



Table (8): Results of compression test for burned and reference cubes

Groups of Method Compressive $f'c$	Compressive Strength of Cubes				Method of Cooling
	*Reference Cube (MPa)	Burned Cubes (MPa)			
		Temperature of Burning			
		300°C	500°C	700°C	
Grade 20 MPa	19.6	18.03	15.09	9.21	Gradually
		16.85	13.72	7.84	Suddenly
Grade 30 MPa	28.8	25.63	20.45	12.96	Gradually
		24.48	19.29	10.94	Suddenly
Grade 30 MPa	37.8	32.51	25.70	15.87	Gradually
		30.99	23.81	12.47	Suddenly

* Control Specimens without burning.

Table 9: Maximum bending strengths of slabs

Compress. Strength f'_c	Maximum bending strengths of slabs (N.m)							
	Refer. slabs		Main slabs (burned slabs)					
	Nominal Bend. strength	Actual Bend. strength	300°C		500°C		700°C	
			Sudd.	Grad.	Sudd.	Grad.	Sudd.	Grad.
20MPa	925.98	900	701.25	733.5	615	675	525	561
30MPa	966.27	969.9	825	831.375	750	810	547.5	701.25
40MPa	986.526	1050	945	969.9	831.375	900	675	750

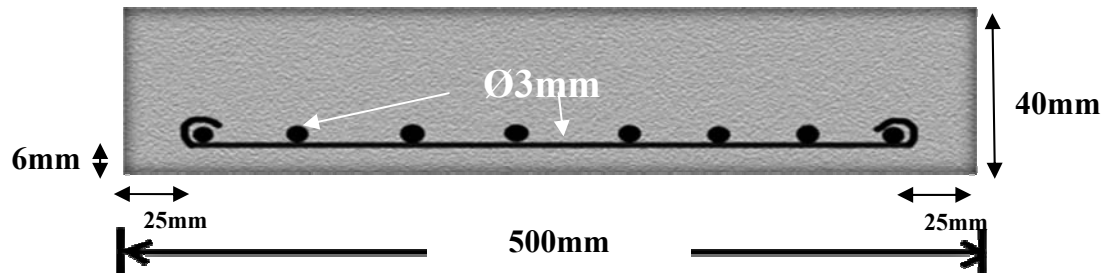


Figure 1: Side Cross Of Slab

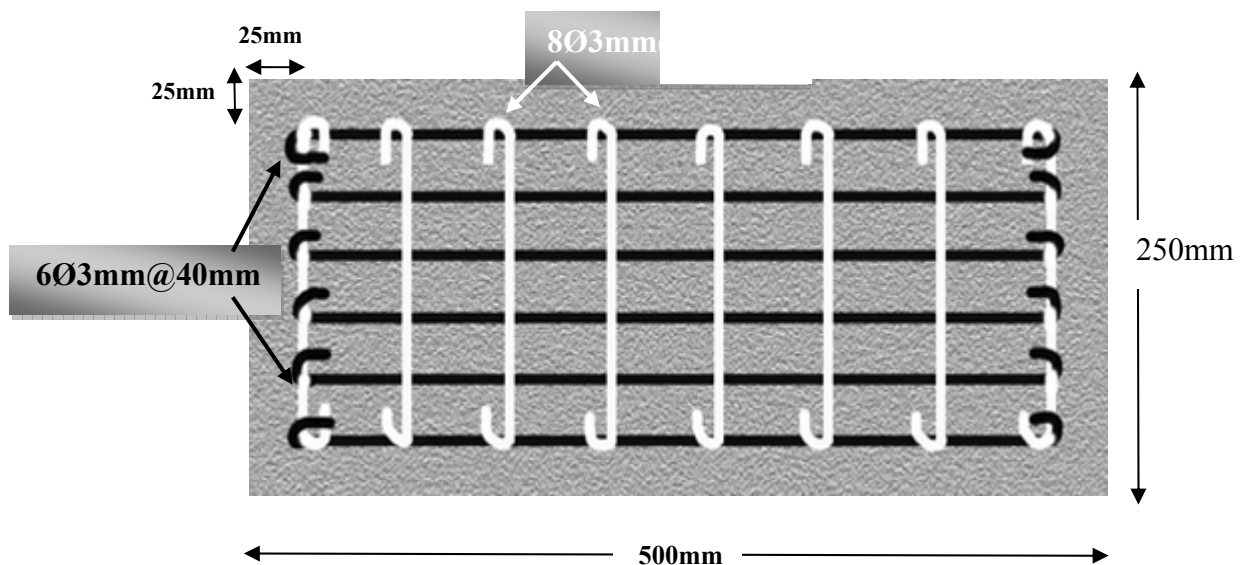


Figure 2: Top View Of Slab With Reinforcement Details



Figure 3: Flame Furnace

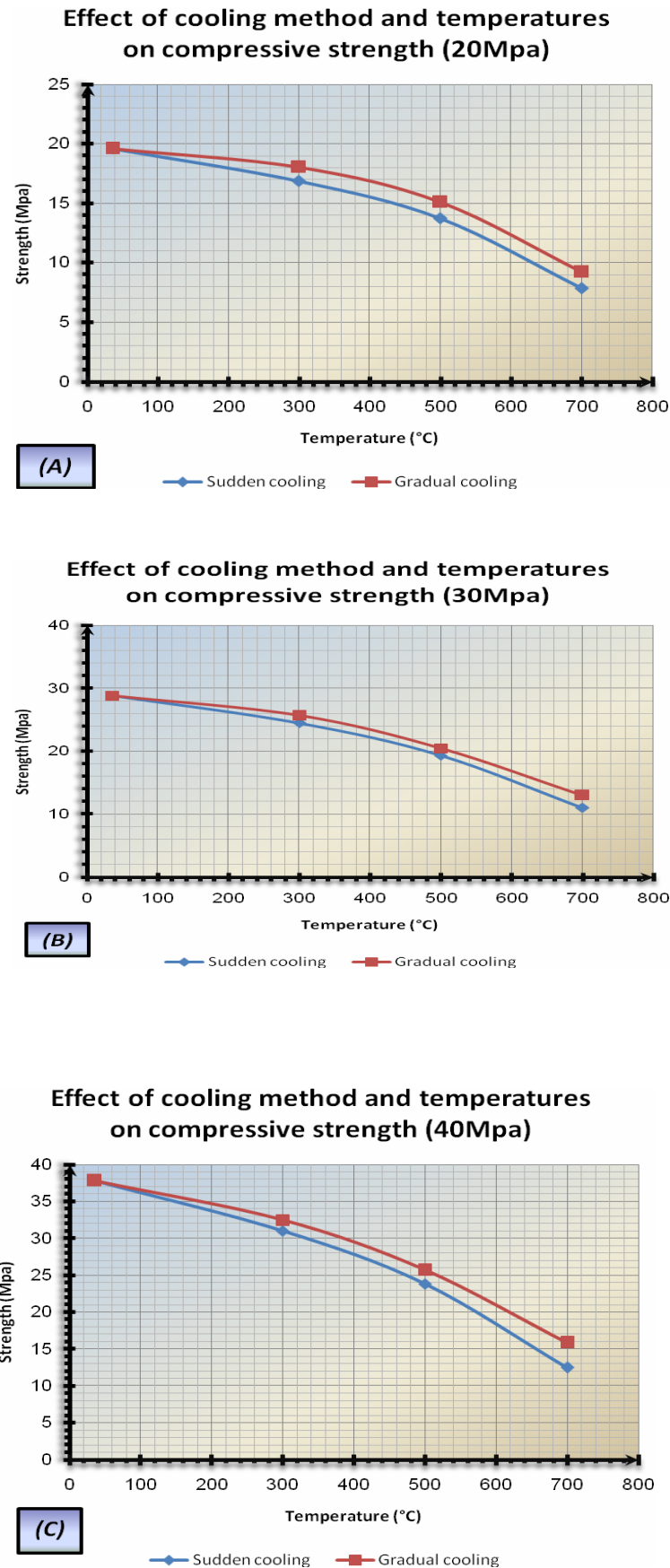


Figure 4: Effect of Cooling Method and Temperatures on Compressive Strengths

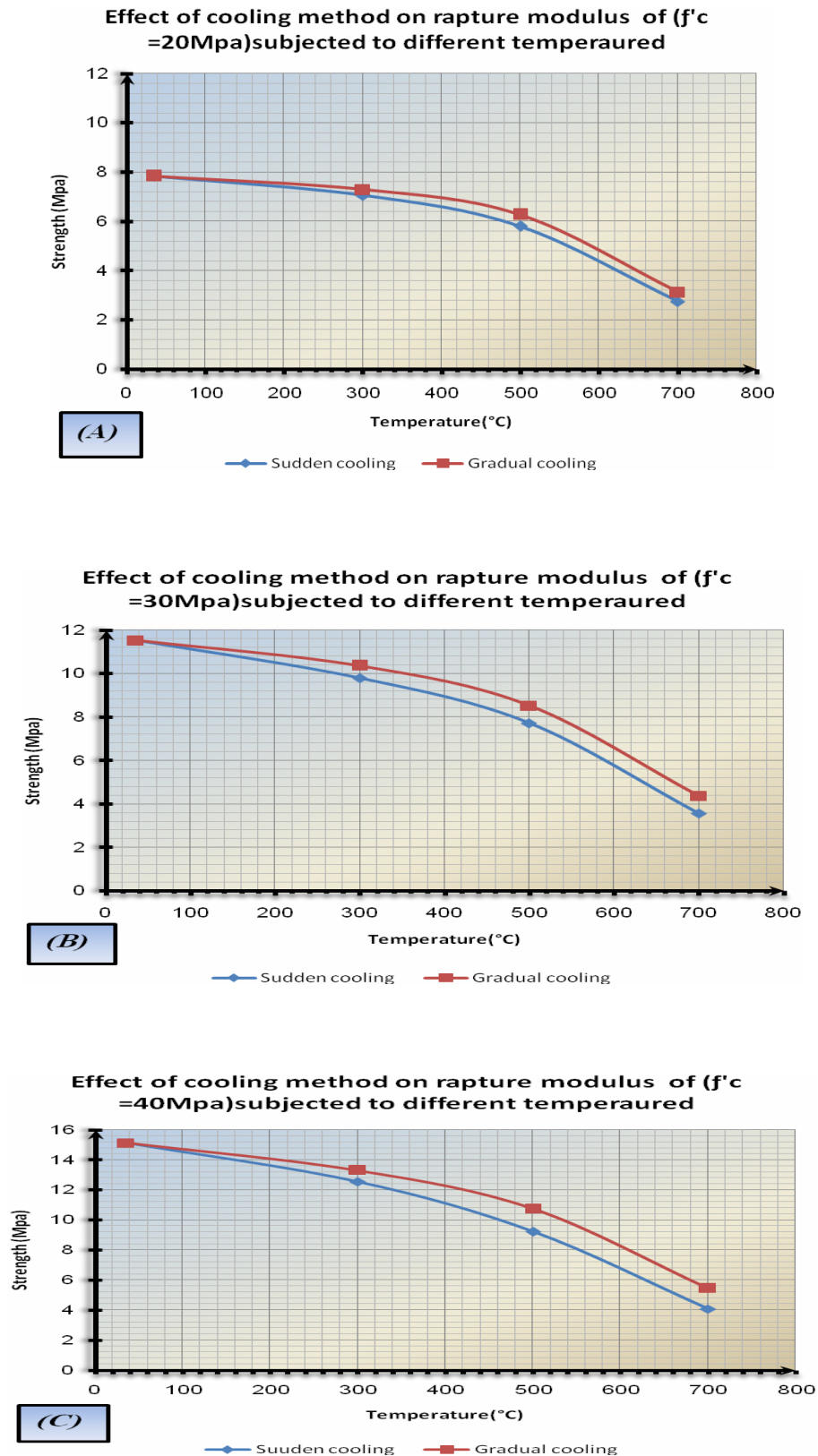
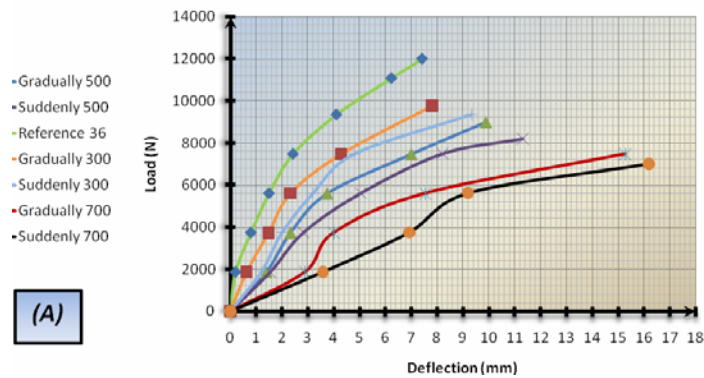


Figure 5: Effect of Cooling Method and Temperatures on Modulus of Rupture

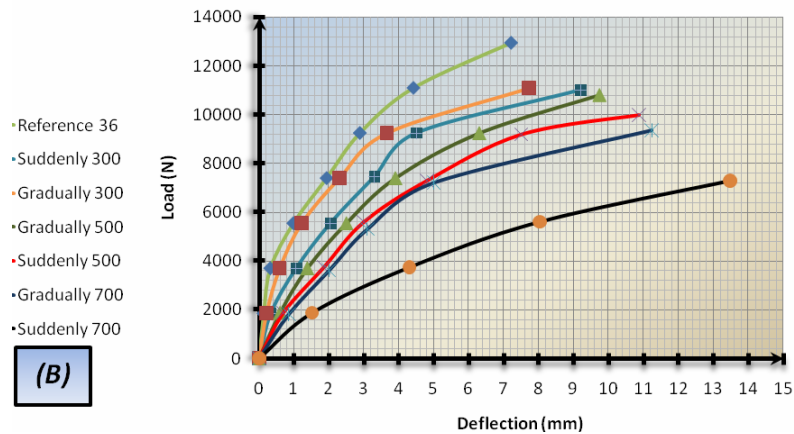


Fig. 6: Testing Of Specimens Under Two Point Loads.

*The effect of temperature and cooling method
on the load-deflection relation for $f_c=20$ Mpa
slabs*



*The effect of temperature and cooling method
on the load-deflection relation for $f_c=30$ Mpa
slabs*



*The effect of temperature and cooling method
on the load-deflection relation for $f_c=40$ Mpa
slabs*

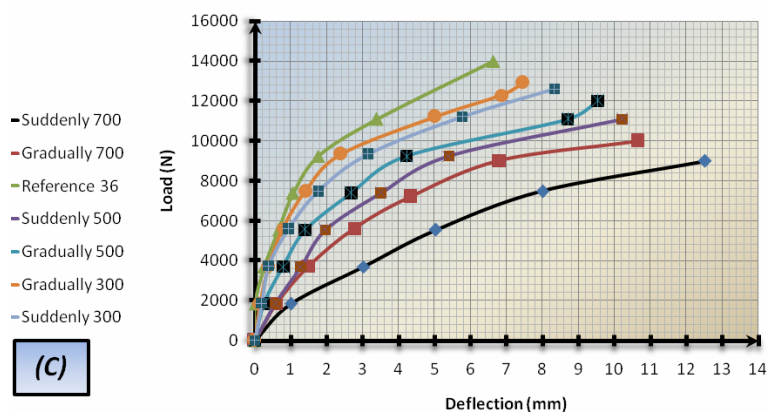


Figure 7: The Load-Deflection Relations For ($f_c=20, 30, \& 40$ Mpa) Slabs In The Temperatures (300, 500, & 700°C) With Both Cooling Method

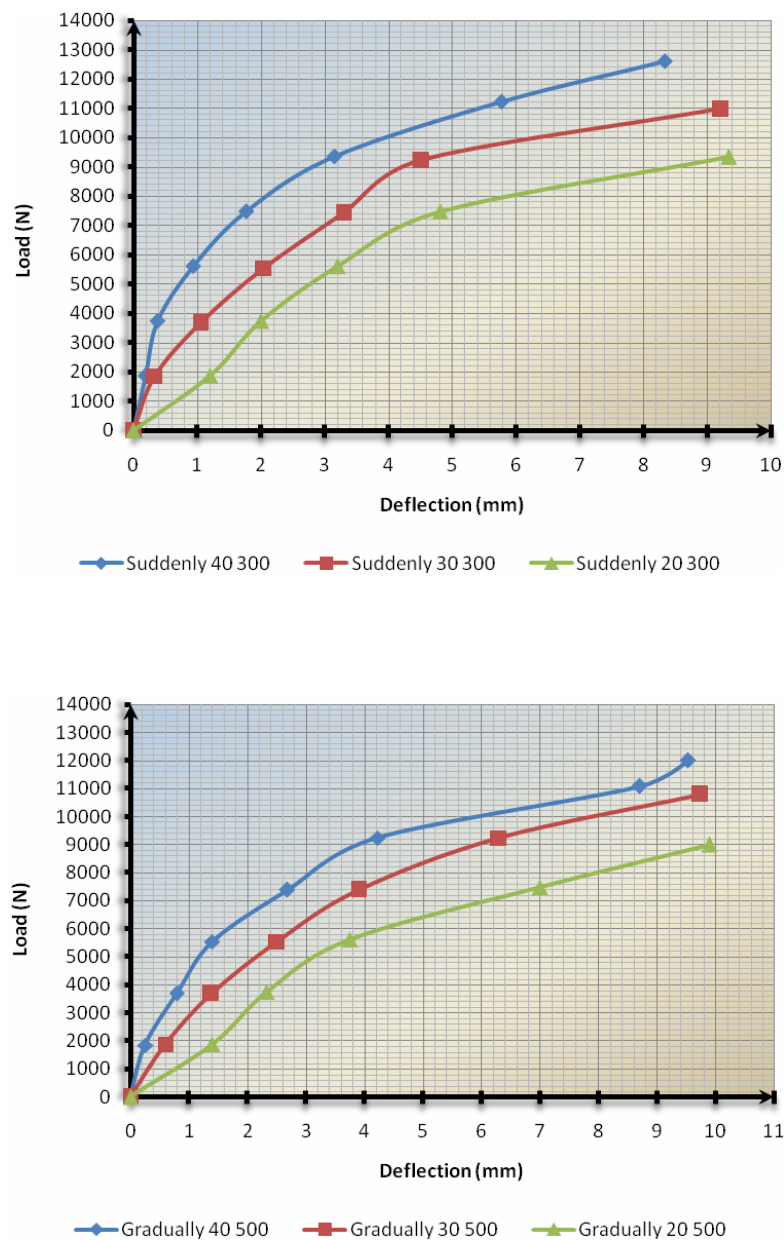


Figure8: The Load-Deflection Relation For Burned Slab Specimens Had Different Concrete Strength In Both Cooling Methods At 500°C.



Prediction of Smear Effect on the Bearing Capacity of Driven Piles

Dr. Ala'a Hussein. Alwan Al-Zuhairi
Lecturer, Eng. College-Civil Dept.
Baghdad University
Email: alaawn@yahoo.com

Hayder Alwan Mahdi
Ass. Lecturer, Eng. College-Civil
Dept Baghdad University
Email: civil_hayder1974@yahoo.com

Saif Mohammed Jawad
Ass. Lecturer, Eng. Dept.
Baghdad University
Email: s1981aif@yahoo.com

Abstract

This paper deals with prediction the effect of soil remoulding (smear) on the ultimate bearing capacity of driven piles. The proposed method based on detecting the decrease in ultimate bearing capacity of the pile shaft (excluding the share of pile tip) after sliding downward. This was done via conducting an experimental study on three installed R.C piles in a sandy clayey silt soil. The piles were installed so that a gap space is left between its tip and the base of borehole. The piles were tested for ultimate bearing capacity according to ASTM D1143 in three stages. Between each two stages the pile was jacked inside the borehole until a sliding of about 200mm is achieved to simulate the soil remoulding due to actual pile driving. The results of the tests exhibited that the pile might loss 14% of its ultimate capacity when it is loaded immediately after installation. Also, it was concluded that the pile may regain of about 9% of its original capacity after 30days of its installation.

Key words: Driven piles, bearing capacity, smear, soil remoulding, pile testing.

()

ASTM D1143
200 ()
()
%9 %14
30

1. Introduction

Piles are structural members usually used to transfer the bearing loads coming from structure they support to the deeper strong strata. According to the method of their installation, piles can be divided into two groups:

- (a) Displacement piles, and
- (b) Non displacement piles

Driven piles and preformed-cast in place piles are examples of displacement piles. Driven piles may be of a solid section made of timber, steel or concrete or hollow steel section. The second type of displacement piles (driven cast-in place piles) is formed by driving a close-ended tube into the ground then it is filled with concrete. Non displacement pile is created when a void is formed into the ground by boring or excavation then the void is filled with concrete.

The method of pile installation may have profound effects on its behavior under load (Polous and Davis). It is easy to recognize that these effects are mostly related with displacement piles since the method of their installation generally creates more disturbance than other methods.

1.1 Effect of Type of the Soil

On the other hand, the type of surrounding soil has a role in magnification or minimization of the installation effects on pile performance.

(a) In clays:

de Mello (1969) classified the effects of pile driving in clays into three classes:

1. Remoulding (smear) of soil particle structure closed to the pile shaft.
2. The stress state of the soil is changed after pile driving due to soil densification i.e. increasing the horizontal stress.
3. Developing of the excess pore pressure then dissipation with time.

Lee et al. (2003) concluded that the state of the soil (density and stress state) is changed significantly when a pile is driven into the ground. D. Basu et al. (2005) noticed that pile driving preloads the surrounding soil, resulting in a greater base resistance than that observed for bored (non-displacement) piles. They found higher ratio of base share of pile capacity to its total capacity (q_b/q_c) for displacement piles than that for geometrically

identical non displacement piles (q_b = capacity of the pile base and q_c = total capacity of the pile). As it is seen the capacity of pile shaft is decreased due to effects of pile driving. Generally, it may be expected that pile driving process in clay will cause initially loss in undrained shear strength of clay due to remoulding at constant moisture content (Polous and Davis).

Concerning the pore pressures developed during pile driving, a number of measurements have been made. As stated by (Polous and Davis) a summary of some measurements of the variation with radial distance of the excess pore pressure around a single driven pile are given in Fig. 1. In this figure the normalized excess pore pressure is

indicated $\frac{\Delta u}{\Delta \sigma'_{vo}}$ where Δu is the excess pore

pressure and $\Delta \sigma'_{vo}$ is the vertical effective stress in the soil prior to driving. It is seen there is a considerable scatter in the points resulting largely from differences in soil type. The larger pore pressure being associated with the more sensitive soils. However, D'Appolonia and Lambe (1971) derived eq.(1) to estimate the maximum pore pressure developed near the pile surface.

$$\frac{\Delta u}{\Delta \sigma'_{vo}} = \left[(1 - k_o) + \frac{2S_u}{\sigma'_{vo}} \right] A_f \quad (1)$$

Where,

Δu_m = maximum excess pore pressure

K_o = in situ coefficient of earth pressure at rest

S_u = undrained shear strength

A_f = pore pressure coefficient A at failure

σ'_{vo} = initial vertical effective stress in soil

(b) In sands:

The soil is compacted by displacement and vibration resulting from permanent rearrangement and some crushing of the particles. The pile capacity is increased when the soil is in loose condition due to increase in relative density caused by pile driving. Kishide (1967) proposed a simple method to estimate the effect of driving a pile in loose sand. He assumed that the diameter of the compacted zone around the driven pile is seven



times the pile diameter (d). Also, he assumed that the change in angle of friction ϕ' is linear with the distance from the original value of ϕ'_1 at the pile tip as clarified in eq.(2) (see Fig. 2):

$$\phi'_2 = \frac{\phi'_1 + 40}{2} \quad (2)$$

From eq.(2) it is concluded that when $\phi'_1 = 40^\circ$, which is the case of dense sand, there is no change in relative density due to pile driving.

Paik and Salgado (2004) investigated the effect of pile installation method on pipe pile behavior (penetration parameters and bearing capacity) in sands via calibration chamber test conducted on model pipe piles installed in different sandy soil conditions. They concluded that the pile capacity is increased with increasing hammer weight at the same driving energy and with increasing hammer weight at the same fall height. Finally, they observed that the jacked piles have higher bearing capacities than identical driven piles under similar conditions.

2. Experimental Works

To performer the goal of this study, an experimental program is conducted on two stages:

2.1 Laboratory Stage

In this stage routine classification tests were conducted on disturbed samples taken from three boreholes prepared for piles. The tests consist of specific gravity, Aterberg limits and grain size distribution. The results of some of these tests are listed in Table 1 and others are shown in Fig. 3. Although soil samples were extracted from different depths, the results of the tests showed almost the same physical properties. Moisture content, unit weight and unconfined compression tests were excuted on undisturbed samples taken from the three drilled boreholes. The results of these tests were tabulated in Table 1.

The aggergates prepared for concrete piles (sand and gravel) were also tested for gradation and undesirable matter content according to Iraqi Standard (IQS 45:1984). The sulphate resistance cement is tested for physical properties according to (IQS 5:1984). A concrete mix was designed to achieve 28-days compressive strength of 30MPa following the proceduer given by ACI 211.1-91. The results of tests and mix proportions are listed in Table 2.

Table 1: Physical and Mechanical properties of the ground soil

Property	Depth of sample (m)	Borhole(1)	Borhole(2)	Borhole(3)
Specific Gravity, G_s	0.75	2.67	2.71	2.72
	1.75	2.76	2.74	2.80
	2.75	2.75	2.73	2.78
Liquid limit, L.L (%)	0.75	33.2	32.7	31.4
	1.75	35.5	38.0	34.8
	2.75	38.8	37.8	39.2
Plasticity index, P.I (%)	0.75	12.0	11.8	12.2
	1.75	13.6	14.1	13.0
	2.75	14.5	15.8	14.2
Moisture content, w_c (%)	1.0	16.2	15.8	16.3
	2.0	17.0	17.2	16.8
	3.0	17.2	17.4	17.4
Dry Unit weight, γ_d (kN/m ³)	1.0	16.88	16.74	16.26
	2.0	17.01	16.92	16.85
	3.0	16.98	16.84	16.91
Unconfined compression, q_u (kPa)	1.0	78.1	79.1	77.4
	2.0	112.6	108.4	112.0
	3.0	118.7	116.8	117.1

2.2 Field Stage

Pile installation

Three 150mm diameter boreholes were drilled to a depth of 3m below ground level in the University of Baghdad near Al-Khawarizmi Engineering College at Al-Jadiriya using the hand auger. No water table was distinguished in all boreholes. To make side skin friction of pile is the only active component of the pile capacity (i.e. to vanish the tip component of the bearing capacity) during pile loading, a gap is left between concrete pile tip and the end of boring. This was made by utilizing a circular steel plug plate fixed at the bottom of reinforcement cage of the pile as shown in Fig. 4. The reinforcement cages were placed in the boreholes so that the piles are installed leaving a gap distance of 500mm between pile tip and borehole base. Then the concrete is poured inside the holes with light compaction to the final top level which is achieved by using a PVC pipe mould as shown in Fig. 5.

Pile testing

After casting, the piles are left for thirty days to permit for concrete maturation. Then each of the three installed piles are subjected to the following procedure of loading and unloading using a hydraulic jack of 35ton capacity, 0.01mm dial gage, reference beam and steel pipe of closed ends as a loading column. The cantilever beams of neighbor building are employed as reaction beams

during pile testing. The details of the loading apparatus are shown in Fig. 6:

1. The pile was loaded according to the method described in ASTM D1143. The theoretical estimated maximum bearing load of the pile was incremented into four equal 25% increments. In each increment, the applied load is maintained by continuously jack force increasing until the rate of settlement that specified in ASTM D1143 (0.25mm/hr) is reached. Incremental loading was continued by jacking the pile until a settlement of about 15% of the pile diameter is obtained or when the pile can not carry any additional load whichever is nearest. In the present work all piles failed by the former criterion. Then the load is removed in decrements of 25% of the total load with one hour between decrements and settlement recovery of the pile is recorded.
2. After this stage of testing, the pile is driven to about 200mm inside the borehole by rapid continuous jacking on its head. This stage simulates the effects of particles remoulding (smear) of the surrounding soil during pile driving.
3. The piles are left for 0, 10 and 30 days before the next cycle of loading is resumed.
4. The second cycle is conducted following steps (1), (2) and (3) mentioned above.
5. The last cycle is done following the same instructions of step (1).

The results of the test of the three piles can be seen in Figs. 7.

Table 2: Material properties and concrete mix proportions

Material Properties	Cement		Water	Fine agg. (sand)		Coarse agg. (gravel)		
	Property			Results	Seive size (mm)	Passing by weight (%)	Seive size (mm)	Passing by weight (%)
	Initial setting time (min)			56	10	100	37.5	100
	Final setting time (hr)			3.5	4.75	92.0	20	98.5
	Compressive strength (MPa)	3 days		18.2	2.36	75.6	10	41.4
		7 days		24.1	1.18	53.2	5	0.9
	Fineness (m ² /kg)			273	0.6	33.0		
					0.3	17.6		
					0.15	8.2		
					SO ₃ (%)	0.23	SO ₃ (%)	0.067
			Fines (%)	4.7	Fines (%)	0.2		
Final result	Pass			Pass (Zone 2)		Pass (grade 20-5)		
Conc. mix proportions	1		0.487	1.632		2.241		



3. Results and Discussion

Fig. 7 shows the load-settlement curves for the tested piles in three cycles of loading. The curves of the first cycle for all three piles exhibit almost the same trend since the piles are distributed in rather small area of ground, the case in which the same condition of soil is predominated as it was clarified in Table 1. Generally, the curves exhibit a decrease in ultimate pile capacity at second and third cycles for a given settlement. This is attributed to the decrease in shear strength of the surrounding soil due to particle remoulding (smear) that caused capacity. This finding comes compatible with the observation of Polous and Davis (1980). They described the regain with time of lost shear strength of the surrounding soil due to pile driving as a thixotropic regain of undrained strength as the structural bonds destroyed by remoulding are at least partially restored.

To study the effect of surrounding soil remoulding (i.e. smear) caused by shaft sliding on pile bearing capacity, the maximum measured pile capacity in each cycle of each pile were plotted against the number of cycle in Fig. 8. The calculated theoretical average maximum pile capacity was also indicated on the same figure. The curves indicate a decrease in maximum pile capacity in a range of (1.9-6.3)kN which represent a (4.3-14)% of the theoretical average maximum capacity. The effect of time lag between loading cycles (smear aging) on the regain of destroyed adhesion between pile shaft and surrounding soil is clarified in Fig.9. The piles regained (2.5-4.6)% after 10days and (3.5-9.4)% after 30days of the original measured ultimate pile capacity.

4. Conclusions

From the results of the experimental work that executed during this study, the following conclusions can be drawn:

1. The proposed new method is based on destroying the adhesion bond between pile shaft and surrounding soil by sliding the pile shaft without tip resistance after installation to simulate the effect of soil remoulding due to actual pile driving.
2. 14% of the ultimate pile capacity may be lost when it is loaded immediately after installation while only 4.6% may be lost when the pile loaded after 30days.

by driving of the pile shaft. The decrease in shear strength of a soil when its particles remoulded is referred to sensitivity which is a property of the cohesive soils. In this study, the tested soil was found generally plastic silt (see Fig. 3). The plasticity came from the ability of the soil to absorb water and transfer from plastic to liquid state (i.e. plasticity index) see Table 1. This may stand behind its behavior after remoulding that caused by pile driving. The decrease in pile capacity was found dependent on time lag between cycles. The more the time lag between the cycles the less decrease in pile

3. When linear variation is assumed for shear strength lossing and regining during pile driving, the regain of the lost shear strength may be taken equals the regain of measured pile capacity after a certain time period. Consequently, a percentage of (2.5-4.6)% of the original shear strength of the soil is regained after 10days and (3.5-9.4)% after 30days of the pile installation.

References:

- ACI Committee 211, 2008, "Standard Practice for Selecting Proportions for Normal, Heavyweight, and Mass Concrete." (211.1-91), American Concrete Institute, Detroit.
- ASTM D1143-81 (reapproved 1994), "Standard Test Method for Piles under Static Axial Compressive Load", Annual Book of ASTM Standards, Vol. 04.08, New York, USA.
- Basu, D., Salgado, R., Prezzi, M., Lee, J. and Paik, K., "Recent Advances in the Design of Axially-Loaded Piles in Sandy Soils", 2005, Advances in Deep Foundation, ASCE, (Downloaded from the site www.ascelibrary.org).
- D'Appolonia, D.J. and Lambe, T. W., 1971, "Performance of Four Foundations on End-Bearing Piles", Soil Mechanics and Foundation Engineering Journal, ASCE, Vol. 97 SM10, pp. 77-93.
- de Mello, V.F., 1969, "Foundation of Buildings on Clay.", Proceeding of 7th International Conference in Soil Mechanics and Foundation Engineering, Mexico City, pp. 49-136
- Head, K.H., 2006, "Soil Laboratory Testing", Volumes 1, 2 and 3, 3rd Edition, Whittles Publishing, Scotland, U.K.

Kishida, H., 1967, "Ultimate Bearing Capacity of Piles Driven into Loose Sand.", Soils and Foundations, Vol.7 No.3, pp. 20-29

Lee, J. H. Salgado, R. and Paik, K. (2003), "Estimation of the Load Capacity of Pipe Pile in Sand Based on Cone Penetration Test Results.", Journal of Geotechnical and Geoenvironmental Engineering., ASCE, Vol. 127 pp. 3-16.

Paik, K. and Salgado, R., "Effect of pile Installation Method on Pipe Pile behavior in Sands", Geotechnical Testing Journal (GTJ), Vol. 27, Issue 1 (January 2004).

Poulos, H.G. and Davis, E.H., "Pile Foundation Analysis and Design.", 1980, Rainbow-Bridge Book Co.

Weltman, A. and Little, J., "A Review of Bearing Pile Types" Directorate of Civil Engineering Services (DOE) and Construction Industry Research and Information (CIRIA) Report PG1, 1977 London.

" (IQS 5:1984)

8 1984

" (IQS 45:1984)

8 1984

Legend:

- Wallaceburg (Lo and Stermac, 1965)
- △ Ghost River (Lo and Stermac, 1965)
- Wabi River (Lo and Stermac, 1965)–(29 ft depth)
- Wabi Riber (Lo and Stermac, 1965)–(37 ft depth)
- × Marine Clay (Bjerrum and Johannessen, 1960)–(7.5 m depth)
- ▲ Marine Clay (Bjerrum and Johannessen, 1960)–(10 m depth)
- ▽ Firm Clay (Airhart et al., 1969)–(40 ft depth)
- + Boston Blue Clay (D'Appolonia and Lambe, 1970)
- Varved Clay (Soderman and Milligan, 1961)–(20 ft depth)
- ▼ Varved Clay (Soderman and Milligan, 1961)–(25 ft depth)
- ◇ Varved Clay (Soderman and Milligan, 1961)–(30 ft depth).

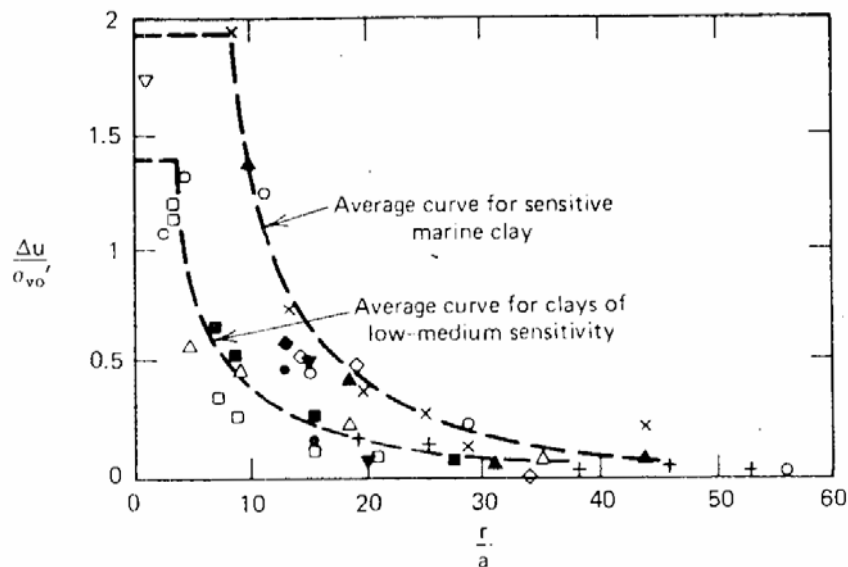


Fig. 1: Summary of measured pore pressures (Polous and Davis, 1980)

Note: $\frac{r}{a}$ = the ratio between the distance from pile center to point at which the pore is measured to the diameter of the pile

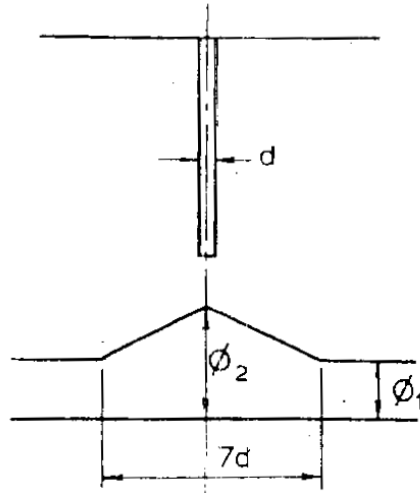


Fig. 2: Effect of pile driving on the angle of internal friction (ϕ) in sand (Kishida, 1967)

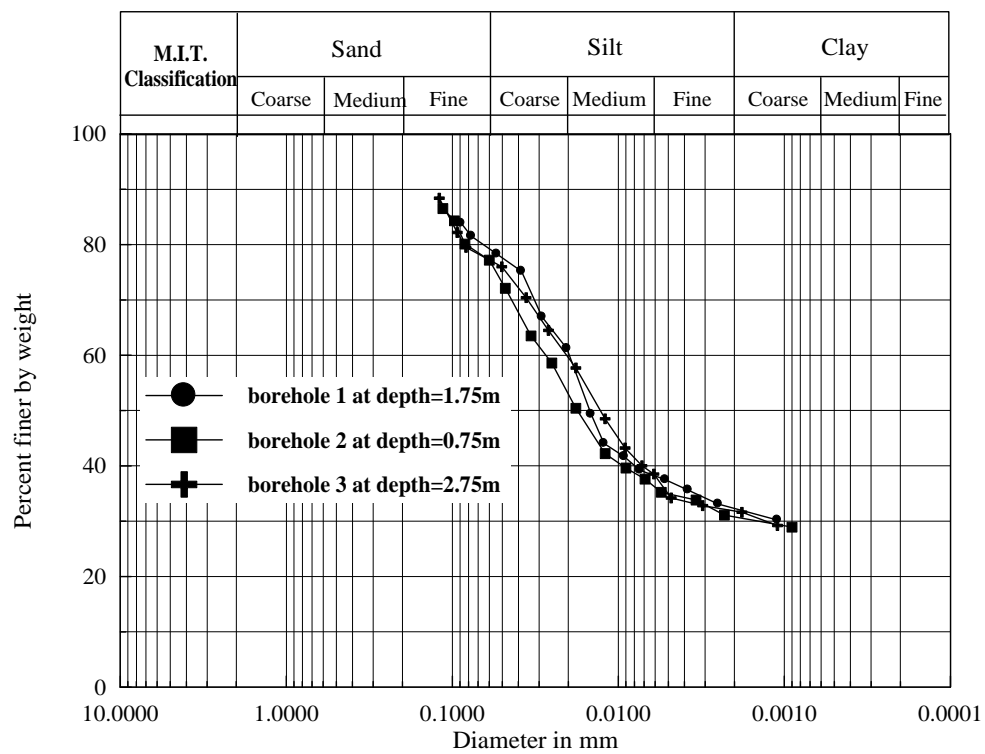


Fig. 3: Grain size distribution of the soil

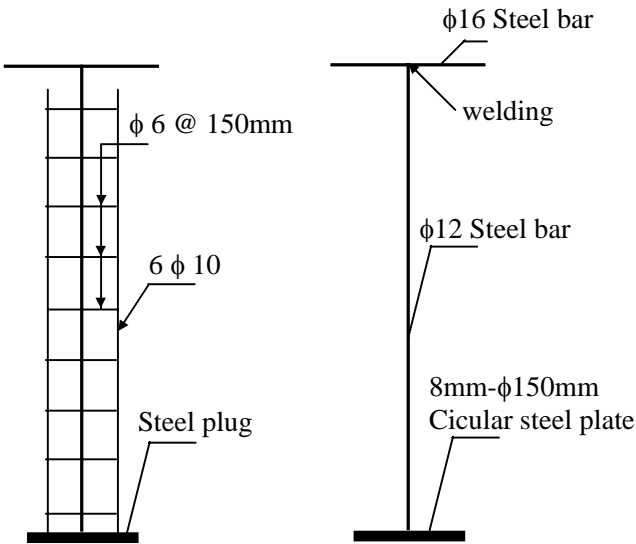


Fig. 4: Pile reinforcement and plug details

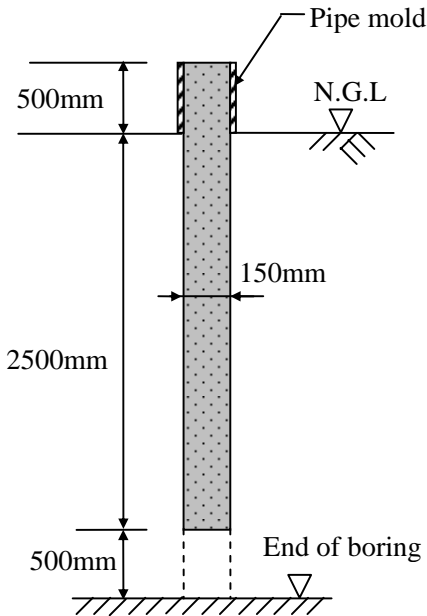


Fig. 5: Pile installation feature

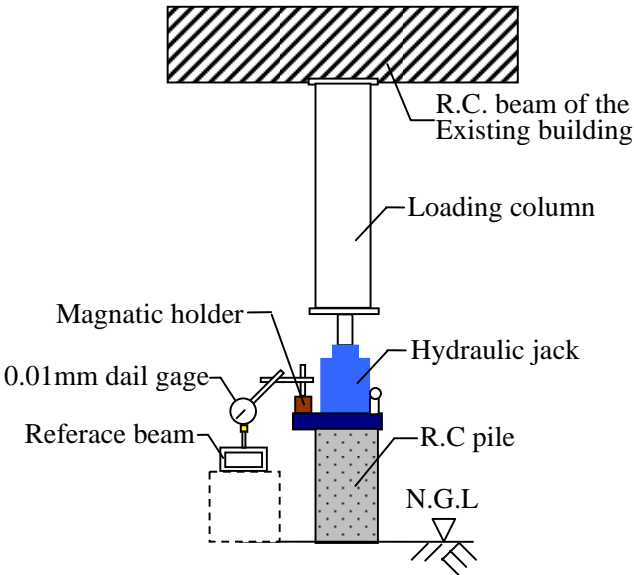
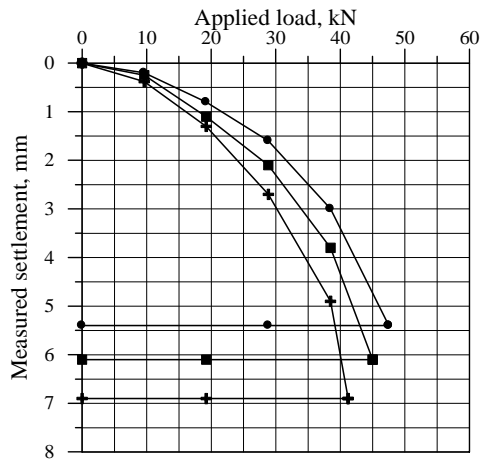
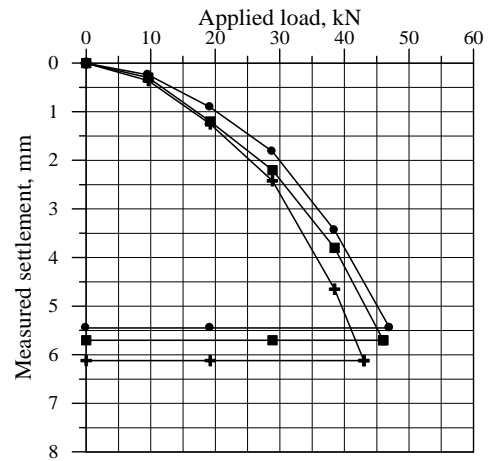


Fig. 6: Loading Apparatus

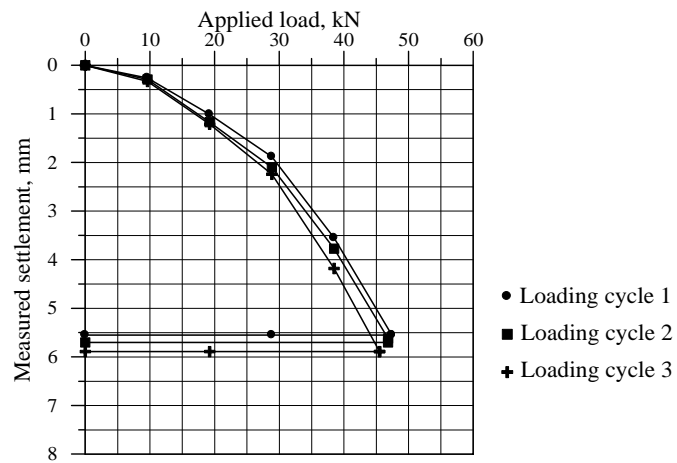




(a) Pile no.(1)



(b) Pile no.(2)



(c) Pile no. (3)

Fig. 7: Load-settlement curves

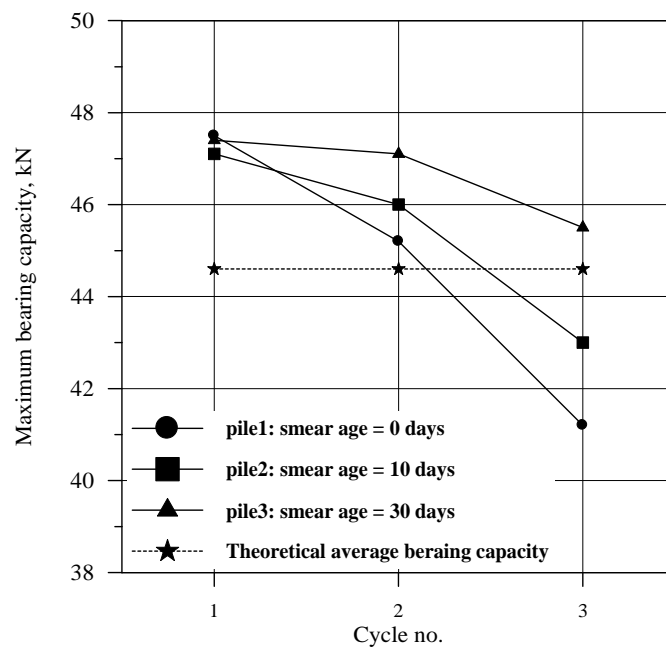


Fig. 8: Maximum measured and theoretical bearing capacities of the piles

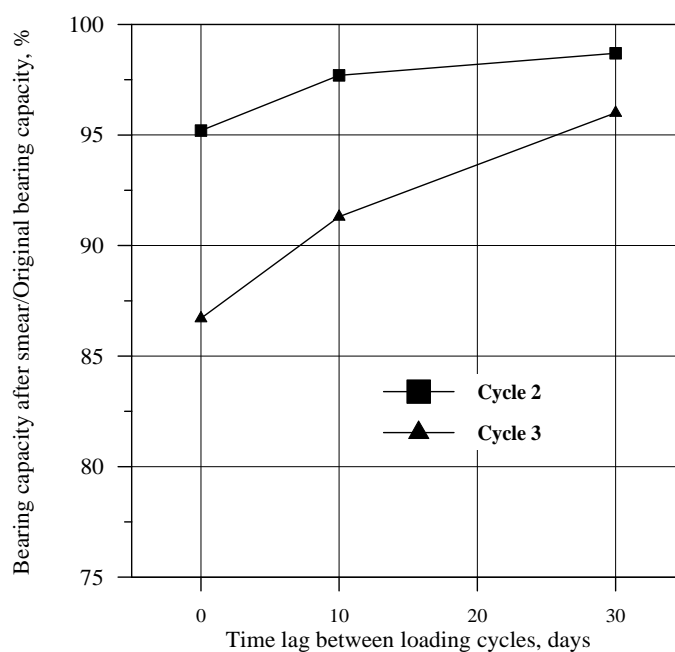


Fig. 9: Effect of smear aging on pile capacity restoring



Self Purification in Al-Saqlawiya Drain in Abu-Grebe

Dr. Jathwa Abdul Karime Ibraheem

A lecturer in Environmental Engineering Department

College Of Engineering

University Of Baghdad

E-mail:jathwa58@yahoo.com

Abstract

Surface water flow samples were collected with distances downstream over Saqlawiya main drain whose stretch of about 24.5 km. The drain travels through different land use pattern, before, flowing into Tigris River. Eight sampling points were carefully selected downstream the channel during dry season. The examined water parameters were pH, NH_3 , NO_3^- , $\text{PO}_4^{=}$, BOD_5 , COD, TDS, S.S, Cl^- , $\text{SO}_4^{=}$, Na^+ , Ca^{+2} , Mg^{+2} , and Oil and Grease.

Descriptive and inferential methods through finding the best curve fit correlation were employed in the study to test the strength of the association between water chemical characteristics and distance downstream the channel.

A comparison of the values of chemical parameters at the Al-Saqlawiya Drain-Tigris River meeting shows that nine parameters (i.e. pH, NH_3 , NO_3^- , $\text{PO}_4^{=}$, BOD_5 , COD, TDS, S.S, and Oil and Grease) out of the 14 parameters under study decreased in their concentration at meeting point.

In a further analysis, predictive models were obtained through using six sampling points (0, 1, 3, 5, 7, 8) and leaving three (2, 4, 6) as activation function.

The percentage error for the calculated values of pH, NH_3 , BOD_5 , COD, TDS, Cl^- , $\text{SO}_4^{=}$, Na^+ and Mg^{+2} ranges from (0.54 to 15) % which demonstrate the high predictive capacity of the models.

While the high values of the determination coefficient (r higher than 0.9) for NH_3 , NO_3^- , BOD_5 , COD, SS, Cl^- , $\text{SO}_4^{=}$, Na^+ , Mg^{+2} and Oil and grease, demonstrate a good model capacity relating water values and distances downstream

Finally the paper concludes that artificial purification efforts at the water works should be directed towards controlling the concentration of Cl^- , $\text{SO}_4^{=}$, Na^+ , Ca^{+2} , Mg^{+2} which increased with increases in distance downstream and suggests further research in the area of monitoring water quality.

Key words: Self purification, Abu-Grebe Dairy factory, Tigris River, Al- Saqlawiya drain, White Gold village

التنقية الذاتية في مبزل الصقلاوية منطقة ابو غريب

الدكتور المدرس جذوة عبد الكريم ابراهيم

الخلاصة

تم جمع عينات من المياه السطحية الجارية على طول مجرى مبزل الصقلاوية ولمسافة تقدر بـ 24.5 كم . يجري المبزل ضمن اراض باستعمالات مختلفة قبل ان يصب في نهر دجلة في نهاية المطاف . تم تحديد ثمانية مواقع على طول مجرى البزل وخلال موسم الجفاف. اما ماتم تحليله من المتغيرات ذات العلاقة بتحديد نوعية المياه السطحية فقد كانت pH و NH_3 و NO_3^- و $\text{PO}_4^{=}$ و BOD_5 و COD و TDS و SS و Cl^- و $\text{SO}_4^{=}$ و Na^+ و Ca^{+2} و Mg^+ ، واخيرا وليس اخرا النفط والدهون الثقيلة. كذلك تم استخدام الطرق الوصفية والاستنتاجية من خلال اختيار افضل منحني يمثل افضل قوة ارتباط بين خصائص المتغيرات الكيميائية والفيزيائية والعضوية للمياه السطحية للمبزل والمسافة الخطية نزولا ومع جريان المبزل حتى التقائه بنهر دجلة. وبمقارنة النتائج للمتغيرات اعلاه عند نقطة التقاء مبزل الصقلاوية مع نهر دجلة تبين ان تسعة متغيرات من اصل اربعة عشر تتناقص في تركيزها مع مسافة الجريان حتى نقطة الالتقاء . كما تم اختيار موديلات رياضية باستخدام ست نقاط موقعية (0 و 1 و 3 و 5 و 7 و 8) وتوفير ثلاثة (2 و 4 و 6) ليتم استخدامها كتطبيق للموديل . تراوحت نسبة الخطأ للقراءات المحسوبة (المخمنة من الموديل الرياضي) من (0.54 الى 15) % بالنسبة لـ pH و NH_3 و BOD_5 و COD و TDS و Cl^- و $\text{SO}_4^{=}$ و Na^+ و Mg^{+2} والتي تشير الى كفاءة الموديل . بينما ارتفاع معامل الارتباط للمتغيرات NH_3 و NO_3^- و BOD_5 و COD و SS و Cl^- و $\text{SO}_4^{=}$ و Na^+ و Mg^{+2} ، والنفط والدهون يشير الى وجود علاقة وثيقة بين تغير تركيز هذه المتغيرات مع المسافة الخطية جنوبا . واخيرا فان البحث يستنتج ان توجه عمليات المعالجة الى معالجة المتغيرات Cl^- و $\text{SO}_4^{=}$ و Na^+ و Ca^{+2} و Mg حصرا والتي تزايدت مع المسافة جنوبا . كما ويقترح البحث الاستزادة في بحوث متابعة نوعية المياه في هذه المنطقة.

الكلمات الرئيسية:

التنقية الذاتية، معمل البان ابو غريب ، نهر دجلة، بزل الصقلاوية، قرية الذهب الابيض

Introduction

Self purification potential is a capability by which rivers are enabled to dilute, lessen or eliminate the undesirable effects of entered pollutants. Precise specification of such capability may be considered as a powerful instrument in rivers sustainable management (Mehrdadi and others, 2006). The self-purification capacity of many rivers has been exceeded by far, and they serve now as wastewater collectors in many cities of the world (Ramírez, 2005).

Agricultural practices in many countries still use flood irrigation and uncontrolled use of pesticides and fertilizers. This combination leads to the production of non-point source discharges that increase the river pollution. All the conditions mentioned above imply problems for large- or medium-sized rivers, but are especially critical for small rivers (Corbitt, 2007).

The so-called small-sized rivers (5 to 12 m wide), low depth (0.3 to 0.7 m) and wide river beds (8 to 20 m) have slow and



structured plug flows that result in a slow oxygen transfer from the upper layer to the middle and to the one in contact with bottom sediments (Ramírez, 2005). Nutrients from the river basin or from rain runoff are introduced into the rivers part of the natural cycle. These nutrients allow the survival of bacteria and algae that will transform the organic matter into inorganic compounds, integrating them into the trophic cycle. Rivers under the conditions stated above are called rivers in equilibrium (Ostroumov, 1999). Anthropogenic activities disturb this equilibrium by continuously discharging wastes into rivers, such as domestic and industrial raw wastewater or agricultural non-point sources, producing a decomposition zone, followed by a septic zone, a recovery zone and finally a clean zone. The length of each of these zones depends on the water flow rate, quantity and kind of bacteria (free or attached), nutrient transport and transformation, oxygen uptake and quality and quantity of anthropogenic contaminants (Fair, 1991).

Degradation of contaminants is especially slow in small sized rivers due to low-flow velocity and few free bacteria in the water column. Therefore, the different zones are longer than those in the bigger-sized rivers (Ostroumov, 1999).

Pollution sources that threaten the quality of water in Al-Saqlawiya channel may be classified into two categories namely point and non-point sources. Point pollution sources are those whose waste is discharged in to the river from a specific point. Major pollutants of this

category are Abu-Grebe Dairy factory, as well as waste water discharged from the residential area of White Gold Village.

On the other hand, non-point sources whose waste is considered as a distributed load consist of agriculture-related pollutants which are drained towards the channel.

The rapid oxygen consumption of dairy waste discharged into public water will lead to lack of oxygen, much quicker than in the case of domestic sewage (Hammer, 1975).

In Natural River systems, organic matter is assimilated by a number of processes that include sedimentation, which is enhanced by mechanical and biological flocculation, chemical oxidation and the death of enteric and pathogenic microorganisms by exposure to sunlight (Ramírez, 2005).

Biodegradable organic matter is gradually eliminated in rivers due mainly to bacterial action by methods very similar to those occurring in wastewater treatment. Complex organic molecules are broken down to simple inorganic molecules in a process requiring oxygen (Nemerow, 1984).

Wastes which are high in degradable organic matter (such as domestic sewage and dairy wastes) will rapidly use up a stream's dissolved oxygen resources in the decomposition/stabilization process.

In some instances the oxygen levels drop to a very low or zero point. Dissolved oxygen is essential to all higher forms of aquatic life. It is widely accepted that a dissolved oxygen level of 3 to 5

milligrams per liter is the minimum required to support a balanced population of aquatic flora and fauna. A lower level can be tolerated in drainage canals, where there is little or no fish life, but it must be kept above zero in order to avoid foul odors or other nuisances (Churchill, 1994).

However, since majority of the inhabitants in this area have no access to treated water, people generally lives directly on polluted streams where quality of water depended solely on the extent of natural cleansing. The drain channel under study receives highly polluted sources and empties into Tigris River. There is therefore a need to determine evidences (if any) of the processes of self purification and also identify which of the water chemistry variable are affected by the process of self purification using fourteen classical indicators pH, Ammonia (NH_3), Nitrate (NO_3^-), Phosphate (PO_4^{3-}), Biochemical Oxygen Demand (BOD_5), Chemical Oxygen Demand (COD), Total Dissolved Solids (TDS), Suspended Solids (SS), Chlorides (Cl^-) ions, Sulphate (SO_4^{2-}) ions, Sodium (Na^+) ions, Calcium (Ca^{+2}) ions, Magnesium (Mg^{+2}) ions, and Oil and Grease.

The Study Area

Al-Saqlawiya channel is a drain and storm water open channel. Verifications agree among themselves that this drain was a rivulet in a series of four rivulets used to irrigate area enclosed between Tigris and Euphrates. The four rivers used to reduce the Euphrates flooding problem flow in a north-easterly

direction to discharge into Tigris River (Sussa, 1981).

The channel flows through farmland and intermittently receives wastewater from Abu Grebe Dairy factory at the north reach of the drain. Al-Saqlawiya channel is about 24.50 km long, it flows through densely populated areas around the middle and lower reaches before draining Periodically into Tigris River (Al-Ferej, 1983), (figure 1).

The riparian population is largely poor and inadequately provided with basic sanitation or portable clean water. As a result, most riparian inhabitants and itinerant herds' men depend largely on the open channel for their daily water needs. People and livestock visit the channel regularly and undertake activities within or beside the drain, and because of people's attitude huge amount of domestic waste are generated which are not properly disposed off, but are dumped indiscriminately along streets, open spaces and on the bank of the channel. In absence of sewerage system, people are using septic tanks and soak pits. In most of the places sewage is discharged into open sub drains without any treatment, ultimately discharged to Al-Saqlawiya drain.

Average temperature is high throughout the year (about 37°C). The flow pattern exhibited by the drain is highly patterned along the incidences of rainfall. The river exhibits higher velocity and greater volume during rainy season, but almost dries up during the dry season (Al-Ansari and Al-Sinawi, 1995).

The retention time for the channel effluents in this reach is estimated about 9 hours under calm and dry weather conditions. But under heavy rainfall, whose discharge can be up to 5 times the dry weather discharge, the lower extreme of retention time is 6 hours (Al-Ferej, 1983).

Materials and Method of Study

Sampling occurred during the absence of precipitation. The period was ideal since in-channel activities are frequent in dry weather and channel velocity is very low during this period.

Thus, a reasonable duration of stream flow was guaranteed and temporary contamination generated by surface runoff and resuspension of contaminated sediments by turbulent flow was reduced.

Standard analytical procedures (APHA, 1995) were followed for Suspended Solids (SS), Biochemical Oxygen Demand (BOD₅), Chemical Oxygen Demand (COD), Sulphate, TDS, Cl⁻ and Ammonia. Direct determinations with a spectrophotometer at UV437 were made for turbidity, using 5cm quartz cuvette and the results reported as absorbance per meter (Abs. m⁻¹).

Na⁺ was analyzed using a flame analyzer while Mg⁺² and Ca⁺² were analyzed using atomic absorption spectrometer. The pH was determined by glass electrode pH meter, NO₃⁻ by colorimetric method using phenol disulphonic acid and phosphorous by bray method.

The inferential method employed which is the product moment linear correlation statistics was used to test the strength of the association between water chemical characteristics and distances downstream the drain channel, and between the parameters themselves.



Fig.1 Al-Saqlawiya Drain showing the sampling points

Methodology

The methodology involved was walking the whole length of the channel, carrying out a visual inventory, collecting samples from preselected sites as exposed in table 1. Samples were collected once a month during the dry months scooped up from below the water surface at midstream and bottled in precleaned glass flasks. Filled sample flasks were sealed free of air bubbles with glass stoppers and stored in darkness at a temperature of approximately 4°C.

Table 1: Sampling points descriptions

Station no.	Location description
0	Meeting point of Al-Saqlawiya Drain and Dairy discharge
1	0.25km downstream pt. 0
2	0.5km downstream pt.0 along Al-Saqlawiya Drain
3	1km downstream pt. 0 along Al-Saqlawiya Drain
4	3km downstream pt 0
5	7km downstream point 0
6	11km downstream pt.0
7	Al-Shaul'a pumping station (17km downstream pt.0)
8	Al-Saqlawiya Drain -Tigris River meeting pt.(24.5 km downstream pt. 0)

The samples were tested in the laboratory for the parameters mentioned above.

Results

Descriptive Characteristics Of Chemical Parameters

The results of the descriptive statistics show that the means of the chemical parameters vary from one parameter to the other (Table 2). For example, it ranges from 2494.6 mg/l for water total dissolved solids, to 0.92 mg/l for phosphates ions. On the extent of the variation between each of these chemical parameters and their mean the result of the standard deviation vary from one parameter to the other. This ranges from 1109.5 mg/l for total dissolved solids to 0.584 for pH. On the relative deviation from one sample point to the other, the result of the coefficient of variation showed that seven parameters (PO_4^{3-} , BOD_5 , COD, TDS, SO_4^{2-} , Na^+ , Mg^{+2} , having heterogeneous distribution due to high coefficient of variation that is greater than 33%. The implication of the above is that these parameters vary on the nature of their occurrences. This point to the fact that water chemistry properties along the channel is highly variable, suggesting that there is a need for close monitoring of chemical parameters for the purposes of water resource management in the study area.

Table 2: Descriptive characteristics of

Variable	pH	NH_3	NO_3^-	PO_4^{3-}	BOD_5
Mean	7.74	2.54	16.18	0.92	32.31
Standard Deviation	0.584	0.917	4.276	0.738	194.1
CV%	7.5	30.1	26.4	80.1	60.0
Variable	COD	TDS	SS	Cl^-	SO_4^{2-}
Mean	68.40	2494.6	76.37	1242.8	2249
Standard Deviation	43.30	1109.5	14.9	446.38	980.8
CV%	63.3	44.4	19.5	30.0	43.6
Variable	Na^+	Ca^{+2}	Mg^{+2}	Oil & Grease	
Mean	974.78	288.1	105.8	21.5	
Standard Deviation	392.4	113.97	82.5	17.18	
CV%	40.25	30.5	77.9	79.9	

water samples



Spatial Characteristics of Water

All the chemical parameters vary in their concentration. pH initially at the source was 10.0, it changed to 7.5 mg/l at point 7 and later to 8.1 at the mouth of the river

(Sample point 8) (Fig. 2a). The value of NH_3 increased from 2.75 mg/l at the source to 9.0 mg/l in sampling point 7, and then decreased to 0.4 mg/l at river's mouth. NO_3^- initially was 71.6 mg/l; it went down to 13.1 mg/l on sampling point 2. This later decreased to 5.5 mg/l (Fig. 2c). Phosphates decreased from 3.64 mg/l at the source to .04 mg/l but further increased to 0.43 mg/l (Fig. 2d). BOD had an initial extreme value of 1860 mg/l, yet it experienced a noticeable decrease to 7.2 mg/l at point 4 and 5, this changed to 100.0 mg/l, 15.0 mg/l and finally to 2.0 mg/l at sample point 8 (Fig. 2e). COD at the source was 147 mg/l; it went down to 99.1 mg/l in sample point 2 and to 8.86 mg/l at sample point 8. Water Total Dissolved Solids had an initial value of 3047 mg/l, increased dramatically to 5780 mg/l at sampling point 6, this increase may possibly due to irrigation flow over and finally was diluted to 712.0 mg/l at sampling point 8, (Fig. 2g). Suspended particles decreased from 290 mg/l at source to 60.50 mg/l at point 1 and finally decreased to 27.60 mg/l at the meeting point (Fig. 2h). The value of Cl^- increased from 1480.00 mg/l at the source to 2512.0 mg/l, but back off to 156.9 mg/l at the channel mouth (Fig. 2i). The value of $\text{SO}_4^{=}$ increased dramatically from 356.5 mg/l at the source to 2512 mg/l at point 1, and further more to 2675.0, 2800 and 3000 mg/l at sampling points 5, 6 and 7.

A value of 900.7 mg/l was reported in point 8 (Fig. 2j). Na^+ initially was 445 mg/l; it went up sharply to 1600 mg/l at point 1. This later decreased to 560 mg/l at sample point 8 (Fig. 2k). This increase may possibly due to riparian inputs.

Ca^{+2} had an initial value of 82.4 mg/l this increased to 416 mg/l at sample point 1 and later on diluted to 210 mg/l at sample point 8 (Fig. 2l). Mg^{+2} increased from 19.5 mg/l at the source to 61.4 mg/l as it arrives the mouth, (Fig. 2m). Finally Oil and Grease was 54.7 mg/l at the source but it kept swinging. 15.4, nil, 5 mg/l, nil, as the channel flow in Tigris River (Fig. 2n).

The high variability in concentration of water chemistry is an expected result of land use changes coupled with the impact of self purification processes, which has either increased or decreased concentration of water chemical parameters in the study area.

Al-Saqlawiya Drain Self Purification

A comparison of the chemical parameters values at the Drain-Tigris meeting (sampling point 8) shows that nine parameters (pH, NH_3 , NO_3^- , $\text{PO}_4^{=}$, BOD_5 , COD, TDS, S.S, and Oil and Grease) out of the 14 parameters decreased in their concentration. This might be due to processes such as oxidation, sedimentation, and volatilization (Oldaker, 1999).

Hence, water parameters are likely to be present in lower concentration in the drain-river joining point, while other parameters must have added into their concentration probably from riparian inputs or plants senescence along the river channel. This consequently suggests a need to examine the concentration of these other

parameters in some details for the purpose of environmental management.

In a further analysis, predictive models were obtained through using six sampling points (0, 1, 3, 5, 7, 8) and leaving three (2, 4, 6) as activation function. Table 3, expose the performance of different models estimated for the six points only, while table 4 shows the calculated value corresponding the actual value and the mean percentage error by applying the spared three points (2, 4 and 6).

The percentage error for the calculated values of pH, NH₃, BOD₅, COD, TDS, Cl, SO₄, Na, Mg⁺² ranges from (0.54 to 15)% which demonstrate the high predictive capacity of the models.

The high values of the determination coefficient (r higher than 0.9) for NH₃, NO₃, BOD₅, COD, SS, Cl, SO₄, Na, Ca, Mg. and Oil and grease, demonstrate a good model capacity relating water values and distances downstream as concentration tends to decrease from the point source downstream as time elapses. However there are other water parameters where the concentration increases downstream, for it must be noted that the conservative pollutant show higher concentration than the non-conservative pollutant. This is because the mass of the former is conserved while the latter decays via various factors such as oxygenation.

One can therefore conclude that artificial purification efforts at the water works should be directed towards controlling the concentration of the increased parameters concentration downstream just mentioned.

The paper suggests further research in the area of monitoring water quality of the parameters. This will be more important at a future date, when the pollutant loadings

in the water body might have increased particularly due to anthropogenic influence in the study area.

River Potability

A comparison of the values of water chemistry at the rivers mouth with the Iraqi Standards, 417/2001 for drinking water and “system of Preservation of Water Sources no. 2 dated 2001” (table 5) shows that five out of the fourteen parameters (Cl⁻, SO₄⁼, Na⁺, Ca⁺² and Mg⁺²) exceeded the Iraqi Standards. Also, these five parameters have been found to increase with distances downstream. Other water parameters fell short of the required limits. Excess concentration of Cl⁻, SO₄⁼, Na⁺, Ca⁺² and Mg⁺² may probably due to riparian inputs from the surrounding farmlands, this has been noted to aggravate hypertension in adults and also to elevate blood pressures in children (WHO, 2006). The high COD can be indicative of the extent of chemical pollution from the riparian land use, in form of leachate from chemical fertilizers and forms of herbicides from farmlands. Both phosphate and nitrogen cause eutrophication in surface water bodies. It is apparent that the nitrogen values were increased after each sewerage scheme.

**Table 3:** Space/time model, for five in between sampling points.

Parameter	Model fit
pH r=0.848	Exponential Association: $y=a(1-e^{-bx})$ a =7.409E+000 b = 1.587E-002,
NH ₃ r=0.958	Exponential association: , a=1.087 b=0.149 e^{-bx} y=a(1-
NO ₃ r=0.989	$\frac{1}{a+bx^c}$ Harris Model : y= a =-6.945E-001,b =5.272E-001 c =6.419E-002
PO ₄ ⁻³ r=0.882	Harris Model : y= $\frac{1}{a+bx^c}$ a =6.193E+000, b =-6.00E-002 c =1.991E+000,
BOD ₅ r=0.999	Harris Model: y= $\frac{1}{a+bx^c}$, a =5.376E-004, b =9.431E-005 c =8.548E-001
COD, r=0.959	Harris Model y= $\frac{1}{a+bx^c}$ a =-4.121E-001, b =4.094E-001 c =5.055E-003
TDS r=0.861	Quadratic Fit: y=a+bx+cx ² a =5.622E+002, b =7.462E-001 c =-2.992E-005
S.S r=0.993	$\frac{1}{a+bx^c}$ Harris Model: y= a =-1.991E-001, b =1.592E-001 c =5.229E-002,
Cl ⁻ r=0.974	MMF Model: =(ab+cx ^d)/(b+x ^d) a =-5.686E+000,b =2.067E+007 c =1.891E+003,d =3.267E+000
SO ₄ ⁼ r=0.993	MMF Model: y=(ab+cx ^d)/(b+x ^d) a =-8.485E+000, b =5.249E+007 c =2.577E+003,d =3.552E+000
Na ⁺ r= 0.996	MMF Model: y=(ab+cx ^d)/(b+x ^d) a =5.658E-001, b =4.315E+003 c =1.390E+003, d =1.652E+000
Ca ⁺² r=0.997	MMF Model: =(ab+cx ^d)/(b+x ^d) a =-4.682E-001, b =1.206E+005 c =3.267E+002, d =2.311E+000
Mg ⁺² r= 0.985	Gunary Model =x/(a+b ^x +c ^{sqr(x)}) a =-2.989E+000, b =9.849E-003 c =2.341E-001,
Oil and Grease r= 0.998	Harris Model: y=1/(a+bx ^c) a =-2.594E+000. b = 1.202E+000 c =1.682E-001,

Table 4: calculated value, actual value and the mean percentage error for the spared three points (2, 4 and 6).

Parameter	Calculated (actual)	Error%
pH	7.40,7.41, 7.41 (7.15),(7.34), (7.46)	0.54%
NH ₃	1.26, 0.188, 5.172 (0.75, 0.55, 4.77)	9.39%
NO ₃	10.973, 5.35, 3.793 (9.54, 9.81, 8.65)	-39.2%
PO ₄ ⁻³	1.75, 0.129, .021 (0.07, 0.51, 0.43)	46.8%
BOD5	77.5, 11.22, 3.71 (15, 44, 22.8)	11.5%
COD	107.3, 70.15, 58.59 (99, 67.8, 33.8)	15%
TDS	927.83, 2531.51, 5150.24 (456, 1500, 5780)	10.14%
S.S	47.06, 23.31, 16.69 (86.5, 52.4, 31)	94.5%
Cl-	1834.14, 1891.95, 1891.95 (1480, 1983, 1842)	10.9%
SO=4	2543.49, 2577.98, 2566.46 (2512.1, 2637.7, 2325.3)	2.92%
Na+	1209.64, 1380.3, 1389.74 (1668, 1000.6, 945.9)	9.22%
Ca+2	307.13, 327.81, 328.1 (566, 470, 448)	55.3%
Mg+2	69.72, 76.16, 84.66 (71.2, 70.2, 71.2)	7%
Oil and Grease	1.2, 0.49, 0.31 (0, 0, 5)	150.50%

Table 5: Drinking water standard and Preservation of Water Sources System no. 2 dated

Parameters	Values at Drain-River meeting, point (8)	Iraqi Drinking water Standards 417/2001 Max.	Water quality limits to be assured in the water bodies according to the Iraqi legislation "Preservation of Water Sources System no.2 dated 2001, (B-1)
pH	8.1	8.5 unit	6.5-8.5
NH ₃	0.4	-----	-----
NO ₃ ⁻	5.5	50	-----
PO ₄ ⁼	0.43	-----	-----
BOD ₅	2	-----	40
COD	8.6	-----	100
TDS	712	-----	-----
S.S	27.6	nil	-----
Cl ⁻	1000	250	-----
SO ₄ ⁼	900.7	500	-----
Na ⁺	560	200	-----
Ca ⁺²	210	50	-----
Mg ⁺²	61.4	50	-----
Oil and Grease	nil	-----	10

Conclusions

The study showed that water chemical parameters vary in both relative and absolute terms. This is clearly shown by the descriptive statistics.

The process of self- purification can be said to operate in the study area since most of the chemical parameters examined reduction in their concentration at the drain-river meeting (sample point 8) compared to their initial concentration.

A decrease in concentration was noticed for the parameters pH, NH₃, NO₃⁻, PO₄⁼, BOD₅, COD, TDS, S.S, and Oil and Grease. While other parameters, of Cl⁻, SO₄⁼, Na⁺, Ca⁺² and Mg⁺ appeared to have gained more materials downstream probably, from the riparian land use comprising mainly farmlands. Hence, purification efforts along the channel should be directed to the control of these parameters.

On the state of stream water Potability, a comparison with local standards of drinking water and preservation of surface water system showed that only five parameters (Cl⁻, SO₄⁼, Na⁺, Ca⁺² and Mg⁺) exceeded the maximum permissible limit of the national standards. Therefore, water treatment effort should be directed towards examining and reduction of the concentration of the above mentioned parameters.

The comparison between the response of the model to the environmental variables on one hand, and results from field observations on the other the hand, shows similarities and indicates that the current modeling can be trusted. The result can be considered satisfactory since the model built up from set of data obtained in the same geographic area.

**Acronym and abbreviations**

BOD₅: Biological Oxygen Demand
Ca⁺²: Calcium ions
Cl⁻: Chloride ions
COD: Chemical Oxygen Demand
Mg⁺²: Magnesium ions
Na⁺: Sodium ions
NH₃: Ammonia
NO₃⁻: Nitrate ions
pH: Acidity measurement
PO₄⁼: Phosphate ions

r: Correlation value
S.S : Suspended Solids
SO₄⁼: Sulphate ions
TDS: Total Dissolved Oxygen

References

Al-Ansari and Al-Sinawi, 1995 ((Water quality of Tigris River water at Baghdad using multi variant analysis)), Proceeding of Iraqi conference in engineering, ICE.

Al-Ferej, Ahmed Furat, 1983, "The Characteristics of some Iraqi Irrigation Systems and their Balancing Systems" A Thesis Submitted to the Department of Irrigation and Draining Engineering of the University of Baghdad for the Degree of M.s.c. in Irrigation and Draining Engineering.

APHA, 1995 ;Standard Methods for the Examination of Water and Wastewater, American Public Health Association, Washington, D.C.

Benoit R.J. 1981, "Self purification in Natural Waters". In. Water and Water Pollution Handbook. Volume 1. New York, p. 63.

Churchill, M. A., Elmore, H. L., and Buckingham, R. A., 1994 "The Prediction of Stream Reaeration Rates," Advanced Water Pollution Research Proceedings, 2nd International Conference, Vol. 2, Tokyo, Japan, Pergammon Press, New York, N.Y.

Fair, G. M., Moore, E. W., and Thomas, H. A., Jr., 1991 "Natural Purification of River Mud and Pollutational Sediments," Sewer Works Journal, Vol. 9, No. 1.

Mehrdadi, M. Ghobadi, T. Nasrabadi, H. Hoveidi, 2006, "Evaluation of the Quality and Self Purification Potential of Tajan River Using Qual2e Model". Iran. J. Environ. Health. Sci. Eng., Vol. 3, No. 3, pp. 199-204

Nemerow Nelson N., 1984 "Scientific Stream Pollution Analysis "McGraw-Hill. Oldaker Warren H., 1999, (Deposition in a River and Their Potential Effects on D.O. Concentration" Journal of The

Sanitary Engineering Division, ASCE,
Vol. 84, No. SA5.

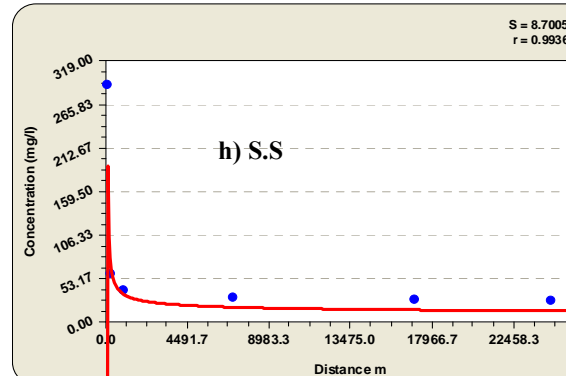
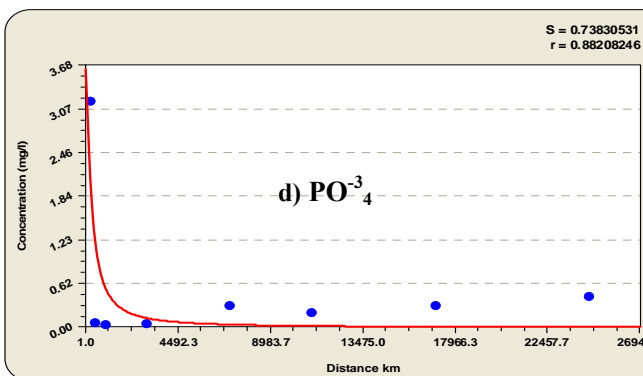
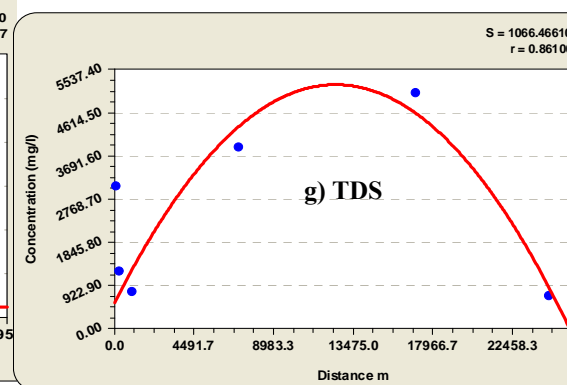
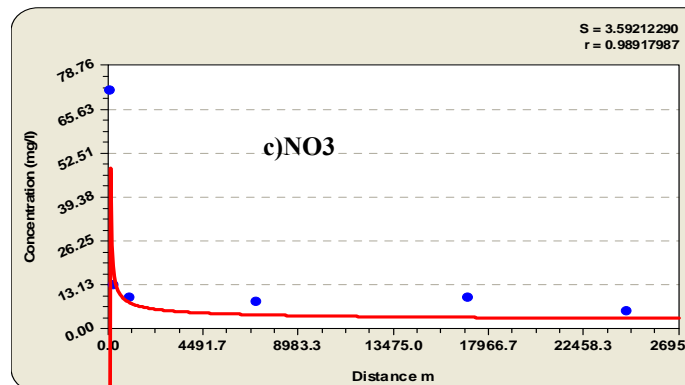
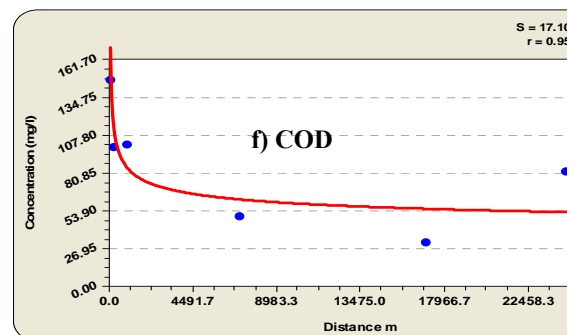
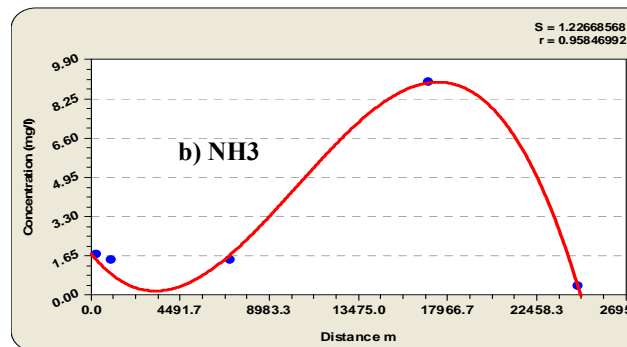
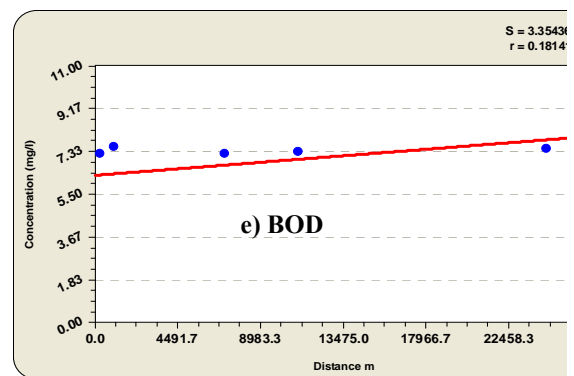
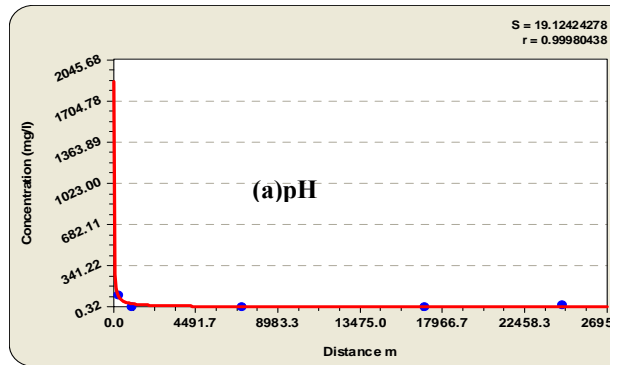
Ostroumovsa (1999) "Water self
purification and nature bioremediation in
the biosphere: New concepts and new
experimental data. J. Biospheric Sci. 1 9-
23.

Ramírez-Bacal, R Saucedo-Terán, LI
Manzanares Papayanopoulos, 2005
"Treatment for Small Polluted Rivers:
Design and Performance of an
Experimental Structure" Water SA Vol.
31 No. 1.

Sussa, Ahmed 1965 "Baghdad Flooding in
History", pp. 387-400.

Hammer, M. J., 1975. "Water and
Wastewater Technology", John Wiley and
Sons, NY.

WHO (2006). Guidelines for Drinking-
Water Quality: First Addendum to 3rd,
Edition. Vol. 1, Recommendations.
Geneva, World Health Organization: 595
pages.



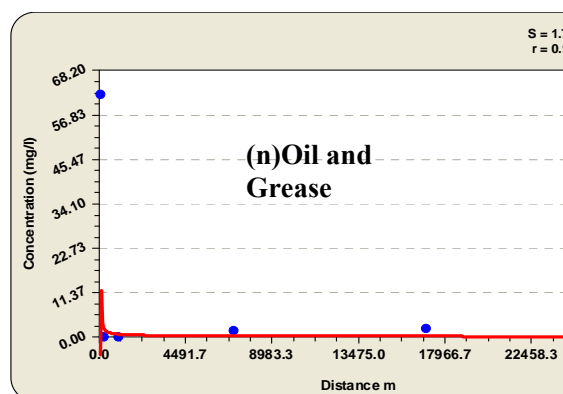
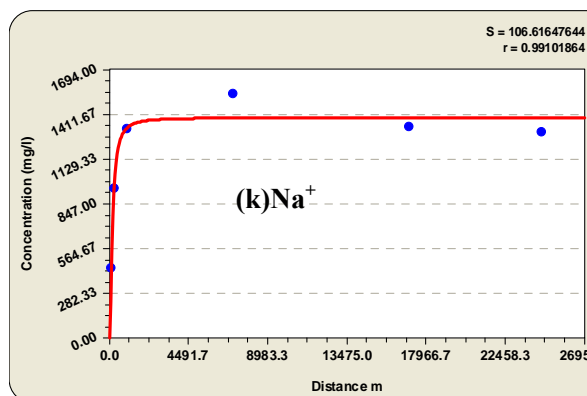
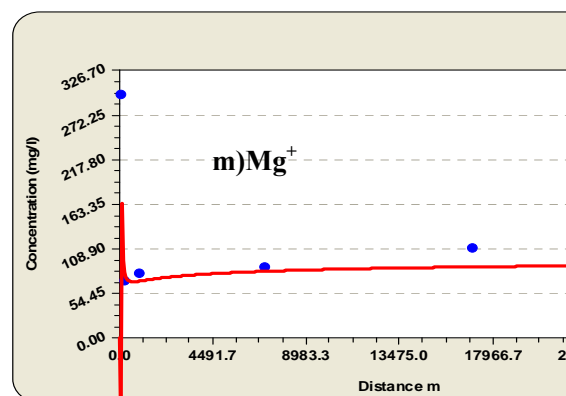
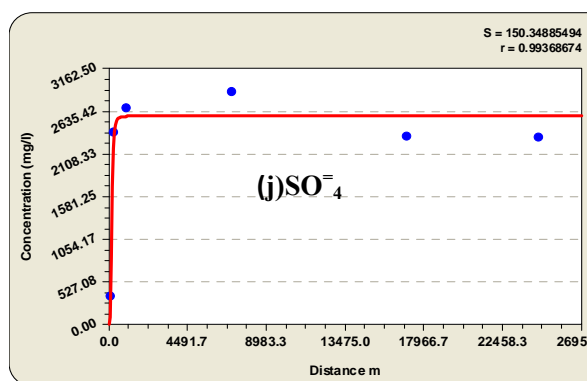
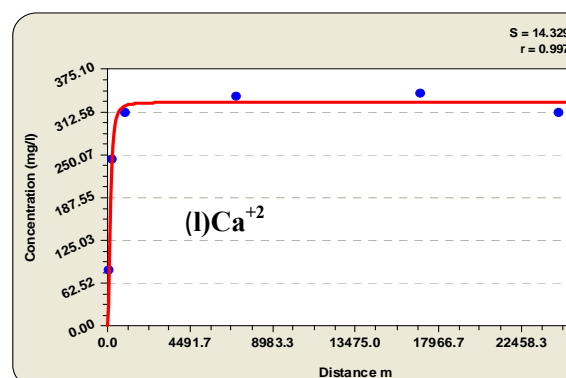
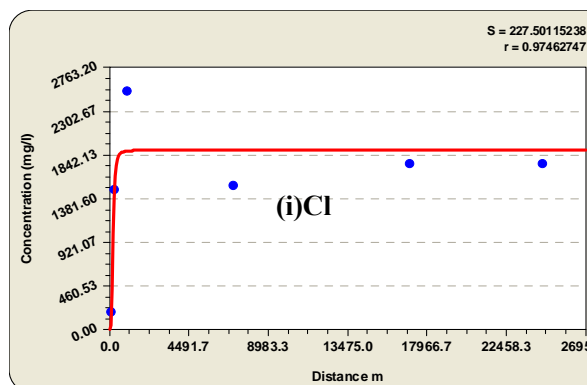


Fig 2: (A-N) Graphical Representation of the Self – Purification Mechanisms in Al- Saqlawiya Drain



Removal of 4-Chlorophenols from Simulated Wastewater by Advanced Oxidation Processes

Yasmen Abdul Mustafa
Environmental Engineering Dept.
Collage of Engineering, University of Baghdad

Ahmed Hameed Shihab
Water Resources Engineering Dept.
Collage of Engineering, University of Baghdad

yasmen.mustafa@gmail.com

engineer.ahmed81@yahoo.com

Abstract

The degradation and mineralization of 4-chlorophenol (4-CP) by advanced oxidation processes (AOPs) was investigated in this work, using both of UV/H₂O₂ and photo-Fenton UV/H₂O₂/Fe⁺³ systems. The reaction was influenced by the input concentration of H₂O₂, the amount of the iron catalyst, the type of iron salt, the pH and the concentration of 4-CP.

A colored solution of benzoquinon can be observed through the first 5 minutes of irradiation time for UV/H₂O₂ system when low concentration (0.01mol/L) of H₂O₂ was used. The colored solution of benzoquinon could also be observed through the first 5 minutes for the UV/H₂O₂/Fe⁺³ system at high concentration (100ppm) of 4-CP. The results have shown that adding Fe⁺³ to the UV/H₂O₂ system enhanced the rate of 4-CP oxidation at a molar ratio of H₂O₂/Fe⁺³/4-CP equals to 13/0.4/1 by a factor of 7. This reduced the consumption of H₂O₂ by a factor of 6 and the irradiation time required for complete degradation was reduced by a factor of 6. The experimental results have shown that the optimum reagents for a complete degradation of 4-CP(50ppm) were H₂O₂=0.005mol/L, Fe⁺³=0.16*10⁻³ mol/L under acidic condition (pH=3) and irradiation time of 15 min for the UV/H₂O₂/Fe⁺³ system with a molar ratio of H₂O₂/Fe⁺³/4-CP equals to 13/0.4/1.

Keywords: 4-chlorophenol; advance oxidation process; Fenton process; photo-Fenton process; UV photolysis.

الخلاصة

تم التحقق من فاعلية استخدام طرق الأكسدة الحديثة (AOPs) للنظامين UV/H₂O₂ و UV/H₂O₂/Fe⁺³ لأكسدة وتحلل مادة الكلوروفينول (4-CP). التفاعل تأثر باختلاف الكميات المضافة من بيروكسيد الهيدروجين (H₂O₂)، كمية الحديد كعامل مساعد، نوعية العامل المساعد Fe⁺³ و Fe⁺²، pH و تراكيز المحلول للكلوروفينول. المواد الملونة متمثلة بال (benzoquinone) تم ملاحظتها بعد 5 دقائق من بدأ التجربة لنظام UV/H₂O₂ عند استعمال تركيز قليل لبيروكسيد الهيدروجين (0.01 mol/L). كذلك تم ملاحظة ظهور المواد الملونة بعد 5 دقائق من بدأ التجربة لنظام UV/H₂O₂/Fe⁺³ عند استعمال تراكيز عالية من الكلوروفينول (100ppm). النتائج بينت ان إضافة الحديد (Fe⁺³) كعامل مساعد الى نظام UV/H₂O₂ وبنسبة مولارية 13/0.4/1 ل H₂O₂/Fe⁺³/4-CP أعطت تحلل أعلى بمقدار 7 مرات وأدت إلى تقليل مادة H₂O₂ المضافة بمقدار 6 مرات وان الزمن اللازم للوصول الى التحلل الكامل انخفض بمقدار 6 مرات. التراكيز المثلى اللازمة للحصول على تحلل كامل للكلوروفينول بتركيز 50 ppm هي H₂O₂=0.005mol/L ، Fe⁺³=0.16*10⁻³mol/L عند وسط حامضي pH = 3 وبزمن 15 دقيقة للنظام UV/H₂O₂/Fe⁺³ وبنسبة مولارية 13/0.4/1.

1. Introduction

The need to restore contaminated sites to avoid further damage to the environment has raised the development of effective methods for pollutants removal in the last years. The treatment processes for different types of effluents must guarantee the elimination or recuperation of the pollutants in order to reach the strict authorized levels for their discharge, (Weber and Smith, 1986).

An ideal waste treatment process must completely mineralize the toxic species present in the waste streams without leaving behind any hazardous residues and should be cost-effective as well, (Stoyanova et al., 2003).

Chlorophenols are highly toxic and cause considerable damage to the ecosystem and human health. They are notified as potential toxic compounds by United State Environmental Protection Agency (USEPA) and their maximum allowable concentrations in drinking-water as total chlorophenols are 0.1ppb (WHO, 2008).

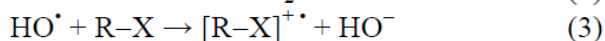
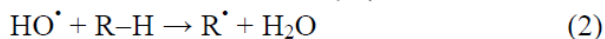
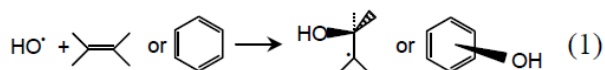
They are introduced into the environment as a result of several man-made activities, e.g. water disinfection, waste incineration, uncontrolled used of pesticides and herbicides, as well as by-products in bleaching of paper pulp with chlorine (Pera-Titus et al., 2004).

Chlorophenols are designated as the priority pollutants by the USEPA and European Commission (Kralik et al., 2009). All chlorophenols possess bactericidal activities that increase with the degree of chlorination. Chlorophenols are highly toxic to algae. Most plants are very sensitive to the phytotoxicity of chlorophenols. As for aquatic organisms, fish and other aquatic organisms absorb chlorophenols through their gills, gastrointestinal tract or skin (WHO, 1998).

The conventional pollutant destructive technologies include biological, thermal and physiochemical treatments. On most occasions, biological treatments require long residence time for microorganisms to degrade the pollutant because they are affected by the pollutant toxicity. Thermal treatments present considerable emission of other hazardous compounds. Other techniques such as flocculation, precipitation, adsorption, air stripping or reverse osmosis (RO) require post-treatment to remove the pollutant from the newly

contaminated environment. Alternative methods to these well-established techniques are the so-called advanced oxidation processes. AOPs are based on the initial formation of radicals, i.e., hydroxyl radicals ($\text{OH}\cdot$) that later act as non-selective oxidation agents.

The possible reaction pathways involving the attack of hydroxyl radicals onto organic compounds are: the electrophilic addition of a hydroxyl radical to organic compounds (unsaturated or aromatic) leading to the formation of organic radicals (Equation 1), the hydrogen abstraction by reacting the hydroxyl radical with a saturated aliphatic compound (Equation 2) and electron transfer with reduction of the hydroxyl radical into a hydroxyl anion by an organic substrate (Equation 3), (Tang, 2004).



Several technologies are included in the AOPs like Fenton, photo-Fenton, wet oxidation, ozonation, photo catalysis...etc. and the main difference between them is the manner to form the radicals. Even though these techniques can provide the conversion of contaminants to less harmful compounds, on most occasions, oxygenated organic products and low molecular weight acids are formed throughout the process. In addition, advanced oxidation processes are limited to treat waters which contain low concentrations of organic or inorganic scavenging substances. Experiences with different oxidation technologies and substrates have shown that partial oxidation of toxic water may increase its biodegradability up to high levels (Pera-Titus et al., 2004).

Advanced oxidation technologies (AOPs) have received increased interest (Kralik et al., 2009). Alnaizy et al., (2000) studied phenol degradation with a $\text{UV}/\text{H}_2\text{O}_2$ process in a completely mixed, batch photolytic reactor, the UV irradiation source was a low-pressure mercury lamp. The study indicates that there is an optimum H_2O_2 /phenol molar ratio for efficient degradation in the range of 100-250.



Hirvonen et al., (2000) made a comparison between 2, 4-dichlorophenol degradation rate by UV/H₂O₂ process and direct UV (20-W 254 nm lamp) irradiation, in the study they reported that the addition of hydrogen peroxide at acidic pH increased the reaction rate by one order of magnitude.

Munter (2001) used AOP to oxidize inorganic contaminants such as cyanide, sulphide and nitrite.

Carneiro et al., (2006) show that typical Fenton catalyst/H₂O₂ ratios range is 1:5 to 1:25; they proven that the optimal pH range for Fenton process is between 2.8 and 3.0.

Matilainen and Sillanp (2010) noted that the degradation of target compounds with UV/ H₂O₂ and VUV ($\lambda=172\text{nm}$) occur about eight times more effectively than with direct UV-photolysis.

Kuo and Wu, (2010) investigate the effect of solar irradiation on Fenton degradation of 4-chlorophenol. The results indicated that solar assisted photo-Fenton process was effective for complete removal of 4-chlorophenol in water. More than 90% of 4-chlorophenol was mineralized to CO₂ in solar assisted process while only 25% carbon mineralization was observed in Fenton process.

Bogatu et al., (2005); Nogueira et al., (2008); Murcia et al. 2009; and Elghniji et al., (2011) identified the intermediate generated during the photocatalytic process of phenolic compounds. The major intermediates are benzoquinone and hydroquinone. The concentrations reach a maximum and then tend to decrease gradually for longer irradiation time indicating the mineralization of these compounds.

The objective of this work is to study the effectiveness of the AOPs in the degradation of 4-chlorophenol as one of the main compounds of the chlorophenols, using pilot plant scale. The AOPs selected to carry out this study were, UV/H₂O₂ and photo-Fenton (UV /H₂O₂/Fe⁺³) systems. To achieve the experimental objectives, different variables were chosen to be followed throughout the treatment: 4-chlorophenol concentration, pH, H₂O₂ and Fe⁺³ concentrations.

2. Materials and Methods

2.1. Reagents

4-Chlorophenol (4-CP) was used as a model substance employed in this research. The physical, chemical, UV-visible absorption spectra and molecular structure of 4-CP are shown in Table 1 and Fig.1, (Thomas and Burgess, 2007). Table 2 shows all the chemicals that were used in the experimentation. All were analytical grade and used as received. All the solutions were prepared by dissolving requisite quantity in distilled water. The pH of the solution was adjusted using H₂SO₄ solution. Initial pH of solution was monitored using a pH meter from (WTW Co., Germany, INOLAB 720).

2.2. Equipments

A laboratory scale set up of AOPs system applied in this study is presented in Fig. 2, (Shihab, 2011). The reactor (1) was made entirely of aluminum with an effective volume of 37.5L. A feed tank (5) of 24L volume was used to prepare the solutions. The solution was circulated at flow rate of 3L/min by using a water pump (3) of 0.5Hp and 0.37kw (Marquis Co., China). To measure the flow rate, a calibrated flow meter (4) of Hidrotek type with flow range (3 to 20L/min) was used. This flow meter was installed vertically and the flow direction was upward. Valves were utilized for sampling, washing, drain and control in the AOPs system as illustrated in Fig.2. A photograph of the photo reactor is shown in Fig. 3. The inlet and outlet pipes were 1.8cm diameter. Vertical baffles were fixed after the inlet zone to let the water overflow to increase the mixing. Two vertical plates with ten rectangular openings (13x1cm) were used as distributors. Three removable side baffles were fixed vertically at the reactor side walls. These baffles are with square cross sectional area with a side length of 5 cm. These baffles reduce the presence of low radiation zones near the reactor walls. UV radiation was generated from three UV lamps TUV 11W 4P-SE (4-Pin single ended), these lamps emit output power at a wavelength of 253.7nm and each was sheathed in a quartz sleeve for protection. These lamps were fixed in a staggered form in the reactor. The spacing between two adjacent lamps should be in a range between (5-12) cm. If this distance is less than 5cm then the

UV energy will be absorbed by the adjacent UV lamp, if the spacing is more than 12cm, there will be a formation of a zone with low UV intensity between the lamps (Chiu et al., 1999; Lyn and Blatchley, 2005). In this study 10cm spacing was used.

Table 1: 4-CP properties (Thomas and Burgess, 2007)

General	
Name	4-Chlorophenol
CAS No.	106-48-9
Formula	C ₆ H ₅ ClO
Molecular weight	128.57 g
Solubility (H ₂ O)	27 g/L (20°C)
pKa	9.4 (25°C)
Refractive index	1.55
Spectra acquisition	
Solvent	H ₂ O
Concentrations	20.0 mg/L (pH = 1.5) and 19.5 mg/L (pH = 12.2)
Pathlength	10 mm
Reference product	FLUKA
Purity	GC > 99%

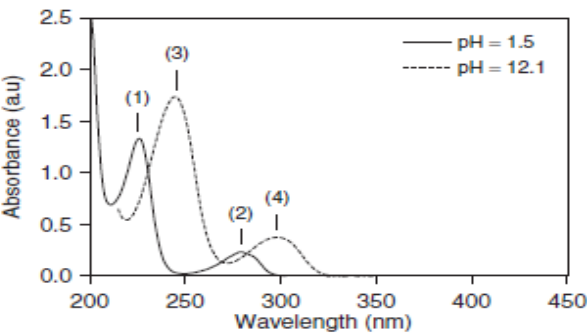
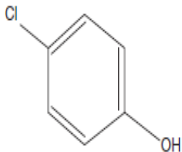


Fig.1:UV-visible spectra for the 4-CP at different pH values(Thomas and Burgess, 2007).

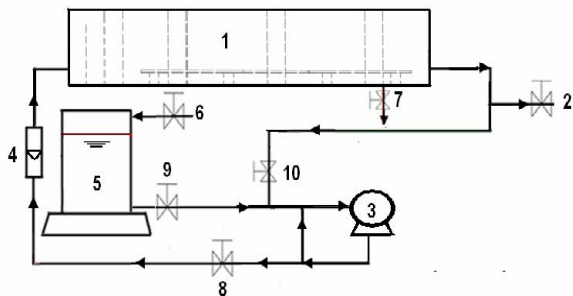


Fig.2:A laboratory scale set up of AOPs system.(1)AOPs reactor,(2)sample extraction valve (3) water pump (4)flow meter (5)feed tank (waste water) (6)washing water inlet valve,(7)drain valve, and (8,9 and 10)control valves.



Fig.3: A photograph of the AOPs reactor.

Table 2: List of chemicals used

Compound	Formula	Vendor
Hydrogen peroxide	H ₂ O ₂	Scharlau (50 % wt/wt)
Ferrous sulphate heptahydrate	FeSO ₄ ·7H ₂ O	Thomas Baker (98 % purity)
Ferric sulphate heptahydrate	Fe ₂ (SO ₄) ₃ ·7H ₂ O	Thomas Baker (99.5 % purity)
Sulfuric acid	H ₂ SO ₄	BDH (97 % purity)
Sodium thiosulfate pentahydrate	Na ₂ S ₂ O ₃ ·5H ₂ O	Riedel Seelze Hannover (99 % purity)

2.3. Experimental Procedure

The experimental procedure used in this research was as follows:

-The desired concentration of 4-CP was prepared and the pH was adjusted by adding a dilute H₂SO₄ solution in the feed tank.

- well mixing was maintained by using a mechanical stirrer for 5min.

-Initial sample (sample at time zero) was taken for analysis.



-The pump was switched on and the solution was allowed to flow from the feed tank through the pump to the photoreactor. Valves No. 2, 7 and 6 were closed and all the other valves were opened.

-The head in the photoreactor was maintained at 15cm by controlling the flow through valve No. 8.

-The desired quantity of H_2O_2 (0.01-0.05) mol/L was added to the feed tank. Circulation was allowed for few minutes then valve No.9 was closed.

-The UV light source was switched on.

-Samples were taken every 15 minutes through valve No.2 until the end of run. Samples were stored in 10 ml vials before analysis. One drop of $\text{Na}_2\text{S}_2\text{O}_3 \cdot 5\text{H}_2\text{O}$ (0.1N) was added to each sample to decompose any residual hydrogen peroxide and prevent hydrogen peroxide from reacting with 4-CP during the analysis.

-For $\text{UV}/\text{H}_2\text{O}_2/\text{Fe}^{+3}$ system, the same procedure was followed and the desired quantity of ferric sulphate was added in the feed tank before adding H_2O_2 .

-The system was cleaned after the end of each run as follows:

The UV light source was turn off, the valves No.7 and 9 were opened leaving valves No.2,10 and 6 closed to drain the reactor and feeding tank. The system was washing by a tap water through valve No.6, by maintaining valve No.10 and 2 closed and valve No.7 opened for drainage.

UV-visible spectrophotometer (Model SP-3000 plus, Optima Co., 2003, Japan) was used to analyze the samples.

3. Results and Discussion

3.1. $\text{UV}/\text{H}_2\text{O}_2$ System

The combination of UV radiation and a little amount of H_2O_2 enhanced strongly the efficiency of degradation of 4-CP. Experiments were carried out at different doses of H_2O_2 (0.01-0.05) mol/L to study its effect on the degradation and mineralization of 4-CP. Fixed 4-CP concentration at 0.39×10^{-3} mol/L (50ppm) was maintained during the experiments.

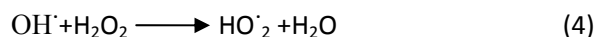
3.1.1. Effect of initial H_2O_2 concentration on $\text{UV}/\text{H}_2\text{O}_2$ system

Different concentrations of H_2O_2 (0.02, 0.03, 0.04 and 0.05) mol/L were used to show the percent degradation of 4-CP as a function of the irradiation time. The results are plotted in Fig.4. From this figure, it can be noticed that the degradation rate of 4-CP increased as the concentration of H_2O_2 increased from 0.02 to 0.03mol/L, and achieve 100% degradation at 0.03mol/L after 90 min of irradiation time. Then the degradation decreased as the H_2O_2 increased to 0.04 and 0.05 mol/L.

Fig.5 shows the degradation of 4-CP at different concentrations of H_2O_2 at irradiation time of 90 minutes. The percent of degradation increased to 100% at 0.03 mol/L of H_2O_2 then decreased to 45% at 0.05mol/L of H_2O_2 .

Investigators gave more than one explanation for these phenomena, among them:

-Hydroxyl radicals generated from the direct photolysis of hydrogen peroxide were the main responsible species of 4-CP elimination. It was expected that increasing the concentration of H_2O_2 reduces the rate of degradation of 4-CP, due to the reaction of hydrogen peroxide with these radicals, and hence acts as an inhibiting agent of 4-CP degradation (i.e. self-scavenging of OH^\cdot by H_2O_2)



-Hydroxyl radical may recombine and participate in radical-radical reactions to form H_2O_2



-At higher H_2O_2 concentrations there is lower light intensity available for 4-CP degradation, since H_2O_2 also absorb light in the system. This can possibly be attributed to low degradation of 4-CP.

-Hydroxyl radical efficiently reacts with H_2O_2 and produces HO_2^\cdot (equation 4). Since HO_2^\cdot radicals are not as reactive as OH^\cdot , and then low degradation may be obtained. H_2O_2 is OH^\cdot scavenger and so an excess H_2O_2 can result in a net decrease in the treatment efficiency (Kutschera et al., 2009).

However, if H_2O_2 dose is low, OH^\cdot formation will also be low, decreasing the treatment efficiency.

Therefore, a balance must be maintained between excess and low levels of H_2O_2 .

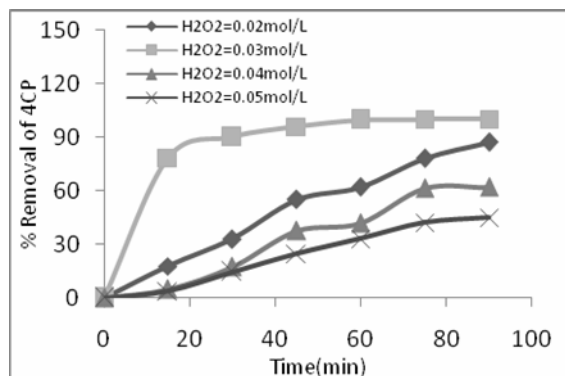


Fig. 4: Degradation of 4-CP by UV/ H_2O_2 system, 4-CP= 0.39×10^{-3} mol/L, pH=3. The effect of initial H_2O_2 concentration.

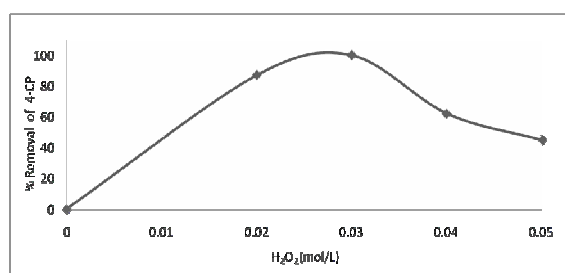


Fig.5: Degradation of 4-CP as a function of H_2O_2 initial concentration by UV/ H_2O_2 system, 4-CP= 0.39×10^{-3} mol/L, pH=3, irradiation time 90 min.

3.1.2. Reaction rate constant for UV/ H_2O_2 system

The experimental data obtained for 4-CP degradation can be fitted according to a pseudo-first-order reaction as follows:

$$-\frac{dc}{dt} = KC \quad (6)$$

The integration leads to

$$\ln C/C_0 = -K \cdot t \quad (7)$$

where C_0 and C are the concentration of 4-CP at irradiation times 0 and t , K is a pseudo-first-order rate constant (in min^{-1}) and t is the irradiation

time (in min). The regression analysis of the concentration curves versus reaction time indicates that the decomposition rate of this compound could be described by first order kinetics, Fig.6. A high increase in K was observed for 0.03 mol/L H_2O_2 (0.086 min^{-1}) compared with other concentrations, Fig. 7.

3.2 UV/ H_2O_2 / Fe^{+3} (photo-Fenton) systems

3.2.1. The effect of initial H_2O_2 concentration on UV/ H_2O_2 / Fe^{+3} system

In the photo-Fenton system both Fe^{+3} ($\text{Fe}_2(\text{SO}_4)_3 \cdot 7\text{H}_2\text{O}$) and H_2O_2 were used to attain the desirable degradation. First Fe^{+3} is fixed at constant concentration while H_2O_2 changed until high degradation was obtained.

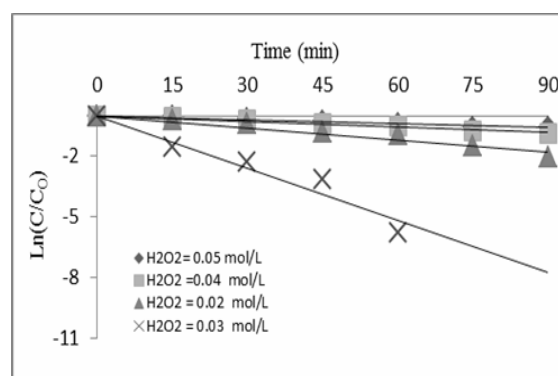


Fig.6: Pseudo-first-order rate constant for 4-CP degradation by UV/ H_2O_2 system, 4-CP= 0.39×10^{-3} mol/L, pH=3.

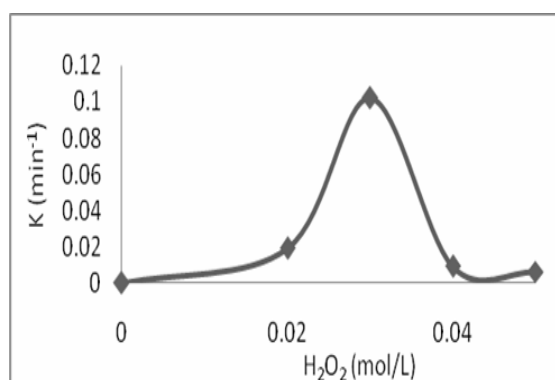


Fig.7: Pseudo-first-order rate constant for 4-CP degradation as a function of H_2O_2 initial concentration by UV/ H_2O_2 system, 4-CP = 0.39×10^{-3} mol/L, pH=3, irradiation time 90 min.



In this sense, a series of experiments were carried out in order to determine the optimum ratio of $\text{H}_2\text{O}_2/4\text{-CP}$. Different concentrations of H_2O_2 (0.003, 0.004, 0.005, 0.006 and 0.007 mol/L) were used in the presence of fixed Fe^{+3} concentration 0.078×10^{-3} mol/L. $\text{H}_2\text{O}_2/4\text{-CP}$ ratios for these concentrations were 8, 10, 13, 15 and 18 respectively, while the ratio of $\text{Fe}^{+3}/4\text{-CP}$ was 0.2. The results are plotted in Figs. 8 and 9. From these figures it can be noticed that a significant enhancement of degradation efficiency was observed when the H_2O_2 concentration was increased to 0.005 mol/L. (i.e. the ratio of $\text{H}_2\text{O}_2/4\text{-CP}$ = 13). Above this concentration, the oxidation rate seems to be negatively affected by the increase of H_2O_2 up to 0.007 mol/L (i.e. the molar ratio of $\text{H}_2\text{O}_2/4\text{-CP}$ = 18). This is due to both the auto-decomposition of H_2O_2 into oxygen and water, and the scavenging effect of hydroxyl radicals by H_2O_2 . Excess of H_2O_2 will react with HO^\bullet competing with organic pollutants and consequently reducing the efficiency of the treatment.

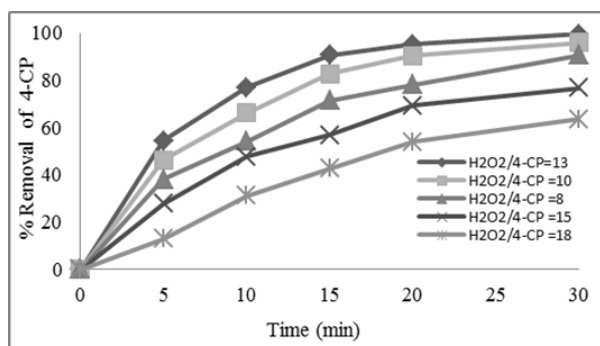


Fig.8: Degradation of 4-CP by UV/ $\text{H}_2\text{O}_2/\text{Fe}^{+3}$ system, $\text{Fe}^{+3} = 0.078 \times 10^{-3}$ mol/L, 4-CP = 0.39×10^{-3} mol/L ($\text{Fe}^{+3}/4\text{-CP}=0.2$), pH=3. The effect of initial H_2O_2 concentration.

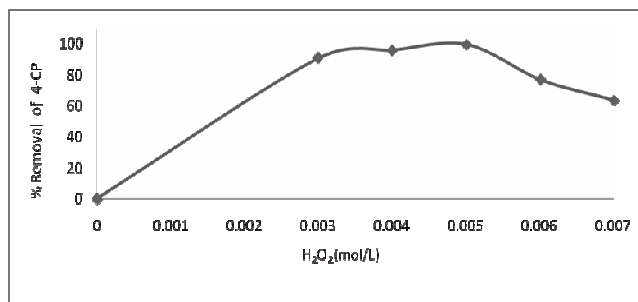


Fig.9: Degradation of 4-CP as a function of H_2O_2 initial concentration by UV/ $\text{H}_2\text{O}_2/\text{Fe}^{+3}$ system, $\text{Fe}^{+3}=0.078 \times 10^{-3}$ mol/L, 4CP= 0.39×10^{-3} mol/L ($\text{Fe}^{+3}/4\text{-CP}=0.2$), pH=3, irradiation time 30 min.

3.2.2. Reaction rate constant for UV/ $\text{H}_2\text{O}_2/\text{Fe}^{+3}$ system at constant Fe^{+3}

The experimental data obtained for 4-CP degradation can be fitted according to a pseudo-first-order reaction; the results are plotted in Figs. 10 and 11. From these results it can be observed that addition of Fe^{+3} to UV/ H_2O_2 system with ratio of $\text{H}_2\text{O}_2/\text{Fe}^{+3}/4\text{-CP}$ equal to 13/0.2/1 enhanced the rate of 4-CP degradation by a factor of 1.9 (from 0.086 to 0.164 min^{-1}) and decrease the amount of H_2O_2 by a factor of 6 (from 0.03 to 0.005 mol/L).

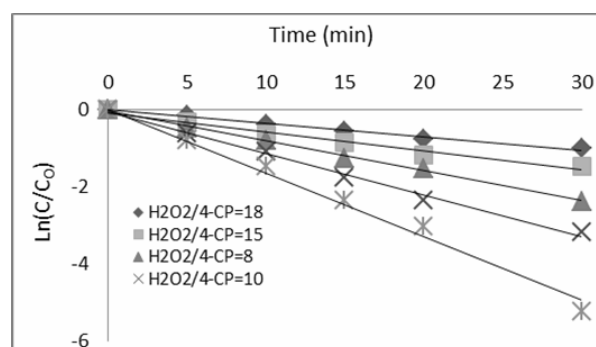


Fig.10: Pseudo-first-order rate constant for 4-CP degradation by UV/ $\text{H}_2\text{O}_2/\text{Fe}^{+3}$ system, $\text{Fe}^{+3}=0.078 \times 10^{-3}$ mol/L, 4-CP = 0.39×10^{-3} mol/L ($\text{Fe}^{+3}/4\text{-CP}=0.2$), pH=3.

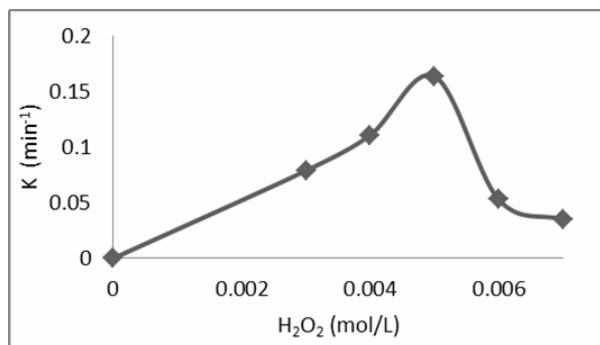


Fig.11: Pseudo-first-order rate constant for 4-CP degradation as a function of H₂O₂ initial concentration by UV/H₂O₂/Fe³⁺ system, 4-CP = 0.39×10^{-3} mol/L, Fe³⁺ = 0.078×10^{-3} mol/L (Fe³⁺/4CP = 0.2), pH = 3, irradiation time = 30 min.

3.2.3. Effect of using Fe²⁺ or Fe³⁺ on UV/H₂O₂/Fe³⁺ system

Iron in its ferrous Fe²⁺ ($\text{FeSO}_4 \cdot 7\text{H}_2\text{O}$) and ferric Fe³⁺ ($\text{Fe}_2(\text{SO}_4)_3 \cdot 7\text{H}_2\text{O}$) form was used as photocatalyst in the photo-Fenton system. Experiments with 4-CP concentration of 0.39×10^{-3} mol/L, H₂O₂ of 0.005 mol/L, Fe²⁺ or Fe³⁺ of 0.078×10^{-3} mol/L and pH = 3 were carried out in order to study the influence of using Fe²⁺ or Fe³⁺ on the degradation process. The results are plotted in Fig. 12. It can be seen from this figure, a slight increase in degradation was obtained for Fe³⁺ photocatalyst. This may be illustrated as, the Fenton process is carried out in presence of Fe²⁺ as catalyst; however the mineralization step appears to be driven by Fe³⁺ catalyzed processes, especially in the presence of light (Pignatello et al., 1999). In the light of the experimental results besides the fact that degradation appears to be driven by Fe³⁺, Fe³⁺ has been selected as catalyst to be used in the photo-Fenton experiments.

3.2.4. The effect of initial Fe³⁺ concentration on UV/H₂O₂/Fe³⁺ system

The effect of initial Fe³⁺ concentrations on photo-Fenton process was tested by carrying out experiments with various amounts of Fe³⁺ (0.04, 0.078, 0.16, 0.23 and 0.31) $\times 10^{-3}$ mol/L. Fe³⁺/4-CP ratios for these concentrations were 0.1, 0.2, 0.4, 0.6 and 0.8 respectively. The optimum H₂O₂ concentration 0.005 mol/L (i.e. the ratio of H₂O₂/4-

CP = 13) was used in these experiments. The results are plotted in Figs. 13 and 14. From these figures it can be noticed that the addition of Fe³⁺ enhanced the efficiency of UV/H₂O₂ system for 4-CP degradation. The degradation rate of 4-CP distinctly increased with increasing amounts of the iron salt. It reached its maximum value at 0.16×10^{-3} mol/L Fe³⁺ (Fe³⁺/4-CP ratio = 0.4) after about 10 min of irradiation time. The addition of the iron salt above this value did not affect the degradation, and had a negative effect.

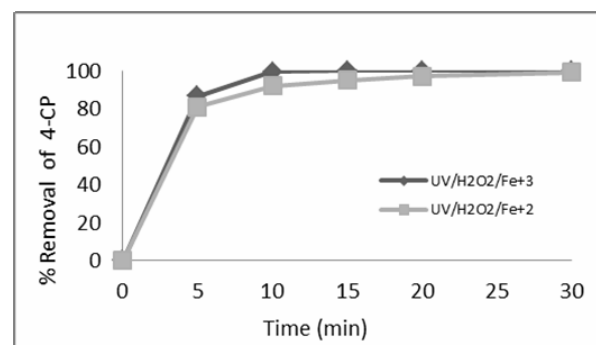


Fig.12: The effect of Fe²⁺ and Fe³⁺ on the 4-CP degradation by UV/H₂O₂/Fe system, 4-CP = 0.39×10^{-3} mol/L, H₂O₂ = 0.005 mol/L (H₂O₂/4-CP = 13), Fe²⁺ = Fe³⁺ = 0.078×10^{-3} mol/L (Fe/4-CP = 0.2), pH = 3.

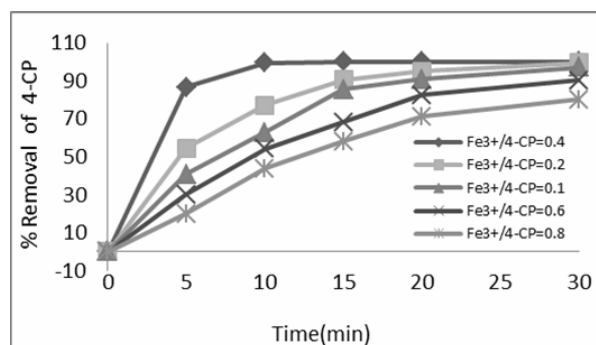


Fig.13: Degradation of 4-CP by UV/H₂O₂/Fe³⁺ system, H₂O₂ = 0.005 mol/L, 4-CP = 0.39×10^{-3} mol/L (H₂O₂/4-CP = 13), pH = 3. The effect of initial Fe³⁺ concentration.

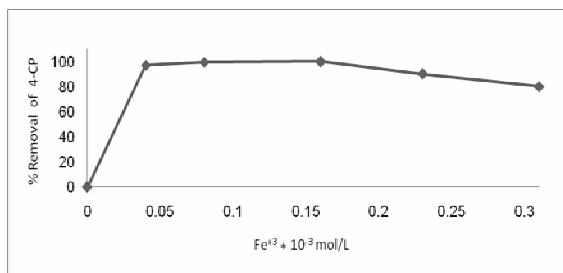


Fig.14: Degradation of 4-CP as a function of Fe^{+3} initial concentration, $\text{H}_2\text{O}_2 = 0.005 \text{ mol/L}$, $4\text{-CP} = 0.39 \times 10^{-3} \text{ mol/L}$ ($\text{H}_2\text{O}_2/4\text{-CP} = 13$), $\text{pH} = 3$, irradiation time 30 min.

3.2.5. Reaction rate constant for $\text{UV}/\text{H}_2\text{O}_2/\text{Fe}^{+3}$ system at constant H_2O_2

The experimental results in Figs. 15 and 16 show that the reaction rate was of a first order and the photo-Fenton process had a significant accelerating effect on the rate of oxidation of 4-CP. The reaction rate constant reaches its maximum value at $0.16 \times 10^{-3} \text{ mol/L}$ Fe^{+3} (i.e. $\text{H}_2\text{O}_2/\text{Fe}^{+3}/4\text{-CP}$ ratio = $13/0.4/1$). It can be observed that the photo-Fenton process enhanced the rate of 4-CP oxidation by a factor of 7 compared with $\text{UV}/\text{H}_2\text{O}_2$ system (i.e. K increased from 0.086 to 0.614 min^{-1}). The optimum ratio for $\text{H}_2\text{O}_2/\text{Fe}^{+3}/4\text{-CP}$ was $13/0.4/1$ which represents a ratio of 31 for $\text{H}_2\text{O}_2/\text{Fe}^{+3}$. This result is in a good agreement with Kavitha and Palanivelu (2004), they reported that the optimal ratio was 20–40 and also with Kuo and Wu (2010), they showed that the optimal ratio of $\text{H}_2\text{O}_2/\text{Fe}^{+3}$ was 40.

3.3. Effect of the pH value on $\text{UV}/\text{H}_2\text{O}_2/\text{Fe}^{+3}$ system

The photo-Fenton reaction is strongly affected by the pH-dependence. The pH value influences the generation of OH radicals and thus the oxidation efficiency. Different values of pH (2, 3, 4 and 5) were used to show its influence on the degradation of 4-CP. The results are plotted in Figs. 17 and 18. From these figures, it can be noticed that the maximum degradation was obtained with the system $\text{UV}/\text{H}_2\text{O}_2/\text{Fe}^{+3}$ at $\text{pH} = 3$. For pH values above 3 the degradation strongly decreases, that is because at higher pH values iron precipitates as hydroxide and that reduces the transmission of the radiation. At lower levels of pH

self-decomposition of hydrogen peroxide is promoted (Meric et al., 2004).

Therefore, a balance must be maintained to get an optimum condition. Figs. 19 and 20, illustrate the influence of pH values on the reaction rate of 4-CP.

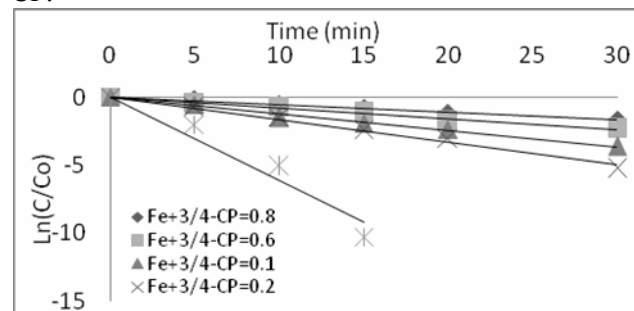


Fig.15: Pseudo-first-order rate constant for 4-CP degradation by $\text{UV}/\text{H}_2\text{O}_2/\text{Fe}^{+3}$ system, $\text{H}_2\text{O}_2 = 0.005 \text{ mol/L}$, $4\text{-CP} = 0.39 \times 10^{-3} \text{ mol/L}$ ($\text{H}_2\text{O}_2/4\text{-CP} = 13$), $\text{pH} = 3$.

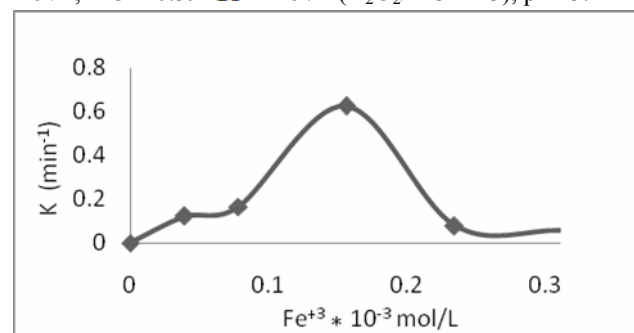


Fig.16: Pseudo-first-order rate constant for 4-CP degradation as a function of Fe^{+3} initial concentration by $\text{UV}/\text{H}_2\text{O}_2/\text{Fe}^{+3}$ system, $\text{H}_2\text{O} = 0.005 \text{ mol/L}$, $4\text{-CP} = 0.39 \times 10^{-3} \text{ mol/L}$ ($\text{H}_2\text{O}_2/4\text{-CP} = 13$), $\text{pH} = 3$, irradiation time 30 min.

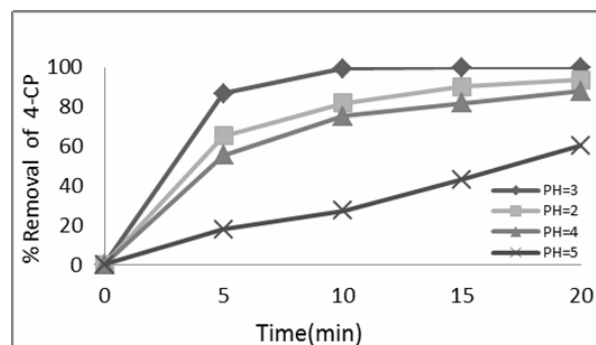


Fig.17: Degradation of 4-CP at different pH values by $\text{UV}/\text{H}_2\text{O}_2/\text{Fe}^{+3}$ system, $\text{Fe}^{+3} = 0.16 \times 10^{-3} \text{ mol/L}$, $\text{H}_2\text{O}_2 = 0.005 \text{ mol/L}$, $4\text{-CP} = 0.39 \times 10^{-3} \text{ mol/L}$.

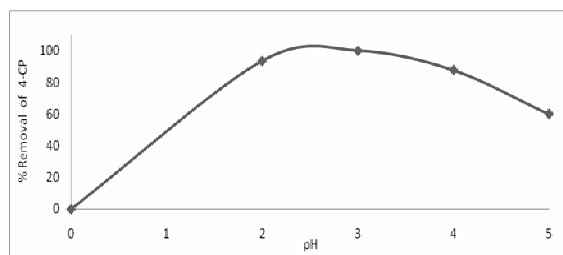


Fig.18: Degradation of 4-CP as a function of pH values by UV/H₂O₂/Fe⁺³ system, Fe⁺³ = 0.16*10⁻³ mol/L, H₂O₂ = 0.005mol/L, 4CP=0.39*10⁻³ mol/L, irradiation time 20 min.

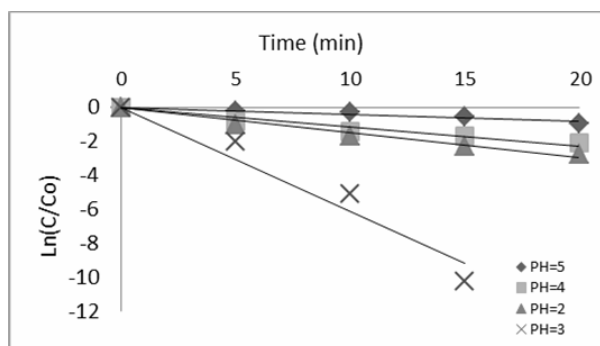


Fig.19: Pseudo-first-order rate constant for 4-CP degradation by UV/H₂O₂/Fe⁺³ system at different values of pH, Fe⁺³=0.16*10⁻³ mol/L, H₂O₂=0.005 mol/L, 4-CP=0.39*10⁻³ mol/L.

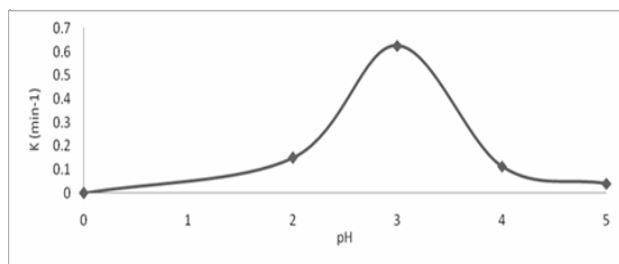


Fig.20: Pseudo-first-order rate constant for 4-CP degradation by UV/H₂O₂/Fe⁺³ system as a function of pH, Fe⁺³=0.16*10⁻³ mol/L, H₂O₂=0.005 mol/L, 4-CP=0.39*10⁻³ mol/L, irradiation time 20 min.

3.4. Effect of initial 4-CP concentration on UV/H₂O₂/Fe⁺³ system

Experiments with 10ppm (0.078 *10⁻³ mol/L) and 100ppm (0.78 *10⁻³ mol/L) of 4-CP in the UV/H₂O₂/Fe⁺³ system were performed to see the

effect of initial concentration change on the degradation process. Figs. 21 and 22, show the UV-vis spectra for 4-CP degradation and its products at different irradiation time at 10 and 100ppm respectively. Referring to Figs. 21A and B, a high powerful oxidization ability for photo-Fenton system toward low level concentration of 4-CP (10ppm) was observed.

No absorbance in the region of intermediate degradation products was observed for hydroquinone (221 and 290 nm) and benzoquinone (247 and 500nm). After only 5 min of irradiation time a complete degradation of 4-CP was observed. Referring to Figs. 22A and B, for high 4-CP concentration (100ppm), a gradual rise in the base line over time was observed. The base line reached a maximum and then tended to decrease gradually for longer irradiation times. This can be the result of the accumulation of degradation products such as hydroquinone which absorb light at about the same wavelength range (221 and 290) nm as 4-CP and benzoquinone (at 247nm). In the visible spectrum, the signal of benzoquinone (at 500nm) is small, but it can be observed at all the times of the experiment.

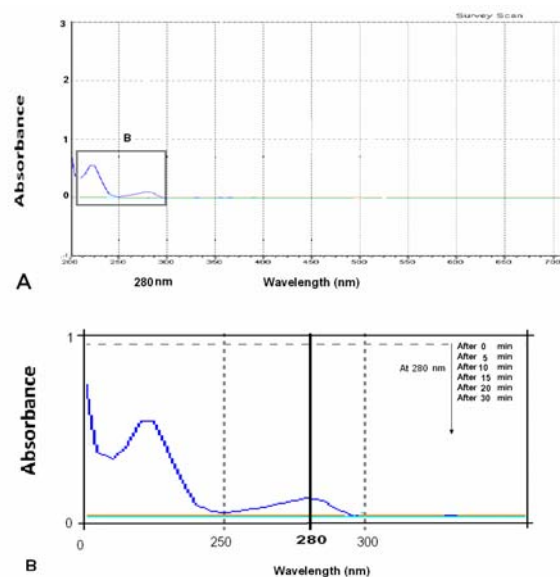


Fig.21(A and B): UV-visible spectra for 4-CP degradation by UV/H₂O₂/Fe⁺³ system, Fe⁺³ = 0.16*10⁻³ mol/L, H₂O₂ = 0.005, 4-CP= 0.078 *10⁻³ mol/L (10ppm), pH=3, irradiation time 30min.

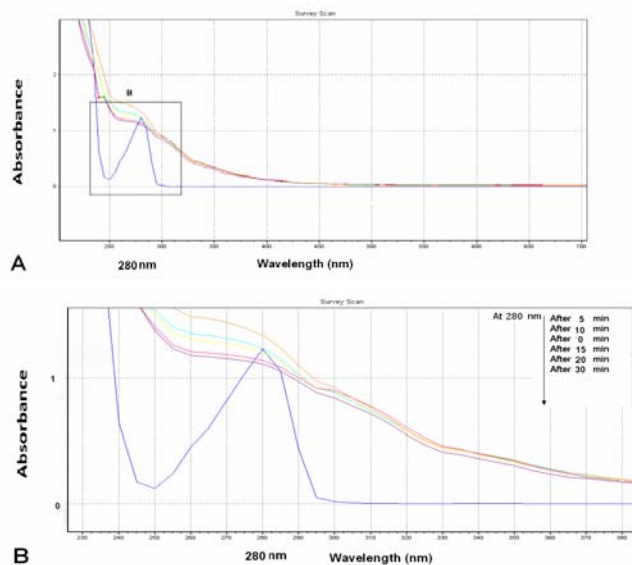


Fig.22(A and B): UV-visible spectra for 4-CP degradation by UV/H₂O₂/Fe⁺³ system, Fe⁺³ = 0.16 * 10⁻³

mol/L, H₂O₂ = 0.005 mol/L, 4-CP = 0.78 * 10⁻³ mol/L (100ppm), pH = 3, irradiation time 30 min.

3.5. Evolution of color due to intermediate formation

The main intermediates that were generated during the 4-CP degradation are hydroquinone and benzoquinone. Hydroquinone was the primary formed product from the degradation of 4-CP. A colored solution of benzoquinone could be observed through the first 5 minutes of irradiation time for UV/H₂O₂ system when low concentration (0.01mol/L) of H₂O₂ was used. This can be indicated from the absorption peaks that appear at 500nm, Fig.23. The initial colorless of the solution became green in first 5 minutes of reaction and then dark green after 15 minutes, and gradually the color intensity decreased, finally disappeared, Fig 24. Also the colored solution of benzoquinone could be observed through the first 5 min for the UV/H₂O₂/Fe⁺³ system at high concentration (100ppm) of 4-CP. It can realized that when there is insufficient amount of reagents required to degraded the 4-CP, intermediate compounds from the degradation product were formed and remain in the

solution where longer irradiation time for complete degradation and mineralization of 4-CP is required.

3.6. Comparison between UV/H₂O₂ and UV/H₂O₂/Fe⁺³ systems

The photo degradation of 4-CP was investigated in both systems UV/H₂O₂ and photo-Fenton UV/H₂O₂/Fe⁺³. The optimum results are listed in Table 3. It can be indicated that the photo-Fenton system had a significant accelerating effect on the rate of oxidation of 4-CP. The data in Table 3 show that adding Fe⁺³ to the UV/H₂O₂ system enhanced the rate of 4-CP oxidation by a factor of 7, reduce the consumption of H₂O₂ by a factor of 6 and the irradiation time required for complete degradation was reduced by a factor of 6. The intermediate products were also minimized.

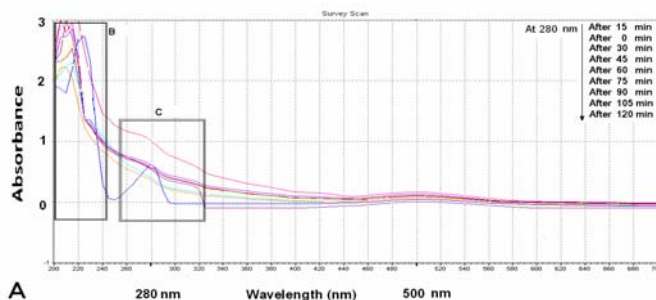


Fig.23: UV-visible spectra for the 4-CP degradation and its photoproducts, 4-CP = 0.39*10⁻³mol/L, H₂O₂=0.01 mol/L, pH = 3.

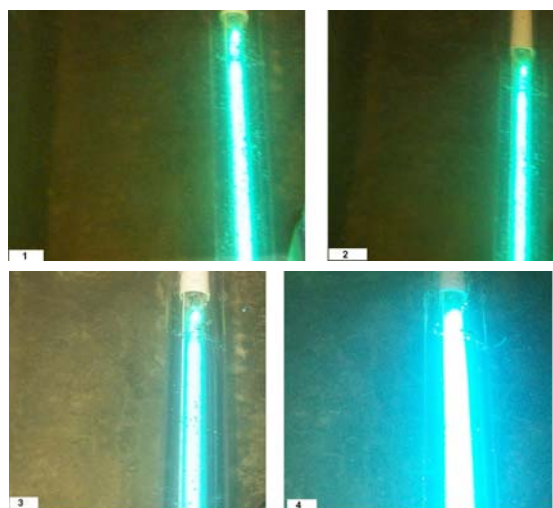


Fig.24: Closer photos inside the reactor for the color evolution in 4-CP solution, H₂O₂ = 0.01mol/L, 4-CP = 0.39*10⁻³mol/L, pH=3, irradiation time 120 min.

Table 3

A comparison between UV/H₂O₂ and UV /H₂O₂/Fe⁺³ systems

System	H ₂ O ₂ (mol/L)	Fe ⁺³ (mol/L)	pH	Irradiation time(min)	K (min ⁻¹)
UV/H ₂ O ₂	0.03	--	3	90	0.086
UV/H ₂ O ₂ /Fe ⁺³	0.005	0.16*10 ⁻³	3	15	0.614

4. Conclusions

The main conclusions that can be drawn from the experimental work of this study are as follows:

1. When there is insufficient amount of reagents required to degrade 4-CP, intermediate compounds from the degradation product are formed, remain in the solution and need longer irradiation time for complete degradation and mineralization. The intermediate products are identified:

- At low concentration of H₂O₂ (0.01mol/L) in UV/H₂O₂ system for 4-CP at concentration of 50ppm.
- At high concentration of 4-CP (100ppm) for UV/H₂O₂/Fe⁺³ system at H₂O₂ concentration of 0.005mol/L.

2. When insufficient amounts of reagents are used, a colored substance (benzquinone) was formed in the above systems (smaller signal of benzquinone for UV/H₂O₂/Fe⁺³ system) after 5 min of irradiation time then the color intensity are decreased and disappeared at longer irradiation time ,120min for UV/H₂O₂ and 30min in UV/H₂O₂/Fe⁺³ systems.

3. The study showed that the photo-Fenton process, was the most effective treatment process under acidic conditions pH=3 and produced a higher rate of degradation of 4-CP at a short irradiation time. The results show that adding Fe⁺³ to the UV/H₂O₂ system with a molar ratio of H₂O₂/Fe⁺³/4-CP equal to 13/0.4/1 enhanced the rate of 4-CP oxidation by a factor of 7, reduce the consumption of H₂O₂ by a factor of 6 and the irradiation time required to complete degradation was reduced by a factor of 4.5. The intermediate and colored products were also minimized.

4. The experimental results showed that the optimum reagents for a complete degradation of 4-CP (50ppm) were obtained at pH=3, H₂O₂=0.005 mol/L, Fe⁺³=0.016 mol/L and irradiation time of

15 min for UV/H₂O₂/Fe⁺³ system with a molar ratio of H₂O₂/Fe⁺³/4-CP equal to 13/0.4/1.

References

Alnaizy, R., and Akgerman, A. (2000). "Advanced oxidation of phenolic compounds, "Advances in Environ. Research, 4, (3), 233-244.

Bogatu,C., Botau,D., Vlaicu,I.,Chis, D., Marsavina, D., Mosoarca, G., Iovi, A. (2005)."Studies Concerning Some Phenolic Compounds Oxidation by Chlorine Dioxide in Water Solutions,Chem.Bull."POLITEHNICA" Univ. (Timișoara) , 50 :1-2.

Carneiro, P.A., Pupo Nogueira, R.F., Zandoni, M.V.B. (2007)."Homogeneous photo degradation of C.I. Reactive Blue 4 using a photo-Fenton process under artificial and solar irradiation, Dyes Pigm.,7: 127-132.

Chiu, K., Lyn, D. A., Savoye, P., Blatchley, E. R. (1999) ."Integrated UV disinfection model based on particle tracking, J. Environ. Eng., 125 : 7-16 .

Elghniji, K., Hentati, O., Mlaik, N., Mahfoudh, A., Ksibi, M. (2011) . "Photocatalytic degradation of 4-chlorophenol under P-modified TiO₂/UV system: Kinetics, intermediates, phytotoxicity and acute toxicity , J. Environ. Sci., 23.

Hirvonen, A., Trapido, M., Hentunen, J., and Takharen, J. (2000) ."Formation of hydroxylated and dimeric intermediates during oxidation of chlorinated phenols in aqueous solution, Chemosphere, 41, 1211-1218.

Kavitha, V., Palanivelu, K. (2004)."The role of ferrous ion in Fenton and photo-Fenton processes for the degradation of phenol, Chemosphere, 55: 1235–1243.

Kralik, P., Kusic, H., Koprivanac, N., Bozic, A.L., (2009) ."Degradation of chlorinated hydrocarbons by UV/H₂O₂: The application of experimental design and kinetic modeling approach, Chem. Eng. J.,158 : 154–166.



- Kuo, W.S., Wu, L.N. (2010) .Fenton degradation of 4-chlorophenol contaminated water promoted by solar irradiation , Sol. Energy, 84 : 59–65.
- Kutschera, K., Bornick, H., Worch, E. (2009). Photoinitiated oxidation of geosmin and 2-methylisoborneol by irradiation with 254 nm and 185 nm UV light ,J. Water Res.,43: 2224–2232.
- Lyn, D.A., ASCE, A.M., Blatchley, E. R. (2005). Numerical computational fluid dynamics- based models of ultraviolet disinfection channels, J. Environ. Eng., 131: 838-849.
- Matilainen, A., Sillanp, M. (2010) .Removal of natural organic matter from drinking water by advanced oxidation processes, J. Chemosphere ,80 : 351–365.
- Meric,S., Kaptan, D., and Olmez, T. (2004). Colour and COD removal from wastewater containing Reactive Black 5 using Fenton's oxidation process, Chemosphere, 54: 435–441.
- Munter, R. (2001) “Advanced oxidation processes- currents status and prospects”, Proc. Estonian Acad. Sci. Chem.,50 :59-80.
- Murcia, M.D., Gomez, M., Gomez, E.,Gomez, J.L., Christofi, N. (2009) .Comparison of different advanced oxidation processes for degrading 4-chlorophenol, World Academy of Science, Engineering and Technology, 55.
- Nogueira, K. R. B., Teixeira, A. C. S. C., Nascimento, C. A. O., Guardani, R. (2008). "Use of Solar Energy in the Treatment of Water contaminated with phenol by photochemical processes , Braz. J. Chem. Eng., 25: 671 – 682.
- Pignatello, J., Liu, D., Huston, P. (1999). Evidence for an additional oxidant in the photoassisted Fenton reaction,,J., Environ., Sci., Technol., 33: 1832-1839.
- Pera-Titus, M., Garcia-Molina, V., banos, M.A., Gimenez,J.,Esplugas,S. (2004) .Degradation of chlorophenols by means of advanced oxidation processes: a general review, Appl. Catal. B: Environ. 47, 219–256.
- Shihab, A. H., (2011). "Removal of organic compounds from simulated wastewater by advanced oxidation processes, Ph.D.Thesis, university of Baghdad.
- Stoyanova, M., Christoskova,St.G.,Georgieva, M., (2003). Low- temperature catalytic oxidation of water containing 4-chlorophenol over Ni-oxide catalyst, Appl. Catal., A A, 248 : 249-259 .
- Tang, W. Z.,(2004) Physicochemical Treatment of Hazardous Wastes. CRC Press.
- Thomas , O., and Burgess, C. (2007). "UV-visible spectrophotometry of water and wastewater , 1st ed., Elsevier publisher , Canada.
- Weber, R.,Smith, E. (1986). "Removing dissolved organic contaminants from water", Environ.,Sci.,&Technol., 20: 970-979.
- WHO (World Health Organization), (1998). Guidelines for drinking water quality", vol.2, Health criteria and other supporting information, Geneva.
- WHO (World Health Organization),(2008). Guidelines for drinking water quality, Vol.1, Recommendations. – 3rd ed., Geneva.



Fatigue Analysis of Hip Prosthesis

Prof. Dr. Adnan N. Jameel Dr. Wedad I. Majeed Alaa Mohammed Razzaq

Dep. of Mech.
College of Engineering
University of Baghdad

Abstract

The present work covers the analytical design process of three dimensional (3-D) hip joint prosthesis with numerical fatigue stress analysis. The analytical generation equations describing the different stem constructive parts (ball, neck, tour, cone, lower ball) have been presented to reform the stem model in a mathematical feature. The generated surface has been introduced to FE solver (Ansys version 11) in order to simulate the induced dynamic stresses and investigate the effect of every design parameter (ball radius, angle of neck, radius of neck, neck ratio, main tour radius, and outer tour radius) on the max. equivalent stresses for hip prosthesis made from titanium alloy. The dynamic loading case has been studied to a stumbling case. The load has been applied on the cap tip as a concentrated load distributed on the interface of ball and socket. The results show that the decreasing of max. Fatigue stress by (175) MPa could be obtained by increasing the outer tour radius from (10)mm to (15) mm and that will change the max. Fatigue zone location from the tour section to the neck. The ball radius and neck angle must be as lower as possible to decrease the fatigue stresses. The most dominate parameter to increase the safety factor is the radius of neck.

Key words: Stem modeling, Hip implant, Hip prosthesis, Fatigue analysis.

الخلاصة:

هذا العمل يغطي تصميم بديل مفصل الورك ثلاثي الابعاد مع التحليل العددي لاجهادات الكلال. معادلات التوليد النظرية التي تصف الاجزاء البنائية للبدال (الكرة، العنق، الوصلة، المخروط، الكرة السفلى) تم تقديمها لتكوين نموذج البديل بصورة رياضية. اما ادخال السطح المولد الى محلل العناصر المحددة (Ansys version 11) لمحاكاة الاجهادات الديناميكية المتولدة ودراسة تأثير كل متغير (نصف قطر الكرة العليا، زاوية ميل العنق، نصف قطر العنق، نسبة العنق، نصف قطر الوصلة الرئيسي، نصف قطر الوصلة الخارجي) على الاجهادات العظمى المكافئة لبديل ورك مصنوع من سبيكة التيتانيوم حالة التحميل الديناميكية درست لحالة التعثر. تم تسليط حمل مركز على قمة غطاء المفصل وموزعاً على سطح الكرة والتجويف. اظهرت النتائج بأنه يمكن تقليل اجهاد الكلال الاعظم بمقدار 175 ميكا باسكال بزيادة نصف قطر الوصلة الخارجي من (10) الى (15) ملم و ذلك سوف يغير موقع منطقة اعظم اجهاد كلال من مقطع الوصلة الى منطقة العنق. نصف قطر الكرة و زاوية العنق يجب ان يكونا باقل مايمكن لتقليل اجهادات الكلال. المتغير الاكثر تأثيرا في زيادة معامل الامان هو نصف قطر العنق.

1.1. Introduction

Model generation means a process of generating the nodes and elements that represent the spatial volume and connectivity of the actual system [Kassim, 1997]. The accurate geometrical representation of stem surface is the first step to a successful computerized stem design which represents base of subsequent analysis such as static stress analysis (combined and contact), fatigue stress investigation, impact stress and vibration to ensure a successful stem implant design. This paper presents a mathematical model able to compute the different surfaces of stem joint (upper ball, neck, tour, cone, and lower ball). The numerical representation of the prosthesis surface how to choice the element type, how to apply load and an overview to fatigue theory are presented at last, The adopted stress analysis fatigue theory is soderberg theory with a high cyclic loading.

1.2. Literature Survey

T. P. Colleton et al (1993) [13] described the cement mantle of an artificial hip joint and subjected to detailed failure analysis. Results from a finite element analysis were used, together with the techniques of fracture mechanics, in an attempt to explain the magnitude and direction of fatigue cracking. Fracture mechanics calculations indicate that the local stress intensity in the region of the principal defect would have been sufficient to exceed the threshold for fatigue crack propagation in this material.

B.A.O. McCormack and P. J. Prendergas(1999) [14] show how fatigue damage accumulation occurs in the cement layer of a hip replacement, a physical model of the joint was used in an experimental study. The model generates the stress pattern found in the cement layers whilst at the same time allowing visualization of micro crack initiation and growth. In this way the gradual process of damage accumulation can be determined. Six specimens were tested to 5 million cycles and a total of 1373 cracks were observed. It was found that, under the flexural loading allowed by the model, the majority of cracks come from pores in the bulk cement. Furthermore, the lateral and medial sides have

statistically different damage accumulation behaviors, and pre-load cracks significantly accelerate the damage accumulation process. The experimental results confirm that damage accumulation is continuously increasing with load in the form of crack initiation and crack propagation.

A. Z. Senalp et al(2007) [9] study dynamic stresses varying in time and resulting in the fatigue failure of implant material. In this study, four stem shapes of varying curvatures for hip prosthesis were modeled. Static, dynamic and fatigue behavior of these designed stem shapes were analyzed using commercial finite element analysis ANSYS software. Static analyses were conducted under body load. Dynamic analyses were performed under walking load. Fatigue behavior of stem shapes was predicted using ANSYS Workbench software. Performance of the stem shapes was investigated for Ti-6Al-4V and cobalt-chromium metal materials and compared with that of a commonly used stem shape developed by Charnley.

T. P. Andriacchi et al(2009) [22] used two-dimensional stress analysis to study the effects of some of the factors leading to early fatigue failure of the femoral stem in total hip prosthesis.

The results show that loss of proximal stem support at the level of the calcar femorale will result in stem stress levels which can lead to fatigue failure, in addition, the role of the body weight and range of cyclic stress fluctuation play an important role in fatigue life under conditions where the stem has lost proximal support.

These results indicate that stem design could be improved by incorporating some means of ensuring adequate support at the calcar femoral and by increasing cross sections in the middle one-third of the stem where maximum tensile stresses are found to occur.

2. Mathematical Representation

Herein three dimensional (3-D) model representation of a hip joint prosthesis consists of five constructive parts will be derived analytically depending on each part shape. The different stem parts are:



- 1- Bottom sphere
- 2- Cone
- 3- Tour interface
- 4- Neck
- 5- Upper sphere

The equations that generate the whole surface are:-

Bottom Sphere: This surface is a half sphere which represents the bottom of stem and its equations are [Fumihiro and ko, 2002]:

$$x^2 + y^2 + z^2 = r_i^2 \quad (1)$$

The spherical coordinate system relates to the Cartesian system in the following equations [Niel Pieterse, 2006]:

$$\left. \begin{aligned} x &= r_i * \cos \theta * \cos \phi \\ y &= r_i * \sin \theta * \cos \phi \\ z &= r_i * \sin \phi \end{aligned} \right\} \quad (2)$$

The different variables in eq.(2), (r_i) is the bottom sphere radius, $\theta = 0$ to 360 degree, $\phi = 0$ to 180 degree are shown in Figure (1).

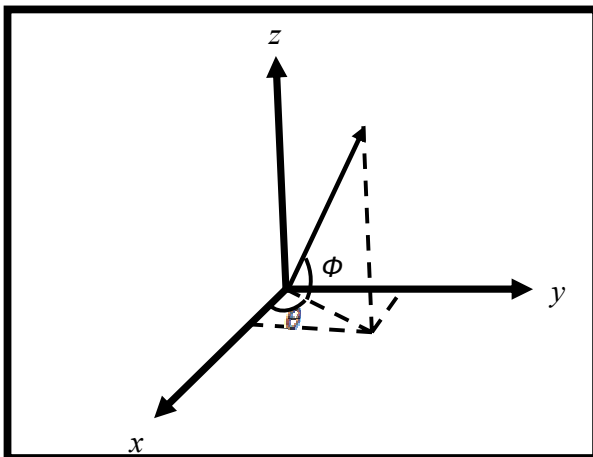


Figure (1), Spherical coordinates System Coordinate

Cone Surface: This section is so important in the fixation of stem in femur and it is non-complete cone. The generation's equations for any cone section are:

$$x^2 + y^2 = r^2 \quad (3)$$

Where (r) is a function of (z) see Figure (2). From the trigonometric relationship the following equations could be concluded:

$$\begin{aligned} r_o / (l + z_1) &= (r_o - r_i) / l \\ z_1 &= (l * r_i) / (r_o - r_i) \end{aligned} \quad (4-a)$$

Where (r_o) is the upper cone radius, (r_i) is the bottom cone radius and (l) is the cone length then:

$$r = (z + z_1)(r_o - r_i) / l \quad (4-b)$$

Sub eq.(4 - a) in eq.(4 - b) to get:

$$r = z(r_o - r_i) / l + r_i \quad (5)$$

And

$$\left. \begin{aligned} x &= r * \cos \theta \\ y &= r * \sin \theta \end{aligned} \right\} \quad (6)$$

Where (θ) = 0 to 360 degree.

Sub eq.(5) in eq.(6) to get:

$$\left. \begin{aligned} x &= (z(r_o - r_i) / l + r_i) \cos (\theta) \\ y &= (z(r_o - r_i) / l + r_i) \sin \theta \end{aligned} \right\} \quad (7)$$

From eq.(7) it is clear that :

$x = f(z, \theta)$ and $y = f(z, \theta)$ where (θ) = 0 to 360 degree and $z = 0$ to (l).

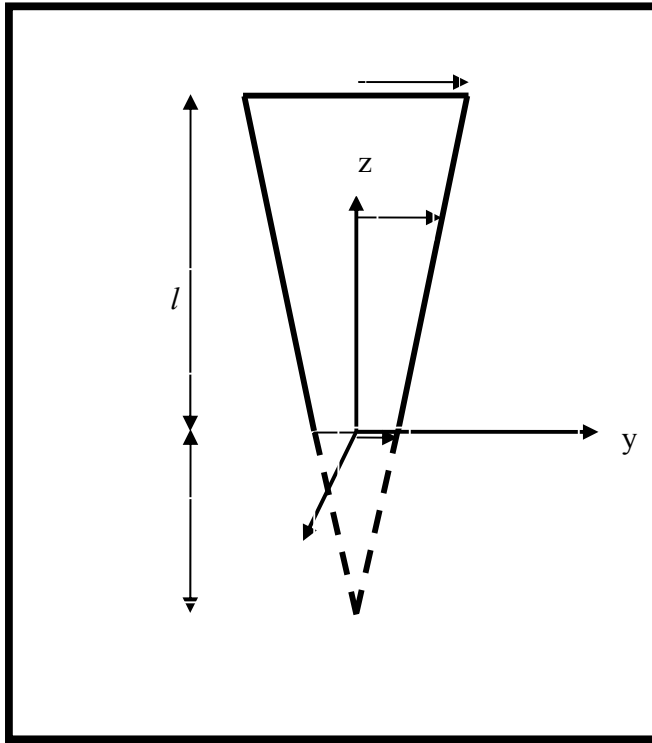


Figure (2), Cone Section

Tour Interface: Figure (3) shows the tour interface surface which represents the third section of stem prosthesis.

$$x^2 + y^2 = r^2$$

If (r) The outer cone radius (r_o) so that :

$$x^2 + y^2 = r_o^2 \quad (8)$$

Where:

$$x = r_o * \cos \theta$$

$$y = r_o * \sin \theta$$

$$z = l$$

Where (θ) = 0 to 360 degree

The coordinate transformation from circle center (O_c) to tour center (O_t) see Figure (4), are:

$$\left. \begin{aligned} x_t &= x_c \\ y_t &= y_c + r_t \\ z_t &= z_c \end{aligned} \right\} \quad (9)$$

Where (r_t) is the tour main radius.

From Figure (4), y_t and z_t system inclined from y_c and z_c by (θ_t), x_t and x_{t1} are coincide with each other, that:

$$\left. \begin{aligned} x_{t1} &= x_t \\ y_{t1} &= y_t * \cos(\theta_t) + z_t * \sin(\theta_t) \\ z_{t1} &= z_t * \cos(\theta_t) - y_t * \sin(\theta_t) \end{aligned} \right\} \quad (10)$$

Where (θ_t) is the tour angle (neck angle).

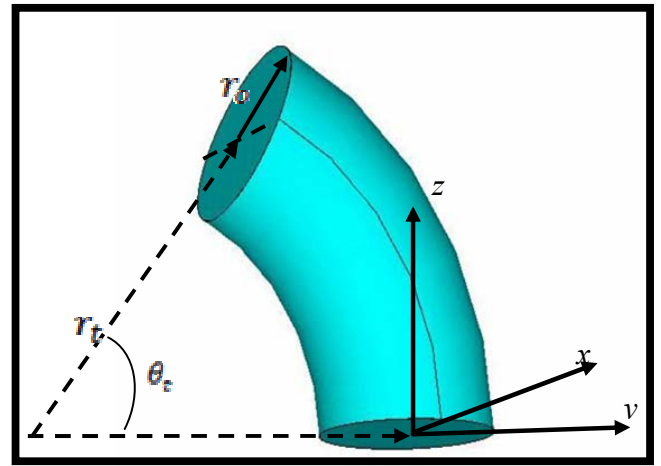


Figure (3), Tour Interface

Neck surface: which represent the weakest part in the system so that it must be studied and analyzed carefully.

This section allows more freedom in the joint movement. Figure (5) shows the neck surface and the different surface variables .In this Figure the coordinate system S_n is fixed at the middle of neck piece and it's clear that (r) is a $f(\theta_1, \theta_2)$ so that :

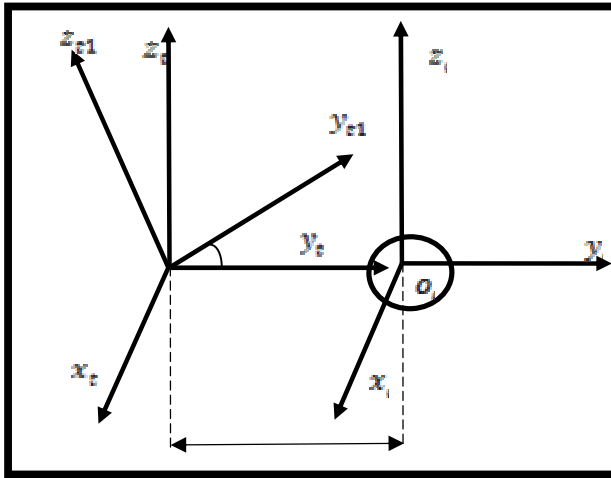


Figure (4), Transformation of Tour Coordinate.

$$\left. \begin{aligned} x_n &= 0 \\ y_n &= r_n + r_{on} (1 - \cos(\theta_i)) \\ z_n &= r_{on} * \sin(\theta_i) \end{aligned} \right\} \quad (11)$$

Where ($i=1$ for Bottom part and $i=2$ for upper part)

The coordinate transformation from S_n to S_{n1} are shown in Figure (6) and as following:

$$\left. \begin{aligned} x_{n1} &= x_n \\ y_{n1} &= y_n \\ z_{n1} &= z_n + r_{on} * \sin(\theta_1) \end{aligned} \right\} \quad (12)$$

The generation of neck surface is achieve by rotating x_{n1}, y_{n1} about z_{n1} are in Figure (7).

$$\left. \begin{aligned} x_{n2} &= x_{n1} \cos(\theta) + y_{n1} \sin(\theta) \\ y_{n2} &= y_{n1} \cos(\theta) - x_{n1} \sin(\theta) \\ z_{n2} &= z_{n1} \end{aligned} \right\} \quad (13)$$

Figure (8) shows the transformation from S_{n2} to S_{n3}

$$\left. \begin{aligned} x_{n3} &= x_{n2} \\ y_{n3} &= y_{n2} + r_t \\ z_{n3} &= z_{n2} \end{aligned} \right\} \quad (14)$$

where (r_t) It is the tour main radius.

The last transformation is to be from S_{n3} to S_{n4} coordinate system as in Figure (8).

$$\left. \begin{aligned} x_{n4} &= x_{n3} \\ y_{n4} &= y_{n3} \cos(\theta t) + z_{n3} \sin(\theta t) \\ z_{n4} &= z_{n3} \cos(\theta t) - y_{n3} \sin(\theta t) \end{aligned} \right\} \quad (15)$$

The coordinate transformation from S_{n4} to S_{n5} are :

$$\left. \begin{aligned} x_{n5} &= x_{n4} \\ y_{n5} &= y_{n4} - r_t (1 - \cos(\theta t)) \\ z_{n5} &= z_{n4} + l + r_t \sin(\theta t) \end{aligned} \right\} \quad (16)$$

as in Figure (8).

Upper Sphere Surface: The generation of upper sphere is different from the Bottom sphere surface, it is larger than a half sphere in surface and that depend upon the difference between the upper neck side radius and the upper sphere radius see Figure (9). The other difference is coordinate transformation. Where x_b, y_b and z_b can be evaluated from Eq. (2).

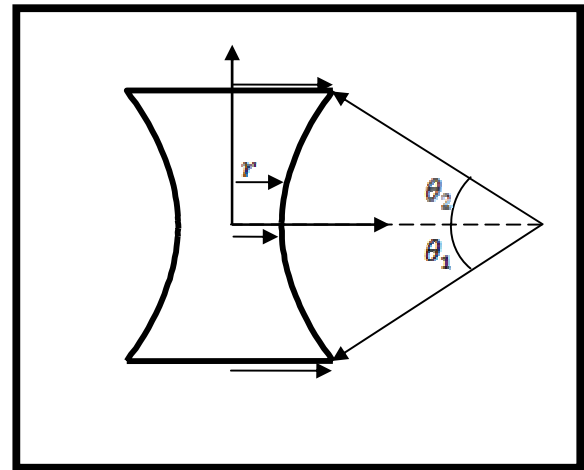


Figure (5), Neck of Stem.

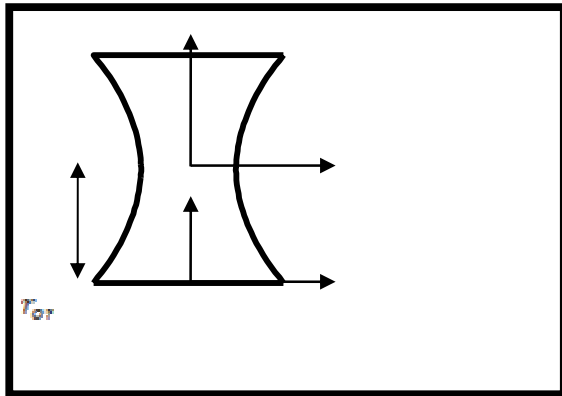


Figure (6) Coordinate Transformation from S_n to S_{n1} .

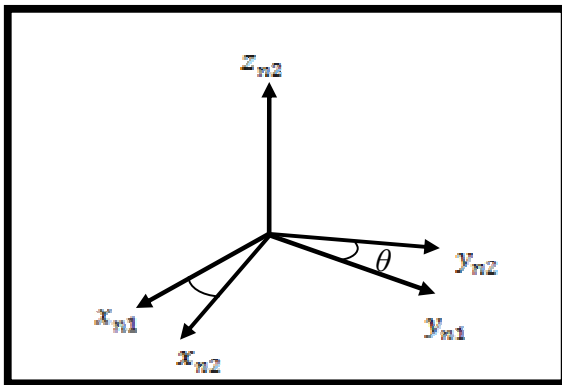


Figure (7) Generation of Neck surface.

In Figure (10) the coordinate transformation from S_b to S_{b1} , coordinate system as follows:

$$\left. \begin{aligned} x_{b1} &= x_b \\ y_{b1} &= y_b \\ z_{b1} &= z_b + A \\ A &= \sqrt{r_b^2 - r_{on}^2} \end{aligned} \right\} \quad (17)$$

Where (A) represents the upper ball offset distance.

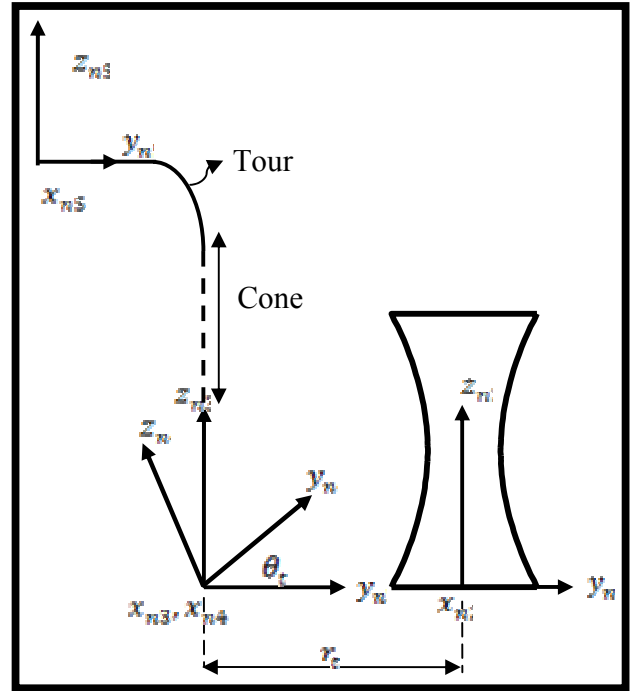


Figure (8) Transformation from S_{n2} to S_{n5}

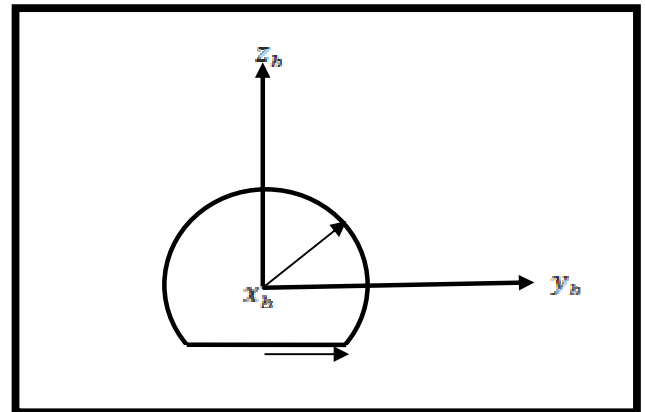


Figure (9), Upper Sphere Cross Section.

In Figure (10) the coordinate transformation from S_{b1} to S_{b2} are:

$$\left. \begin{aligned} x_{b2} &= x_{b1} \\ y_{b2} &= y_{b1} \cos(\theta_r) + z_{b1} \sin(\theta_r) \\ z_{b2} &= z_{b1} \cos(\theta_r) - y_{b1} \sin(\theta_r) \end{aligned} \right\} \quad (18)$$

The last coordinate transformation is shown in Figure (11) and as follow:

$$\left. \begin{aligned} x_{b3} &= x_{b2} \\ y_{b3} &= y_{b2} - r_c (1 - \cos(\theta_r)) - r_{on} \sin(\theta_1 + \theta_2) \sin(\theta_r) \\ z_{b3} &= z_{b2} \end{aligned} \right\} \quad (19)$$

$$z_{b3} = z_{b2} + l + r_t \sin(\theta_t) + r_{on} \sin(\theta_1 + \theta_2) \cos(\theta_t)$$

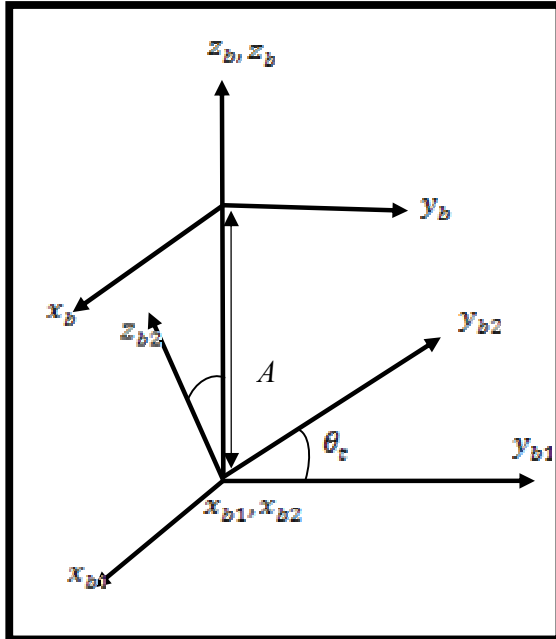


Figure (10), Transformation Coordinate System.

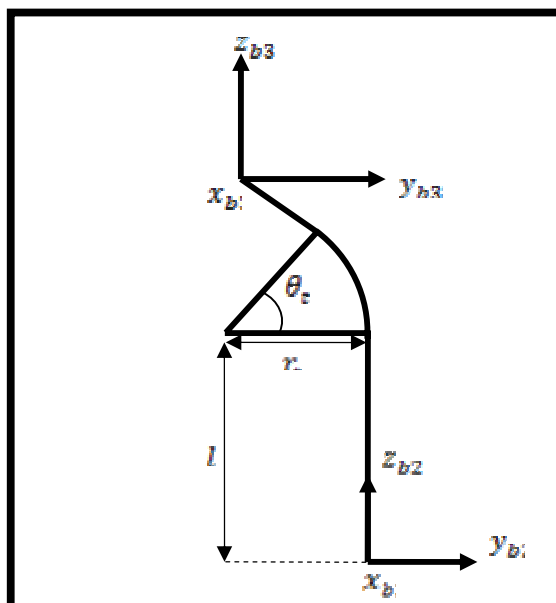


Figure (11), Transformation from S_{b2} to S_{b3} .

3. F.E. Stem Modeling:

Modeling steps of stem are:-

- 1- Build up the model .
- 2- Specify the material properties (module of elasticity and Poisson's ratio)
- 3- Specify the elements by using convergence test to choose the proper element type and number as following:
 - Building up the stem models.
 - Specifying the material properties as a structural, Titanium alloy, linear, elastic,

isotropic with $\nu = 0.32$, $E = 110,000 \text{ N/mm}^2$

[Oguz Kayabasi and Fehmi Erzincanli, 2006].

- Specifying the applied load and boundary conditions (they are the same through the convergence test).
- Specifying the element type as solid and using the following element type successively (anasio 64, Tetrahedrol 10 node 187, 8 node 185, 20 solid 186, 20 solid 95, Brick 8 node 45 and 10 node 92) with changing the coarser to each element in order to investigate the right element number as well the element type. The result of the convergence test show that the best element type that can be employed to mesh the model is solid element 92 with 24403 elements and 36343 nodes as in Figure (12), and Figure (13) [Nassear Rasheid, 2009].
- 4- Apply load to the model using a concentrated load with contact algorithm the load at each hip joint is maximum.

The force was applied to concave surface of the whole of the acetabular.

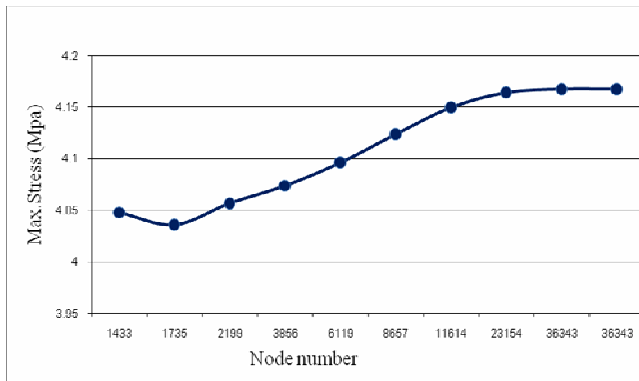


Figure (12), Convergence Test.

3.1 modeling of Contact Element:

In most mechanical and structural engineering systems interactions occur between mechanical components or two parts of a single component when they contact with each other. Contact problems are highly nonlinear and required significant computer resources to solve [James F. Doyle, 2004].

Generally the contact problems can be put in two classes [R.B. Heywood, 1969]

1. Rigid- to- flexible bodies in contact problem: in this types of contact one or more of the contacting surfaces are treated as being rigid material, which has a much higher stiffness relative to deformable body it contacts. Many metals forming problems fall into this category. This type of contact problems is used for stem in mesh.
2. Flexible- to flexible bodies in contact: both contacting bodies are deformable. This type of contact problems is used for bolted joints, and interference fits.

3.2 Contact Element Capability:

Ansys finite element analysis (FEA) program offers a variety of elements designed to treat cases of changing mechanical contact between the parts of an assembly or between the different parts of different faces of a single part. These elements range from simple, limited idealizations to complex and sophisticated [Sandro Barone and Paola Forte,

2001]. In general the contact applications can be classified into three types [Oguz Kayabasi and Fehmi Erzincanli, 2006].

1. Point- to- point contact, where the exact location of contact should be known beforehand.
2. Point- to- surface contact, where the exact location of the area may not be known beforehand.
3. Surface- to- surface contact typically used to model surface- to – surface contact applications of rigid- to – flexible classification, Which is used in this work.

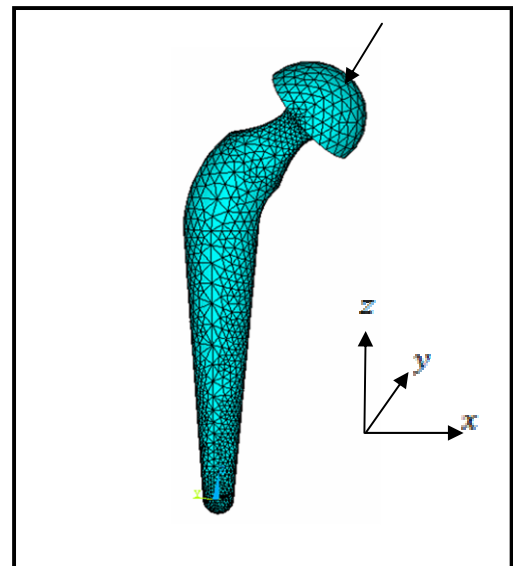


Figure (13), Stem Meshed with Solid Element 10 Nodes 92.

3.3. Material And Geometry Of Model:

The material used in this study is Titanium alloy (Ti6Al4V) with modulus of Elasticity (E)

=110,000 N/mm² and $\nu=0.32$. The properties of

prosthesis design which are used in finite element method are the same properties of [Oguz Kayabasi and Fehmi Erzincanli, 2006].



3.4. Loading Conditions:

For dynamic analysis, the maximum stumbling resultant force that applied on the surface of the implant bearing is 8.7 times the body weight (BW = 70 kg) applied at cup tip. This could be resolved into [H.F El'sheikh et al, 2003]: $F_x = 2188.86\text{N}$, $F_y = -669.53\text{N}$ and $F_z = -5472.1\text{N}$

4. Fatigue Definition:

Fatigue is the failure of a material under fluctuating stresses each of which is believed to

produce minute amounts of plastic strain[E.J.Hearn], failure is the sudden fracture after initiation and growth of a crack.

There are three factors affected on fatigue:

1. Crack length.
2. Cyclic stress.
3. Environmental conditions.

This factors affected on number of stress cycles before the final failure [Ayad Morad Alzuhairy, 2000].

5. Verification Test:-

The validity of the present work results must be checked by making a comparison with any previous work dealt with the same problem. The adopted work investigated the induced stresses in a special feature of Charnley stem by making neck cross section larger than the tour cross section (collar) under cyclic loading. The finite element model was meshed by solid 45 tetrahedron elements with total number of (10493). The applied load is used as a concentrated load with three components directed in (x, y, z) direction applied at the upper ball tip. Table (1) represents Verification of present work fatigue stresses with Ref.[Oguz Kayabasi and Fehmi Erzincanli, 2006].

Table (1) Verification of present work fatigue stresses with Ref.[Oguz Kayabasi and Fehmi Erzincanli, 2006].

Max. Equivalent Stress (MPa)	Max.Equivalent Stress(MPa),present work	Percentage Error (%)
207.447	204.44	1.4495
184.395	175.98	4.564
161.348	152.6	5.422
138.298	131.68	4.785
115.249	108.29	6.038
92.199	85.314	7.467
69.149	63.614	8.004
46.099	44.904	2.592
23.050	21.607	8.008

6. Results and Discussions:

The mechanical failure of femoral stem of total hip replacement prosthesis occurs not infrequently, probably as a result of cyclic stress above endurance limit of implant material. A good implant design should satisfy maximum or an infinite fatigue life endurance fatigue effects on stem. This can be insured by physical testing or a fatigue analysis.

The effects of surgical mechanics of implantation, prosthetic design and the prosthetic material appear to be inter related. In present study the effects of a series of variables on stress in the femoral stem and fatigue life of the prosthesis are analyzed, the variables include:-

1. Angle of neck.
2. Ball radius.
3. Main tour Radius.

4. Neck ratio.
5. Outer tour radius.
6. Radius of neck.

Figure (14) shows contour distribution of Von mises stress values due to change of effective design parameter (neck angle). While of figure (15) show contour of minimum safety factor values which calculated according to Soderberg theory due to change of the same parameters.

The variation of equivalent (Von mises) stresses under periodic loads are shown in figures (16) to (27).

From the results it is clear that the most dominant design parameter is (outer tour radius (r_o)) which has found to reduce the Von mises stress by 226 MPa because the decreasing for the moment inertia see figure (22) and increase the safety factor by 1.5 as shown in figure (23).

The second effective design parameter is the neck angle which has a direct relationship with the Von mises stresses, it is clear that the increasing of the neck angle increases the arm of the bending moment (increasing Von mises stress by 100 MPa) as shown in figure (16) and an inverse one with safety factor (decreasing the safety factor by 1.5) as shown in figure (17).

The third effective design parameter is the radius of neck which has been found to has an inverse correlation with the max. Von mises stress in the range of (10) mm to (16) mm (decreasing the Von mises by 100 MPa), the cause of that is the increasing of the moment of the inertia at the neck section, see figure (24) and a direct one with safety factor increasing the safety factor by 6) as in figure (25).

The fourth effective design parameter is the ball radius which found to has a direct relationship with the Von mises stresses in the range of (15-25) mm (increasing the Von mises stresses by 45 MPa), this is due to that increasing of the arm of the pressure center so that the bending moment increases, see figure (18) and an inverse one with safety factor in

The same range (decreasing the safety factor by 0.8) see figure (19).

The fifth effective design parameter is the neck ratio which has found to has an inverse relationship with the max. Von mises stress in the range of (0.5) to (0.8) mm (decreasing the Von mises by 30 MPa) as shown in figure (26) and has a direct one with safety factor in the same range (increasing the safety factor by 0.75) as shown in figure (27).

The sixth effective design parameter is the tour main radius (r_f) which has insignificant effect on the max. Von mises stresses and safety factor because the arm of the bending moment increasing with the increasing of mean tour radius as presented in figures (20),(21).

7. Conclusions:

1. It was found that the outer tour radius play a key role in decreasing the fatigue stresses by (175) MPa in the range of (10 to 15) mm, radius of the neck and neck raio play the same role but with a lower effect.
2. The values of the neck angle and ball radius must be as lower as possible because they have a negative effect on the max. fatigue stresses.
3. Despite of the major positive role of the outer tour radius there is a minor negative role and that is the moving of the max. Fatigue stress zone to the weakest stem section (neck) from the tour section.
4. The radius of neck has the dominate role and increasing the safety factor from (1.2 to 7.2), while the neck ratio and outer tour radius have a lower direct effect. The increasing of the neck angle and ball radius decreases the safety factor.

8. References

Ayad Morad Alzuhairy, (Study of fatigue properties of acicular ductile iron compared with steel(42 CrMo4)), M.Sc.thesis, University of technology, 2000.



E. J. Hearn, (Mechanics of materials), Book, International series on material science and technology, VOL. 19, 1977.

Fumihiro Yoshimine, Ko Ginbayashi (A mathematical formula to calculate the theoretical range of motion for total hip replacement), Journal of Biomechanics, 35 (2002) 989–993, www.elsevier.com/locate/jbiomech

H.F El'sheikh, B.J MacDonald, M.S.J. Hashmi, (Finite element simulation of the hip joint during stumbling: a comparison between static and dynamic loading), Journal of materials processing technology 143–144 (2003) 249–255.

James F. Doyle, (Modern experimental stress analysis), Book, Purdue University, Lafayette, USA, 2004.

Kassim A Abdullah, (Stress and stability analysis of the neck – stem interface of the modular hip prosthesis), Ph.D. thesis , Queen's university –Mechanical engineering ,Canada 1997.

Nassear Rasheid Hmoad, (Simulation of meshing and contact with stress analysis of hypoid gear drive), M.Sc. thesis, Baghdad university ,library of Mechanical engineering , 2009.

Niel Pieterse, (Development of a dynamic hip joint simulation model), M.Sc. thesis, University of Pretoria, 2006

Oguz Kayabasi and Fehmi Erzincanli, (Finite element modeling and analysis of a new cemented hip prosthesis), ELSEVIER, Advances in Engineering Software 37 (2006) 477–483.

R.B. Heywood, (Photoelasticity for designers), Vol. 2, 1969.

Sandro Barone and Paola Forte, (CAD / FEM procedures for stress analysis in unconventional gear applications), International Journal of computer applications in technology), Vol. 15, No. 1, 2001, pp.305-389.

9. Nomenclatures

English Symbols

Symbol	Description	Unit
A	Upper ball distance offset	mm
E	Modulus of elasticity	N/ mm^2
F	Force	N
n_r	Neck ratio=the position of the neck weakest section to neck length	
N	safety factor	
O_c	Tour circle center	
O_t	Main tour circle center	
r_b	Ball radius	mm
r_i	The bottom sphere radius, the bottom cone radius	mm
r_n	Neck radius	
r_o	The upper cone radius, the outer cone radius	mm
r_{on}	The outer radius of neck	
r_f	Main tour radius	
R_s	Stress ratio	
$S_n(x_n, y_n, z_n)$	The coordinate system of Neck	
x, y, z	Cartesian coordinate	

10. Greek symbols

Symbol	Description	Unit
θ_t	The tour angle or Neck angle	degree
θ	Angle between project (r_i) on (x-y) plane and (x) axis in spherical coordinate system.	degree
ν	Poisson's ratio	-
σ_{\max}	Maximum stress	MPa
σ_{\min}	Minimum stress	MPa
ϕ	Angle between (r_i) and project (r_i) on (x-y) plane	Degree

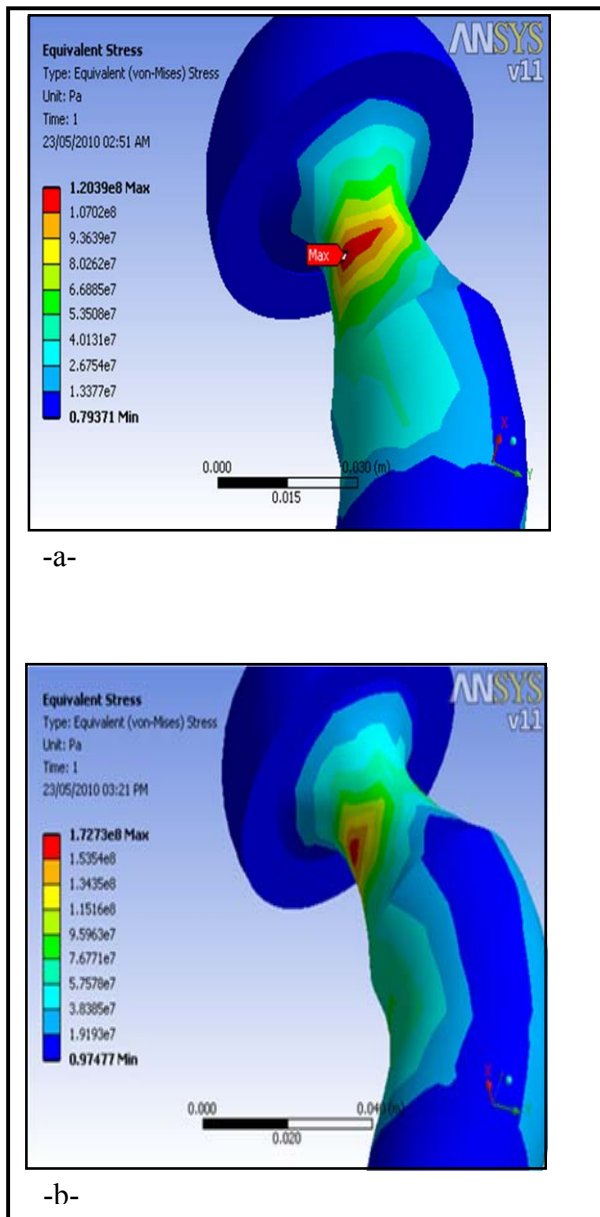


Figure (14), Von mises Stress with Changing Neck Angle. (a)- $\theta_c=35^\circ$, (b)- $\theta_c=55^\circ$

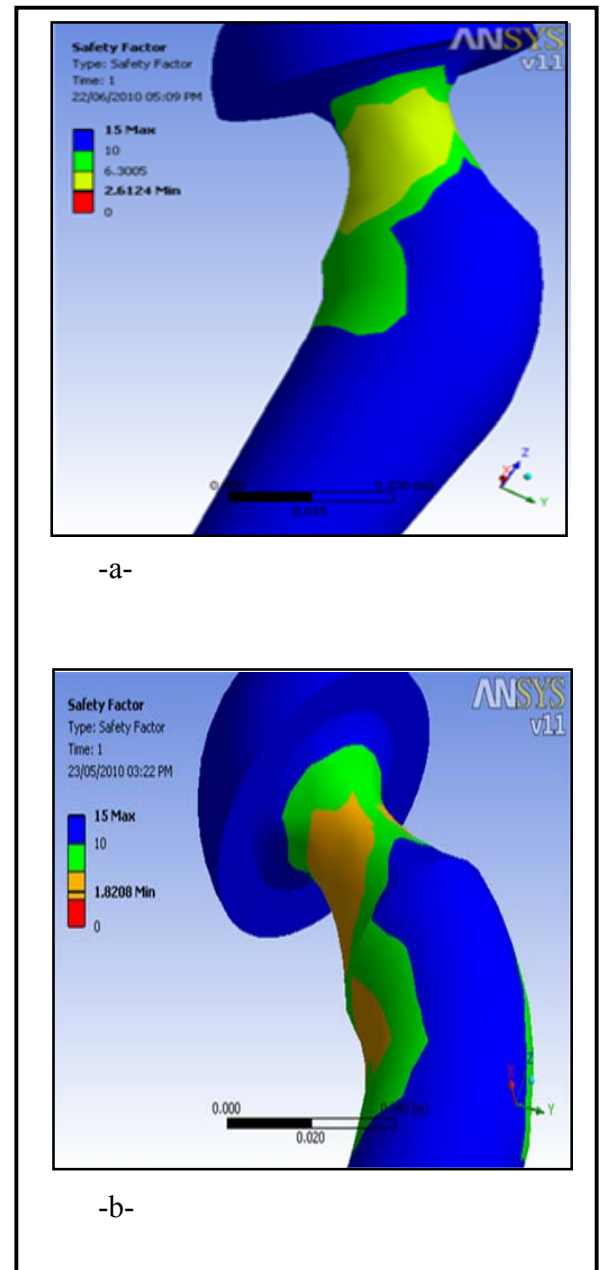


Figure (15), Safety Factor with Changing Neck angle. (a)- $\theta_c=35^\circ$, (b)- $\theta_c=55^\circ$

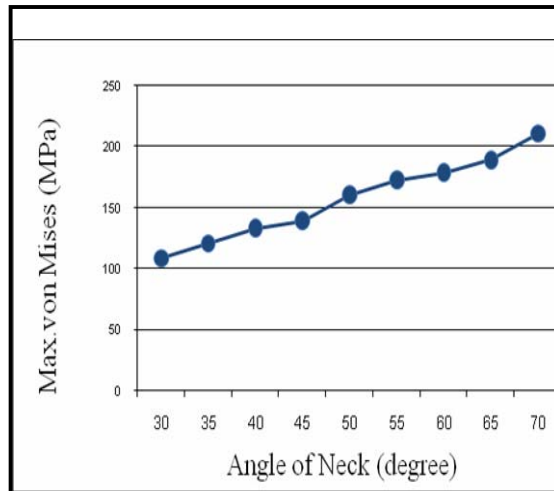


Figure (16), Variation of Max.Von mises Stress with Angle of Neck.

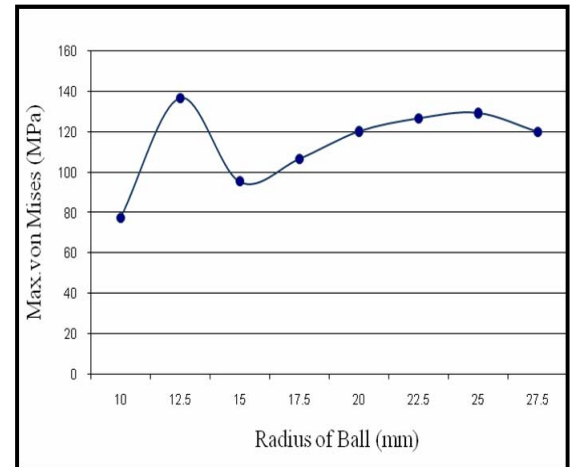


Figure (18), Variation of Max.Von mises Stress with Ball Radius.

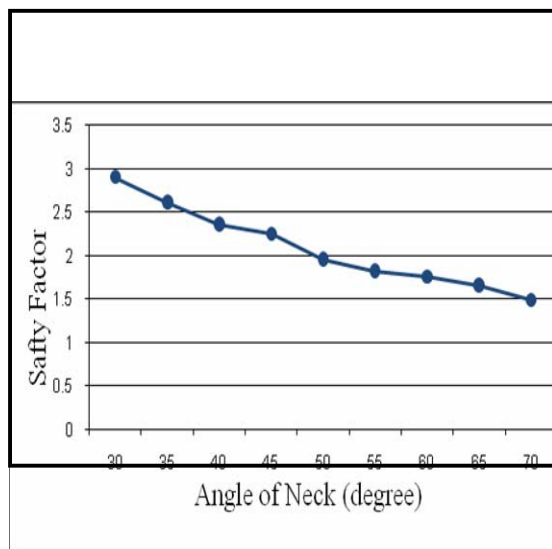


Figure (17), Variation of Min. Safety Factor with Angle of Neck.

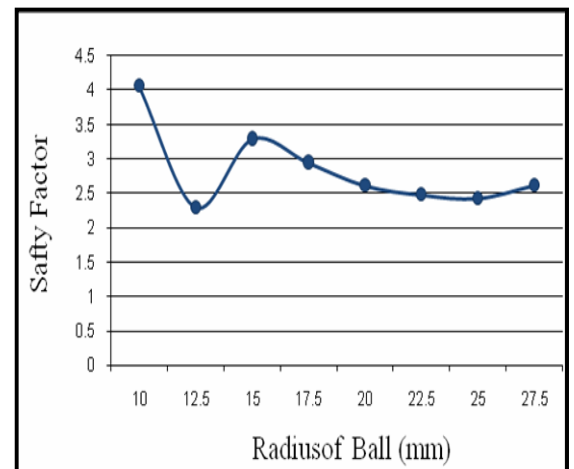


Figure (19), Variation of Min. Safety Factor with Ball

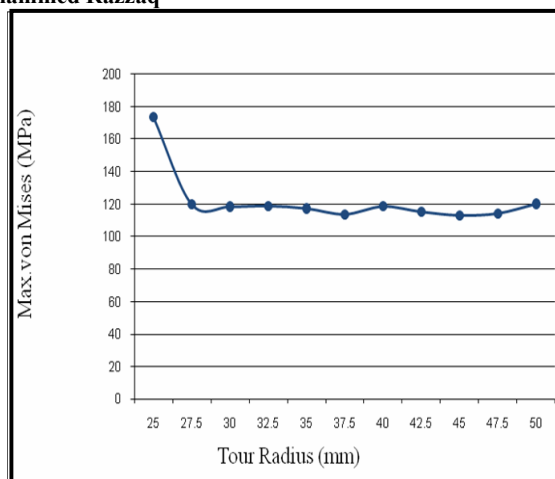
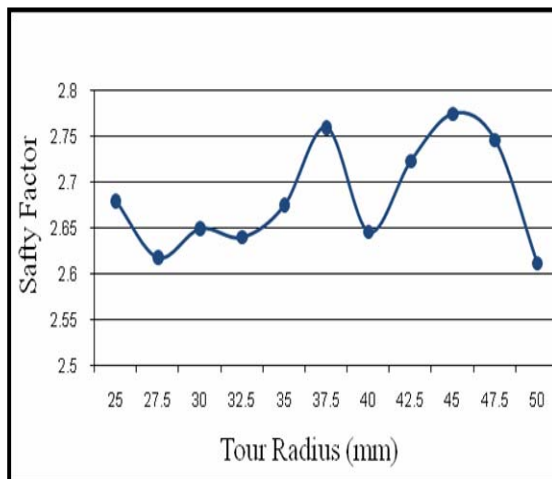


Figure (20), Variation of Max.Von mises Stress with Main Tour Radius.



Figure(21), Variation of Min. Safety Factor with Main Tour Radius.

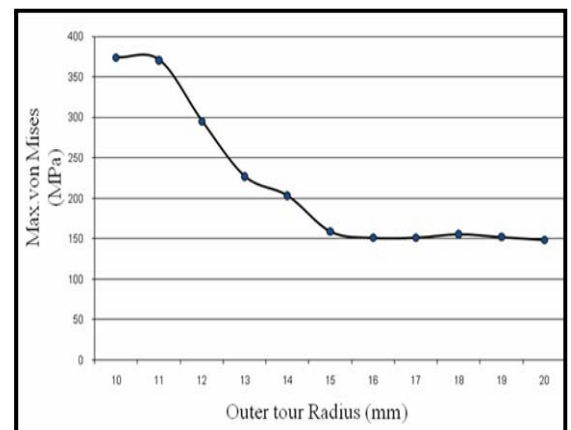
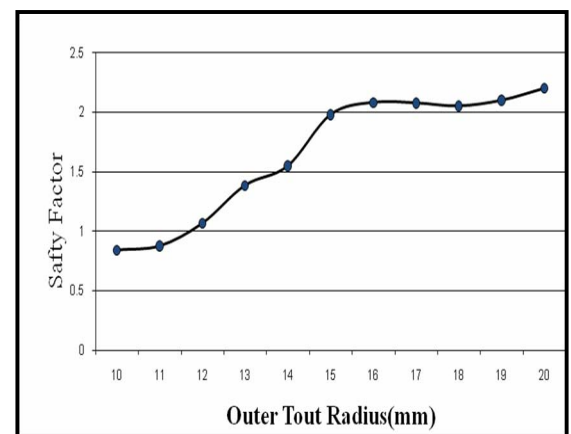
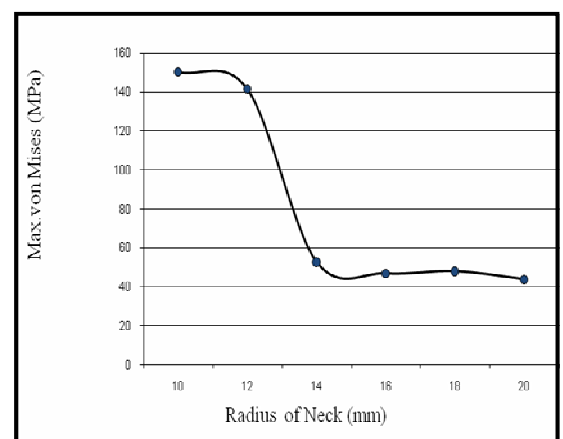


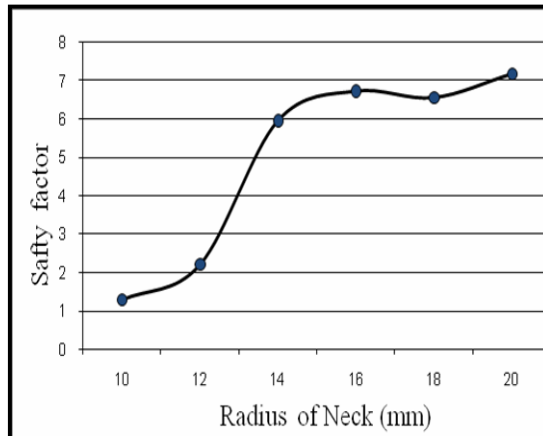
Figure (22), Variation of Max.Von mises Stress with Outer Radius of Tour.



Figure(23), Variation of Min. Safety Factor with Outer Radius of Tour.



Figure(24), Variation of Max.Von mises Stress with Neck Radius.



Figure(25), Variation of Min. Safety Factor with Neck Radius .

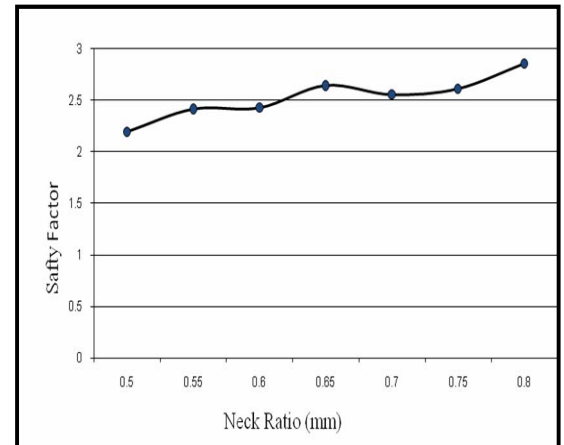


Figure (27), Variation of Min. Safety Factor with Neck Ratio.

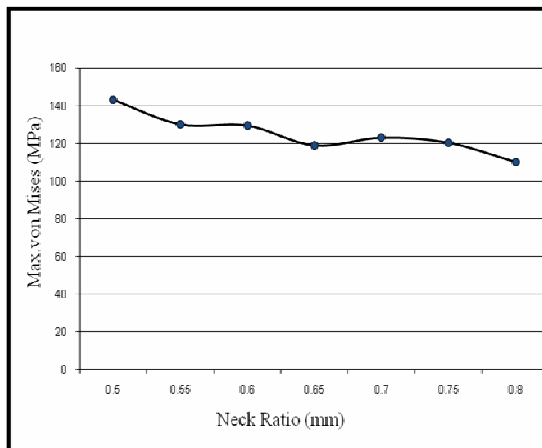


Figure (26), Variation of Max. Von mises Stress with Neck Ratio.

Experimental Study of a Biomechanical Behaviour of Rat Patellar Tendon

Dr. Fakhir S

Dr. Sadiq J. Abass

Eng. Noor Ali Sadek

College of Medicine, Al-Nahrain
University

College of Engineering,
Al-Nahrain University

College of Engineering, Al-Nahrain
University

Abstract

Tendon is important structure of the human body, since it can sustain tensile loading. The primary function of this tissue is to stabilize the joints they attached to it during daily activities. As well as, tendon has viscoelastic properties that can determine their response to loading and restrict the potential of injuries. One of the major points that this paper works with is the study of the biomechanical behaviour of tendon in response to tensile loading to describe their biological behaviour. Also, conclude the mathematical expression that may illustrate the tendon behaviour. All of the experiments were made in Physiology laboratories / Medical College/ Al- Nahrain University on ten rats "Rattus Norvegicus" of [108- 360] gm weight for in- vitro tensile test. So that 20 specimens were dissected from the rat knees, for the patellar tendons which always hydrated to prevent the tissue dryness. The results of the study, shows the behaviour of the tendon in response to tensile loading with two techniques; the dead loads technique and the continuous loads technique. The stress- strain relationships were also evaluated, as well as, the modified superposition theory was applied at different strain levels to the patellar tendon. The obtained results show that the modified superposition theory gives good results that are partly similar to the experimental results. Also, the tendon shows longer initial pattern than that for the ligament due to the presence of higher elastin content in the tendon than in the ligament.

Key words:

Patellar tendon, Biomechanical behaviour, Viscoelastic properties, Modified superposition theory.

دراسة عملية للسلوك الميكانيكي الإحيائي لوتر الجرذ الرضفي

الخلاصة

الوتر هو نوع من الأنسجة الحيوية الموجودة في جسم الإنسان يصل العضلات بالعظام ويعتبر جزء مهم من تراكيب جسم الحيوانات الثديية، من حيث قابليته على تحمل قوى الشد. الوظيفة الرئيسية لهذا النسيج هي تثبيت المفاصل التي يتصل بها خلال قيام الإنسان بنشاطاته اليومية. كذلك يملك الوتر خواصا (viscoelastic) معتمدة على الزمن كمعظم الأنسجة الحية التي تبين استجابة الوتر لتأثير القوى وكيفية تجنب حدوث الإصابات. لهذا فإن الهدف الرئيسي لهذا العمل هو دراسة الخواص الميكانيكية الإحيائية للوتر من حيث استجابة النسيج لقوى الشد وصياغة تعبير رياضي يوضح خصائص الوتر. أجريت جميع التجارب الملحة في مختبرات قسم الفلسفة في كلية الطب/ جامعة النهرين باستخدام الحيوانات المختبرية (الجرذ) الذي يتراوح وزنه (108- 360)غم، حيث شرحت 20 عينة للأوتار الرضفية من مفاصل ركب الجرذان ورطببت باستمرار أثناء إجراء التجارب لمنع جفافها. نتائج الدراسة، بينت سلوك الوتر استجابة لقوى الشد باستخدام تقنيتين؛ تقنية الأحمال الميتة وتقنية الأحمال المستمرة. كذلك علاقات الإجهاد المطاوعة قُيِّمت أيضاً، بالإضافة إلى ذلك طبقت نظرية (modified superposition) بمستويات الإجهاد المختلفة إلى نتائج الوتر الرضفي. أظهرت النتائج المحسوبة نظرياً بأن نظرية (modified superposition) تُعطي نتائج جيدة وهي مقاربة للنتائج المحسوبة عملياً.

Introduction

Tendon has similar structure to the ligament. Tendons vary in form, and can be rounded cords, strap like bands or flattened ribbons. When healthy they appear brilliant white, and have a fibroelastic texture. **Structurally**, tendon is composed of tenoblasts and tenocytes lying within a network of extracellular matrix (ECM). Tenoblasts are immature tendon cells. They are spindle-shaped, with numerous cytoplasmic organelles reflecting their high metabolic activity. As they age, tenoblasts become elongated and transform into tenocytes. These have a lower nucleus to cytoplasm ratio than tenoblasts, with decreased metabolic activity. Together, tenoblasts and tenocytes account for 90- 95% of the cellular elements of tendons. The remaining 5-10% of the cellular elements of tendons consists of chondrocytes at the bone attachment and insertion sites, synovial cells of the tendon sheath, and vascular cells, including capillary endothelial cells and smooth muscle cells of arterioles. Tenocytes synthesize collagen and all components of the ECM, and are also active in energy generation. Tenocytes and tenoblasts lie between the collagen fibres along the long axis of the tendon. The dry mass of human tendons is approximately 30% of the total tendon mass, with water accounting for the remaining 70%. Collagen type I accounts for 65-80%, and elastin accounts for approximately 2% of the dry mass of tendons as shown in fig (1) [P. Sharma and N. Maffulli, 2006]. Tightly packed tropocollagen molecules; approximately 1.5 nm in diameter, aggregate into groups of five, becoming microfibrils of approximately 3.5 nm in diameter. The microfibrils group in to subfibrils, which, in turn, aggregate to form fibrils. Fibrils are approximately 50-500 nm in diameter with a periodicity (spacing) of 64 nm. Fibres are an aggregation of fibrils and are 50-300 μ in diameter [Benno M. Nigg and Walter Herzog, 1999]. They are the smallest unit of collagen hierarchy that can be seen under light microscope. Fibers have an undulating crimp with a distance between amplitudes of about 50 μ . The crimp period can vary dramatically in different location within the ligament. Fibroblasts tend to align in rows between fiber bundles and are elongated along the long axis in the direction of normal tensile stress.

Protein also presents in ligament and tendon which is called Fibronectin; this protein contains

about 5% carbohydrate. This protein is found in small quantities in the matrix, usually in association with several other matrix component and blood vessels. Fibronectin also interacts with portions of the cell surface that are known to attach to intracellular elements, possibly forming part of an important matrix-cell feedback mechanism [Benno M. Nigg and Walter Herzog, 1999].

Water makes up about two-thirds of the weight of normal ligaments; 70 to 80% of the remaining weight is made up by the fibrillar protein collagen [Jeffrey A. Weiss and John C. Gardiner, 2001] Water can be associated with other ligament components in a variety of ways. It can be structurally bound to other matrix components. It can be bound to polar side chains, be so-called "transitional water" (loosely bound) or be freely associated with the interfibrillar gel. Most water in ligaments is freely bound or transitional. Although the exact function of water in ligaments is unknown, it appears to be crucial for at least three main reasons:

- Its interaction with the ground substance and particularly the proteoglycans influences the tissue's viscoelastic behavior.
- It seems to provide lubrication and facilitate inter-fascicular sliding.
- It carries nutrients to the fibroblasts and takes waste substances away.

A study on the effect of tissue hydration shows that the structural properties of human patellar tendon are more sensitive to time when the tissues are fully hydrated [Tammy L. Haut and Roger C. Haut, 1997]. **Elastin** is an elastic substance that is found in very small amounts in most skeletal tendons in fibular form. However, elastin fibers are about twice as common as collagen fibers. The role of elastin is probably related to recovering tendon length after stress is removed. Elastin "protects" collagen, at least at low strains [Benno M. Nigg and Walter Herzog, 1999].

Physical Properties

The physical properties of all soft connective tissues can be classified into two general categories: structural and material. The structural properties of a tendon are derived from the behaviour of a tendon-muscle complex. The material properties describe the material

irrespective of geometry. They are usually measured in the midsubstance of the tendon [Benno M. Nigg and Walter Herzog, 1999]. The load-deformation curve of all collagen-based tissues have a characteristic upwards concave shape In which the stiffness varies non-linearly with force (fig (2)). This curve consists of the regions as follows:

- Toe region: which is the initial portion of the curve, the tendon deform easily without much tensile force.
- The linear region: which is the second portion of the curve followed the toe region in which the load and deformation are approximately linearly related; the slope of this region is often used to represent the elastic stiffness of the tissue.
- Microfailure region: which is the third region of the curve followed the linear region in which sharp falls in tensile force are seen, presumably as a result of a sequential microfailure of collagen fibers.
- Failure region: which is the last region of the curve in which further loading causes the force reduces to zero as the tissue fails completely.

As the force or displacement increases, however, the tendon stiffens, providing more resistance to deformation ensures efficient load transfer from muscles to bones [C. Ross Ethier and Carig A. Simmons, 2008].

Constitutive Equations

The elastic modulus was computed from the stress- strain curve, which represent the slope of the linear part of the curve [P. P. Provenzano, 2002].

$$E = \frac{\Delta\sigma}{\Delta\varepsilon} \quad (1)$$

Where, E is the elastic modulus. σ is the measured stress and ε is the measured strain, both can be calculated by [P. P. Provenzano, 2002],

$$\sigma = \frac{F}{A} \quad (2)$$

Where, F is the measured force and A is the calculated area [P. P. Provenzano, 2002].

$$\varepsilon = \frac{\Delta l}{l_o} \quad (3)$$

Where, Δl is the measured change in length and l_o is the original length.

The constitutive model that considered in this study is the nonlinear (modified) superposition model, as it is relatively simple to calculate and has been shown to fit the stress relaxation of connective tissues well. The general form of nonlinear superposition is given by [P. P. Provenzano, 2002]:

$$\sigma(\varepsilon, t) = \int_0^t E(t - \tau, \varepsilon(\tau)) \frac{d\varepsilon(\tau)}{d\tau} d\tau \quad (4)$$

The form of the relaxation function represented by nonseparable strain-dependent power law [P. P. Provenzano, 2002]:

$$E(\varepsilon, t) = A(\varepsilon)t^{B(\varepsilon)} \quad (5)$$

The function A (ε) represents the initial modulus (E_0) that represent a constant obtained from the stress-strain curve or isochronal curve describing the nonlinear elastic behavior. The function B (ε) describes the strain-dependent rate of stress relaxation and can take the form B (ε) = g (ε) n_0 , where n_0 is some initial relaxation rate and g(ε) accounts for strain-dependent nonlinearity in relaxation rate. Substituting a Heaviside function, as described above, into eq. (4) results in [P. P. Provenzano, 2002]:

$$\sigma(\varepsilon, t) = E_0 \varepsilon t^{g(\varepsilon)n_0} = \sigma_0 t^{g(\varepsilon)n_0} \quad (6)$$

Where, E_0 and σ_0 represent isochronal values of the tangent modulus and stress, respectively, and can be functions of strain to account for nonlinearities in the elastic response.

The rate of relaxation as a function of strain for tendon shows that the tendon relaxation rate increases with increasing strain as shown in fig (3) [Sarah E. Duenwald, 2010].

Material and Method

In the experimental work, a study was made in physiology laboratories of the Medical College /Al-Nahrain University on ten rats "*Rattus Norvegicus*", patellar tendon from rats of weights ranging (108-360) gm were used as an animal tissue model for ex-vivo testing. Each rat was anesthized using fluothane inhalation anesthetic drug in a secured closed container. Patellar tendon

Carefully excised from the rat knees and all of the extraneous tissues were removed with care not to disrupt the original and insertion sites as well as the tendon itself. Specimens were kept hydrated in a physiological normal saline solution. Twenty patellar tendons were used in the experimental work. After the preparation of the specimens, all of the instruments were connected together as in fig (4). In which, the tendon from the one end was fixed with the force transducer and the other end of the tendon was fixed with the displacement transducer and both transducer were connected to the polygraph.

There were two techniques in which the loads or weights were applied in order to initiate an elongation in the specimen. The first technique, in which, dead weights of totally 290gm were used. There was a gradual addition of 10gm in the weight in each step and the polygraph would trace the changes in the specimen tension and displacement in each addition of weight as shown in fig (5). The second technique, in which, a continuous loads or weights were used as shown in fig (6). In the first technique of the dead loads, the force polygraph plots the tension and the displacement polygraph plots the displacement generated in the specimen without time consideration. But, in the second technique of the continuous loads or weights, the force polygraph plots the tension of the specimen with time and the displacement polygraph plots the displacement with time. The length of the specimen, the diameter from different sides as well as the room temperature all were measured before the experiment was done. From the diameters, the area of the specimen was measured and assumed to be elliptical. During the experiment after the connection of the specimen with the transducer, the specimen should be hydrated continuously.

Results

The results could be divided in to three parts, the first part shows the force- deformation curves of dead loads technique and continuous loads technique. The second part shows the conversion of the force- deformation curves in to stress- strain curves. Then the last part contains the application of the modified superposition method to the experimental data. The results were analyzed by using the mathematical expressions in Microsoft Office Excel program. A gradual

increase in displacement with the graduals adds on loading of 10 gm in each step for the rat patellar tendon shown in fig (7). Also, a gradual increases of tension with the graduals adds on of dead loads [10 gm for each step] of the rat patellar tendon shown in fig (8) and fig (9) shows gradual add on increases in tension and displacement with gradual loading [10gm for each step] of the rat patellar tendon, in which, an initial part of the curve contain a small part (0.4-0.9) mm called the "toe" region which followed by a more linear part (1-2.25) mm called linear region.

The average of all of the gradual increases of the tensions and displacements at gradual loading in all the experiments of the rat patellar tendons represented by smooth line which contain an initial "toe" region followed by a more linear region, the overall curve is shown in fig (10).

When continuous loads technique is used a continuous add on increases of displacement with the continuous increasing of weights which represented by smooth line for the rat patellar tendon is shown in fig (11). Fig (12) shows a gradually increased line represents the relationships between the continuous add on increases of tension with the continuous increasing of weights for the rat patellar tendon. Also, the continuous add on increases of the tension and displacement with continuous loading for the rat patellar tendon which represented by smooth line shows an initial "toe" region followed by amore linear region is shown in fig (13).

The average of all of the continuous increases of the tensions and displacements at continuous loading in all the experiments of the rat LCLs is shown in fig (14) this curve illustrate the "toe" region and the linear region.

The second part of the results shows the stress-strain curves for the rat medial collateral ligament. From the tension- deformation curve the stress-strain curve was plotted and also, it was necessary to determine the original length and the orthogonal diameters for each specimen along the experiments. From the measured diameters, the cross sectional area was calculated and assumed to be elliptical [$A=4/3(\text{base length}*\text{height})$]. When rat patellar tendon is used, the original length (measured using ordinary ruler) of the rat patellar tendons specimens ranging from [5-6.5] mm and cross sectional area of [10.5- 11.4] mm² are used

to plot the stress- strain relationship. The average of all of the stress- strain curves for the rat patellar tendons in continuous loading shown in the fig (15) which represents a smooth line with two significant regions; the initial "toe" region and the linear region .

The third part of the results was the application of the modified superposition method. One of the major reasons that the modified superposition model would be preferred among the other models was that the variables of the theory could be clearly established from the experimental results without complications. This model was applied to the experimental data at different strain levels after the elastic modulus and the relaxation rate were determined from the stress- strain curves showed previously and the equation (6) was used. The elastic modulus was determined from the slope of the linear region of the stress- strain curve in fig (15) and shown to be equal to 48.5kPa also From the fig (3) the relaxation rate was shown to be equal to -0.045, -0.0875, -0.095, -0.12 and -0.15 for the corresponding strain levels of 2%, 3.6%, 4%, 5% and 6% respectively. For each strain level the theoretical results of the modified superposition theory and the experimental results were shown in the figures from (16) to (20) in which the experimental stress was denoted by stress e and theoretical stress produced from the application of the modified superposition theory was denoted by stress MS .

Discussion

Tendon consists of two major components; which is the collagen component and the elastin component. The collagen represents the major component that resisting the tensile stress, while the elastin represents the elastic component. In this study the modified superposition theory of eq. (6) is applied to the experimental results of the rat patellar tendon in the figures from (16) to (20) and two paths are distinguished:

- ❑ Non-parallel lines shown in the first sections of these curves between the experimental results and the theoretical results.
- ❑ Parallel lines shown in the second sections of these curves between both results.

From the observation of the rat patellar tendon it is clear that the second path has behaviour similar to polymers [P. P. Provenzano, 2002], which

indicates that their structure at such strains will have a viscoelastic properties. While the first path of the curves may give an impression that it behaves more elastic the behaviour, which is not similar to polymers. This dual behaviour of the biological tissue could be explained by the following:

- ❑ In biological tissues, the combination of more than one material will give a behaviour that represents both materials. Since the tendon consist of collagen and elastin component, so that the collagen components are assumed to response to the initial state of tension, then before the elastin component are fully stretched, the collagen component will continue their stretching until the crimp is removed and the whole tissue is stretched. This speculated by the results shown in fig (15) of the rat patellar tendon, respectively. These figures illustrate a first portion that is called "toe region" which shows an elongation with little tension generated in these tissues; as the elongation increased a much tension are generated in the tendon and ligament which are shown in the second portion of the curves that is called the "linear region", which visualize the behaviour of the tensile component (collagen).
- ❑ The other explanation that describes the behavioural changes in the tendon assumes that these changes are related to their structural architectures [Nordin and Frankel, 2004], which depend on the assumption that both collagen and elastin will show their behaviour collectively.

The tendon microarchitecture visualized under light microscope showed that the proteoglycans which are arranged in the form of hinges are attached to the collagen fibers as shown in fig (21). These hinges may explain in part the initial stretching of the collagen fibers in the "toe" region of the stress- strain curves. So that when the load is applied, the tension is first generated in the collagen fibers until the coiling of the collagen fibers are removed and the fiber are stretched. After that, the tension is transmitted to the proteoglycans which have coiled arrangement, are slightly stretched and this tension is then transmitted to another collagen fiber and so on. So that, the collagen fibers are related to resisting higher tensile force more than the Elastin fibers.

Finally, the experimental results are typically succeeded to fit the applied model [modified superposition model] and show the biomechanical behaviour of the tendon.

References

Benno M. Nigg and Walter Herzog, "*Biomechanics of the musculo-skeletal system*". 2nd edition. 1999, pp. 107-117.

C. Ross Ethier and Carig A. Simmons, "*Introductory biomechanics from cell to organisms*", University of Toronto, Canada, 1st edition, 2008.

Jeffrey A. Weiss and John C. Gardiner, "*Computational Modeling of Ligament Mechanics*", Critical Reviews™ in Biomedical Engineering, 29(4), 2001, pp. 1-70.

K. Michelle quapp, "*Material characterization of human medial collateral ligament*", M.Sc. thesis, University of Utah, March 1997.

Nordin and Frankel, "*Mechanics of Muscle, Tendon, and Ligament*", McMahon, T.A , 2004, pp.148-175.

P. P. Provenzano, R. S. Lakes, D. T. Corr, and R. Vanderby Jr., "*Application of nonlinear viscoelastic models to describe ligament behavior*", Biomechan Model Mechanobiology (2002), pp.45 – 57.

P. Sharma and N. Maffulli, "*Biology of tendon injury: healing, modeling and remodeling* ", J Musculoskelet Neuronal Interact 2006; 6(2):181-190

Sarah E. Duenwald, Ray Vanderby Jr. and Roderic S. Lakes, "*Stress relaxation and recovery in tendon and ligament: Experiment and modeling*", Biorheology 47, 2010, pp.1-14.

Tammy L. Haut and Roger C. Haut , "*The state of tissue hydration determines the strain-rate-sensitive stiffness of human patellar tendon*", Journal of Biomechanics, Volume 30, Issue 1 , Pages 79-81, January 1997

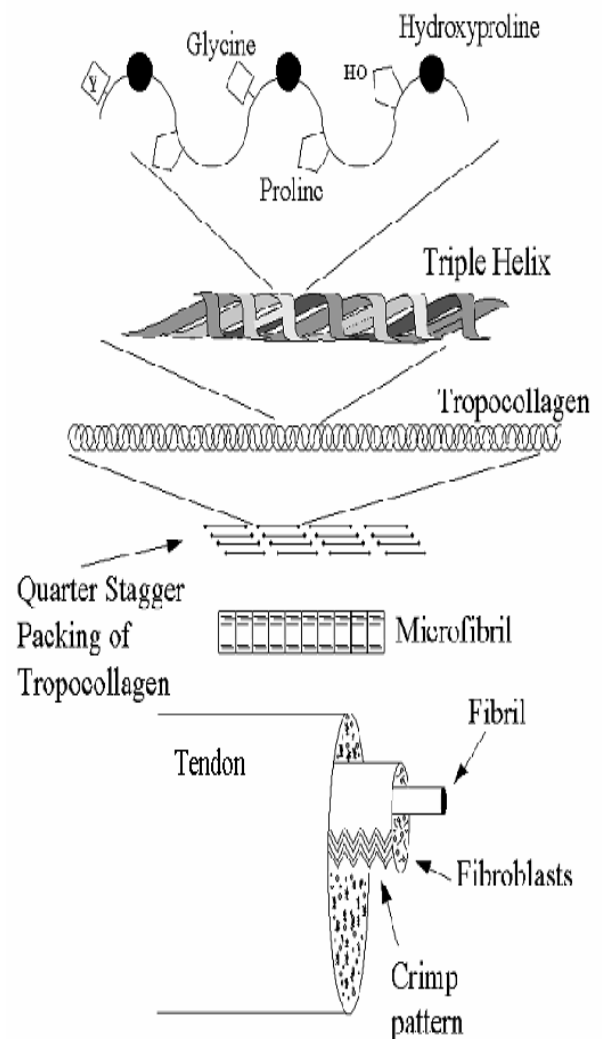


Figure (1) Schematic illustration depicting the hierarchical structure of collagen tendon midsubstance [K. Michelle quapp 1997]

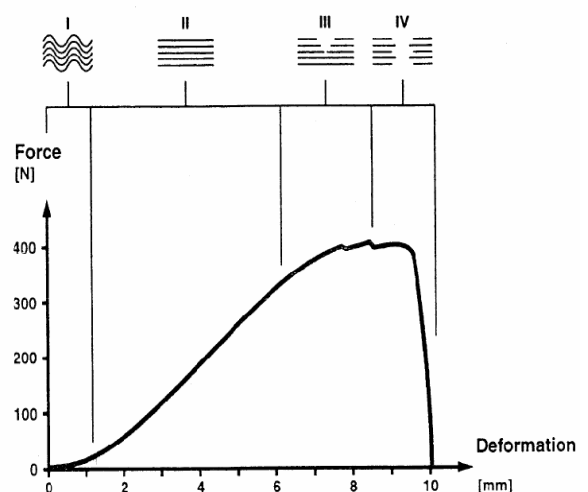


Figure (2) A typical force-deformation curve. I =toe region; II = linear region; III = region of micro- failure; IV = failure region [Benno M. Nigg and Walter Herzog, 1999]

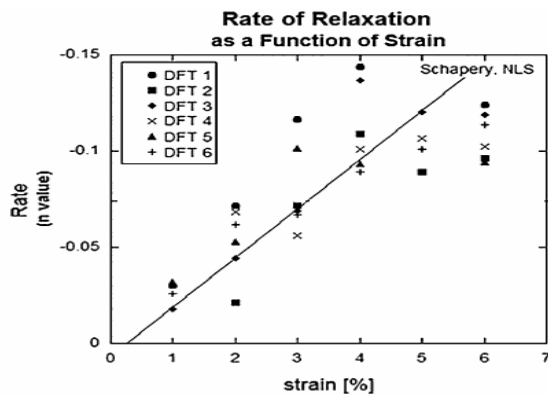


Figure (3) The Rate of Relaxation (defined as n term of power law equation, $E = At^n$) as a Function of Strain for Digital Flexor Tendon [Sarah E. Duenwald, 2010].

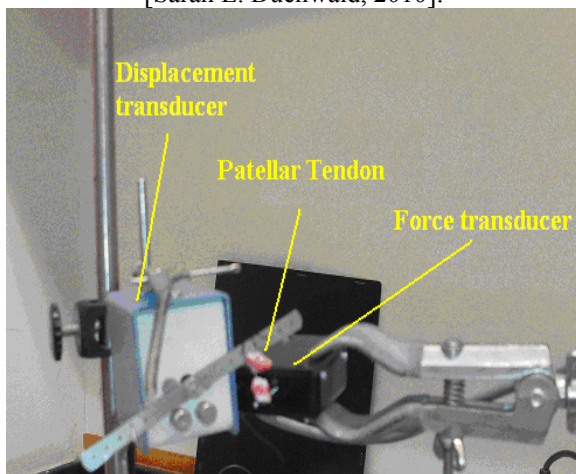


Figure (4) Connection of the patellar tendon with the force and displacement transducer.

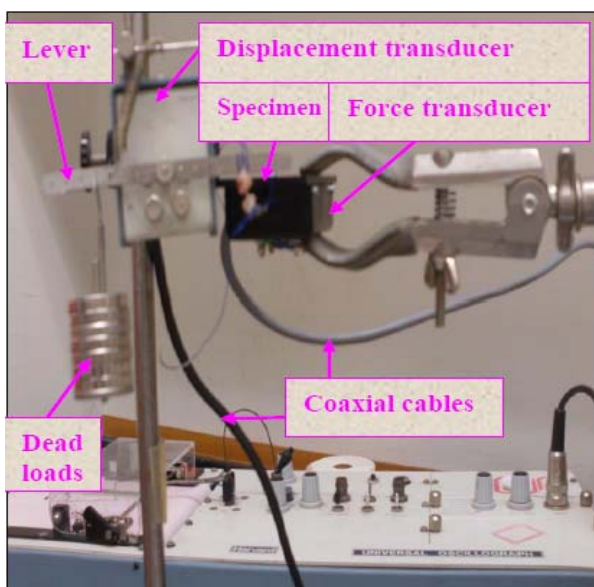


Figure (5) Dead Loads Technique.

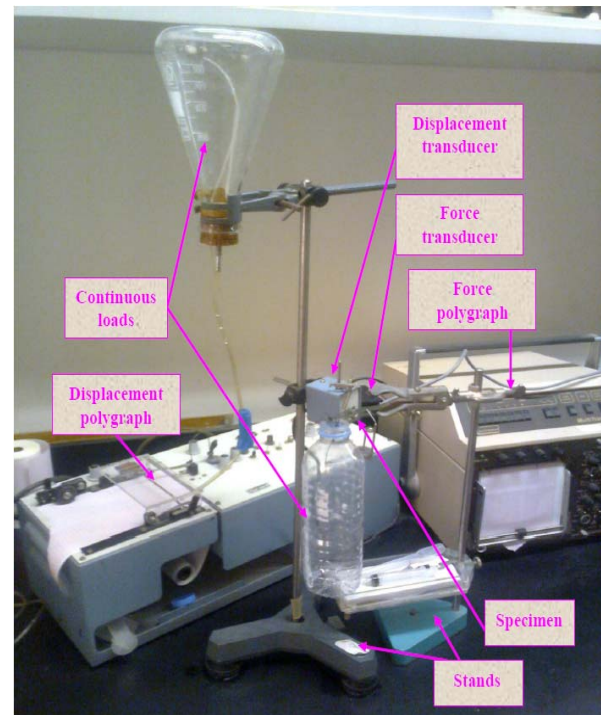


Figure (6) Continuous Loads Technique.

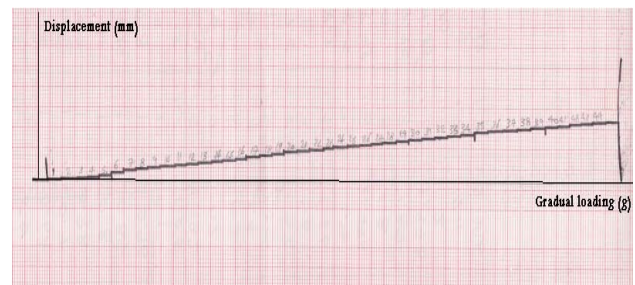


Figure (7) Raw data shows the relationships between the steps of gradual add on increases of displacement with the gradual loading by weights of the rat patellar tendon each 5mm=1mm displacement.



Figure (8) Raw data shows the relationships between the steps of gradual add on increases of tension with the gradual loading by weights of the rat patellar tendon [each 4mm=10gm of tension]

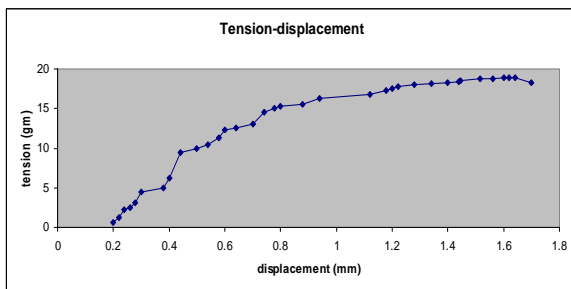


Figure (9) The gradual add on increases of the tension and displacement with gradual loading for one rat patellar tendon.

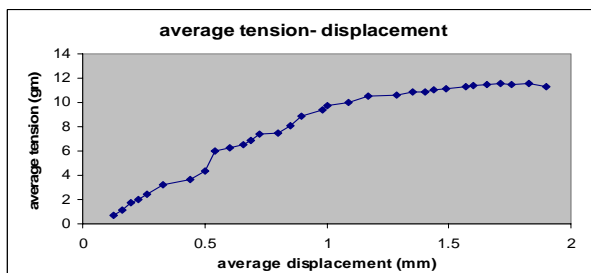


Figure (10) The average of all of the gradual increases of the tensions and displacements at gradual loading in all the experiments of the rat patellar tendons.

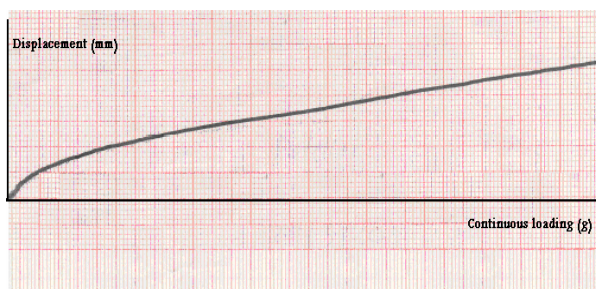


Figure (11) Raw data shows the relationships between the continuous add on increases of displacement with the continuous loading by weights of the rat patellar tendon [each 5mm on the curve =1mm of displacement].

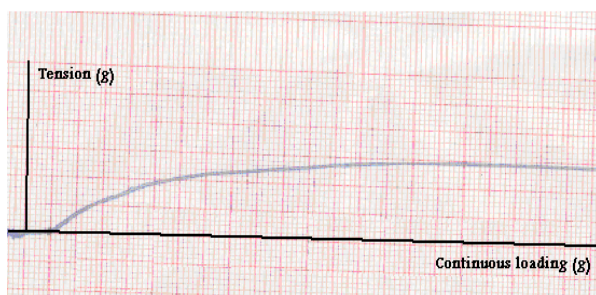


Figure (12) Raw data shows the relationships between the steps of continuous add on increases of tension with the continuous loading by weights for the rat patellar tendon [each 4mm on the curve = 10gm of tension].

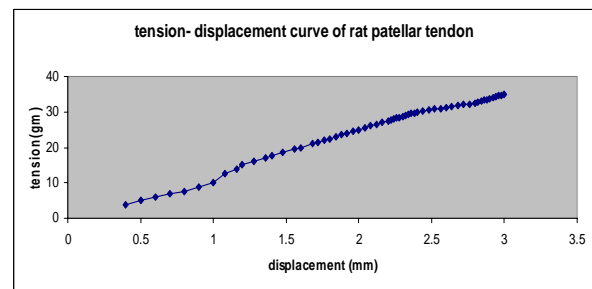


Figure (13) The continuous add on increases of the tension and displacement with continuous loading for one rat patellar tendon.

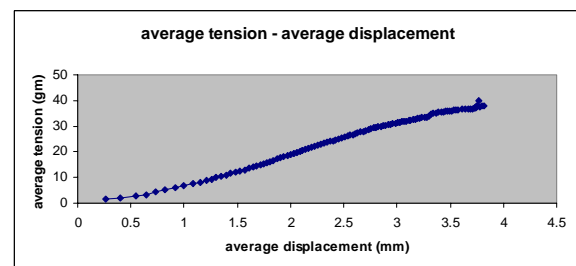


Figure (14) The average of all of the continuous increases of the tensions and displacements at continuous loading in all the experiments of the rat patellar tendons.

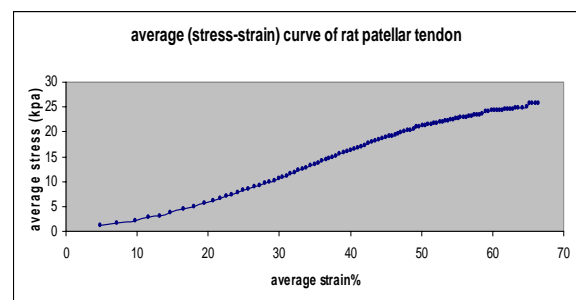


Figure (15) Average stress-strain curve for rat patellar tendons under continuous loading.

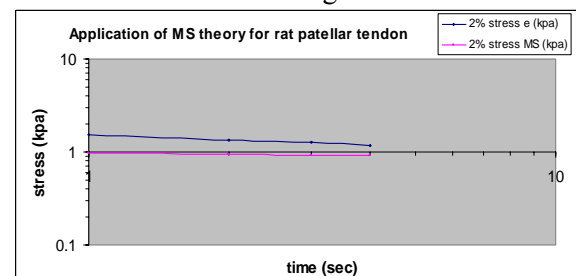


Figure (16) Application of the modified superposition theory to the rat patellar tendon at strain level of 2%. The blue line represented the experimental results and the pink line represented the theoretical results.

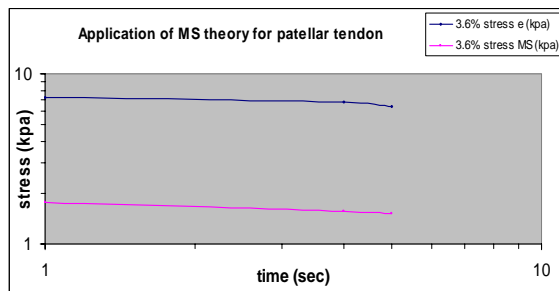


Figure (17) Application of the modified superposition theory to the rat patellar tendon at strain level of 3.6%. The blue line represented the experimental results and the pink line represented the theoretical results.

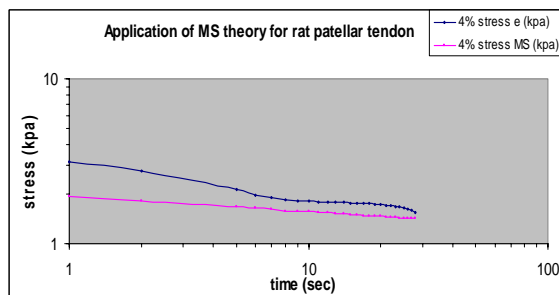


Figure (18) Application of the modified superposition theory to the rat patellar tendon at strain level of 4%. The blue line represented the experimental results and the pink line represented the theoretical results.

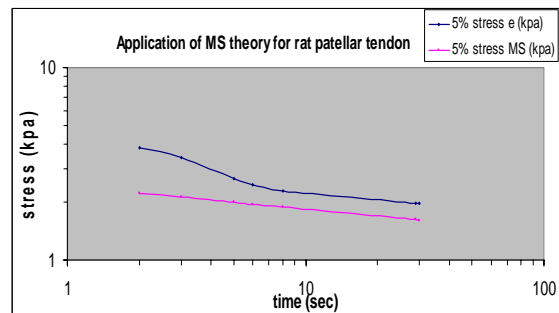


Figure (19) Application of the modified superposition theory to the rat patellar tendon at strain level of 5%. The blue line represented the experimental results and the pink line represented the theoretical results.

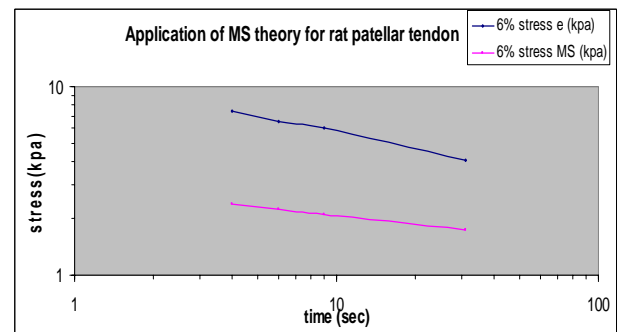


Figure (20) Application of the modified superposition theory to the rat patellar tendon at strain level of 6%. The blue line represented the experimental results and the pink line represented the theoretical results.

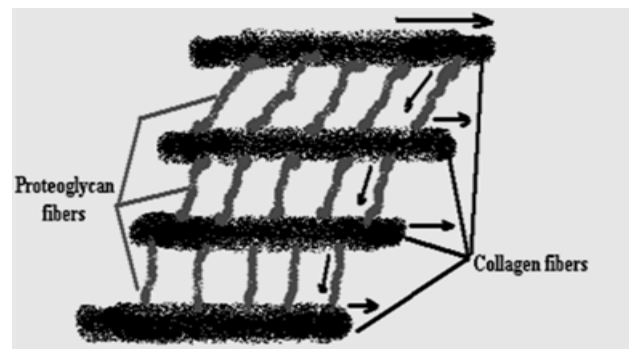


Figure (21) Illustration of collagen interaction with Proteoglycan.



Investigation Parameters of Resistance Spot Welding For AA1050 Aluminum Alloy Sheets

Kasim Mohammed Daws
Professor
Mechanical Engineering Department
Baghdad University
Kasim_daws@yahoo.com

Moneer Hammed Al-Saadi
Assistance Professor
Welding Department
Technical College-Baghdad
monerht@yahoo.com

Ihsan Kadhom Abbas Al-Naimi
Assistance Lecturer
Mechanical Engineering Department
Baghdad University
Ihsan_kad@yahoo.com

Abstract

The parameters of resistance spot welding (RSW) performed on low strength commercial aluminum sheets are investigated experimentally, the performance requirements and weldability issues were driven the choice of a specific aluminum alloy that was AA1050. RSW aluminum alloys has a major problem of inconsistent quality from weld to weld comparing with welding steel alloys sheet, due to the higher thermal conductivity, higher thermal expansion, narrow plastic temperature range, and lower electrical resistivity. Much effort has been devoted to the study of describing the relation between the parameters of the process (welding current, welding time, and electrode force) and weld strength. Shear-tensile strength tests were performed to indicate the weld quality. A weld lobe diagrams were constructed to evaluate the weldability of three sheet thicknesses of this alloy. Most appropriate welding time and electrode force are 5 cycles and 1.75-2.25 kN respectively. The ranges of the weldability are 14-28, 18-30, and 22-32 kA for 0.6, 1.0, and 1.5 mm sheet thicknesses respectively. A statistical regression analysis was used to demonstrate the relationship of the process parameters and the strength of the weldments. Two empirical equations for each thickness were proposed to estimate the shear tensile strength of the weldments, one for quadratic and the other linear relationship between the process parameters and the strength. There are no significant differences between the equations when applied to the available data.

Keywords: Commercial Aluminum alloys RSW Welding Parameters

Regression Analysis

AA1050

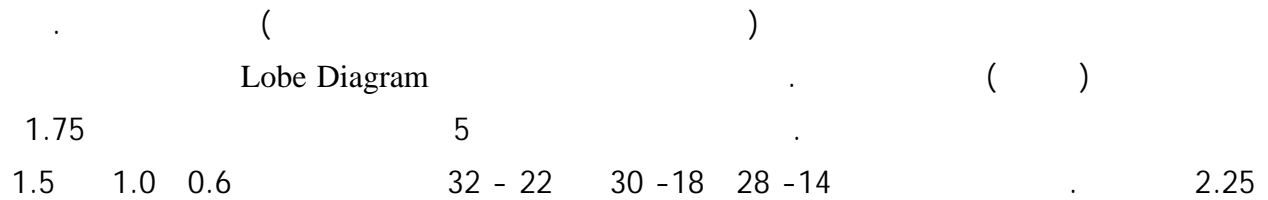
إحسان كاظم عباس النعيمي

أ.م. د منير حميد ظلفيح السعدي

أ. د قاسم محمد دوس العتابي

:

.AA1050



:

سبائك الالمنيوم التجارية

لحام مقاومة النقطة

متغيرات اللحام

تحليل الانحدار



Introduction

RSW has been the dominant process in sheet metal joining, particularly in automobile industry in spite of consumer goods. Modern small vehicles contain (2000-5000) spot welds [Chao 2003]; therefore, each welded spot has its own importance not only with regard to quality but also for production issue. Automobiles manufacturers trend to make lighter vehicles with intensive use of aluminum in order to reduce fuel consumption and CO₂ emission.

A better understanding of aluminum spot welding processes has become necessary. Steel and aluminum alloys share many of the same process attributes for RSW. However, the productivity of aluminum spot welding is lower than of steel especially those alloys with low strength (series 1xxx), This is because aluminum alloys have higher thermal and electrical conductivity, higher coefficient of expansion, narrow plastic temperature range, and oxide film problems which forms on the surface of the aluminum and has high electrical resistance and a high melting temperature (2050°C), as the oxide film grows the effective contact resistance of the aluminum changes. Therefore, the control of weld quality is much more difficult and requires tighter controls [Kim and et. al 2009].

In general, aluminum's high thermal and electrical conductivity require higher current, shorter weld time, about (2-3) times the amount of current and ¼ weld time compared to spot welding steel. Accurate control and synchronization of current and electrode force is required due to the narrow plastic temperature range [RWMA 2003].

Most of the previous researches on aluminum RSW were concentrated on the high strength aluminum alloys such as series (2xxx), (5xxx), (6xxx), and (7xxx), since these alloys are less difficult of RSW than those low strength alloy series (1xxx), and definitely by manufacturer demand, but the required for low price product and higher resistance of corrosion will increase the demand on aluminum alloys series (1xxx) especially in sheet metal products.

Weld lobe diagrams are usually developed in a lap environment with nominal process setting and then extended to production. It is a graph indicating the evaluation on RSW weldability that shows the appropriate welding range by changing two factors with fixing one factor among three factors of RSW such as electrode force, weld time, and weld current

[Cho and et.al. 2006]. In this work, the lobe diagram of weld current-weld time was used, with fixing the electrode force. The left boundary line of the lobe diagram was decided by low limit tensile strength of the welded thin aluminum sheet, and the right boundary line was decided where expulsion occurred [Zhang and Senkara 2006].

Expulsion, which can be observed frequently during RSW, happens at either the faying surfaces or the electrode/work piece interfaces. The latter may severely affect surface quality and electrode life, but not the strength of the weld if it is limited to the surface. The risk of expulsion is especially high in spot welding of aluminum alloys due to the very dynamic and unstable character of the process, relating to the application of a high current in a short welding time as compared to welding steels. Expulsions usually occur at the later stage of welding, as a nugget needs time to grow to a certain size. However, observations have shown that expulsion may also happen at early stages of welding when the size of the molten metal is considerably smaller than that of the compressive force supplied by the electrodes.

Expulsion in welding is determined by many factors involving electrical, thermal, metallurgical, and mechanical processes. Although there are many complicated causes of expulsion, its basic process can be described by the interaction between the forces from the liquid nugget and its surrounding solid containment. Based on this understanding, a general model of expulsion is proposed. The criterion can be stated as: Expulsion occurs when the force from the liquid nugget onto the solid containment equals or exceeds the effective electrode force [Senkara, Zhang, and Hu, 2004].

In this work, the relationship of RSW parameters and the quality of weld represented by shear-tensile test of aluminum welds were developed by using the charts indicating this relationship and the multiple power regressions using linear and quadratic model to construct mathematical empirical equations in order to estimate the strength of welds depending on the process parameter as an input values.

Experimental Procedure

The experiments were performed at Technical University of Denmark (DTU), using 0.6, 1.0, and 1.5 mm sheet thicknesses of low strength aluminum alloy AA1050 on a TECNA 8106 AC spot welding machine, the specifications of the welder are listed in **Table 1**. The Controller of the welder type is TE-180 with 16 functions.

The electrodes used during the experiments were type A0 according to ISO 5821-2009. They were made of Zirconium copper alloy (Cu Cr Zr) with the following chemical composition Cr 0.7-1.2%, Zr 0.06-0.15%, and the reminder Cu.

The configuration of electrodes is radius, 16 mm diameter with a spherical end surface of 40 mm radius. Welding current measured by a Rogowski coil together with TECNA-1430 conditioner instrument and a piezoelectric force sensor with Kistler type 5015 transducer for measuring the electrode force. And both these instruments connected to the Electrostatic Sensitive Connectors National Instruments model BNC-2110.

A LabVIEW version 8.6 software program from national Instruments was used to calculate the RMS of current and voltage, and the electrode force during welding. The properties and nominal compositions (performed by spectrum analyzer) of the sheets are shown in **Table 2**, the samples were cut from the sheets into 16 × 115 mm, the rolling direction with the longitudinal dimension and they joined as lap joining as shown in **Fig. 1**, to prepare the shear-tensile tests. A hard wood fixture was used to fix the samples in a good alignment with electrodes of welder.

The strength of weldments was performed in lap shear-tensile test on a 100 kN AMSLER universal testing machine. The effect of RMS current I (A), welding time C (cycle), and the electrode force P (kN) on the weld strength S (N) were investigated and evaluated. There were not used up/down-slope of the current and electrode force in all experiments. The experiments were designed as a general factorial with three replicates per condition. The factors and their associated values are given in **Table 3**.

Fig. 2 shows the macro/micrographs of the welding strips of 1.0 mm thick which was welded with 29 kA and 5 cycles. The nugget seems clearly with suitable size due to the sufficient welding parameters.

Results and Discussion

Lobe Diagram

A lobe diagram is a two dimension graphical representation of ranges of welding parameters for a specific material and its thickness to compare and evaluate the weldability and has been used for many years. The weldability of a material in RSW is determined by two main factors. Firstly, the width of the lobe curve, which shows the permissible weld current range at a constant weld time and secondly the wear of the electrodes [Kim and Eagar 1988].

The allowed welding range is obtained by fixing one parameter and changing two remaining parameters among electrode force, weld time and weld current. In this study, weld current-weld time has been used to represent the welding lobe, with fixing electrode force. The horizontal and vertical axes were set to weld current and weld time respectively. The value of the preselected electrode force was not originally planned, but during the experiments was performed, and it was selected about 2 kN, since this force give more weldability of the soft aluminum alloy than the other three values which were used in this work.

The width of lobe diagram depends on many variables such as weld current, weld time, electrode force, thickness of the sheet, and electrode shapes, but the dominant influence of the lobe width is the material properties and the surface contaminations of the sheets.

The oxide film is a dominant factor affects the weldability especially when welding aluminum sheets, since it causes many problems due to its high electrical resistance, high melting point (2050°C), and tenacious non-uniform nature of breaking during spot welding. Thereby it is difficult to construct the same lobe diagram for the same aluminum alloy and the same sheet thickness even though it selects the same welding parameters due to the largely variations of the oxide film growth.

Fig. 3 shows the weld lobe diagram as mentioned above with three sheet thicknesses. The lower limit (left line) of the diagram had been set to 435, 725, and 1100 kN for 0.6, 1.0, and 1.5 mm sheet thicknesses respectively. These values were calculated as the minimum shear tensile strength required for acceptable welding strength. On the contrast, the upper limit (right line) was decided by whether an expulsion (splash) occurred or not [Kim and Eagar 1988].

The wider area of all lobe diagrams located nearly at 5 cycles as welding time and showing good agreement across the investigated aluminum alloys which required minimum welding time, since any increasing of welding time cause expulsion and more distortions in the sheets because of the amount of excess heat generated.

The differences of the weldability between the thicknesses of the sheets as showing in lobe diagrams do not look much as it was expected and this is due the probability that all sheets have the same thickness of the oxide layer being of the same batch production.

The ranges of the appropriate welding condition are 28-14 (14), 30-18 (12), and 32-22 (10) kA of 0.6, 1.0 and 1.5 mm sheet thicknesses respectively. So, this could be conclude that the relationship between the weldability and thickness of sheets of this type of alloys as an inverse relationship. And the reasons that increasing the volume of the strip and surface area means more heat dissipated due to the thermal properties of the metal, in addition of more expulsions occur.

Weld Strength

RSW involves complicated interaction between the physical and metallurgical properties of the materials and electromagnetic and mechanical phenomena of the process. In this work, much effort has been devoted to the study of describing the welding parameters and the weldability of the soft aluminum alloy to obtain good weld qualities and in the same time improve the production stability without severe expulsion while maintaining a longer lifetime of electrodes. This will need not only better understanding of the weldability of the materials, but also more optimization of the welding process parameters which will need numerous welding experiments and destructive tests.

Shear tensile tests were done on the welding strips to demonstrate the strength of the welding quality and finding the relationship between the parameters of the RSW process and the strength. **Fig. 4, Fig.5, and Fig.6** show the effect of the welding current (percentage of the machine) and welding time (cycles) on the shear tensile force (N) for the 0.6, 1.0, and 1.5 mm sheet thicknesses, while the pressure was fixed of the pneumatic system of the welder at 1/8 bar which is nearly to the (1.75-2.25) kN electrode force, since the electrode force measured and calculated dynamically by the force sensor and the assistance of the LabVIEW program.

The charts confirm that increasing the welding time will decrease the shear tensile force due to the expulsions occur at these stages, and there are optimum values of welding current for each thickness. The small amount of the current density will form insufficient nugget size and the large amount of the current density will expulsion occur causing decrease of the electrode life. The relationship between the shear tensile strength and the parameters of the RSW process with three sheet thicknesses is shown in **Fig. 7**, and it is quite natural that the high values of shear tensile force exist with a thickness of 1.5 mm because of the large size of the nugget that bear higher load than the smaller nugget.

For the purpose of giving a clear picture of the process and their parameters, other experiments were performed by increasing the electrode pressure to the 1/4 bar (2.25-3.00 kN), 1/2 bar (3.00-3.50 kN), and 3/4 bar (3.50-4.00 kN). The charts of the influence of increasing the electrode force on the relationship between the RSW process parameters and their strength were shown in **Fig. 8**. The electrode force is the critical factor that influences the weldability.

There are a number of important observations by studying the charts, can summarize by the following:

- Sheet 1.5 mm
 - i. The best strength of the welding had performed at 2.25-3.00 kN electrode force, and 22-27 kA welding current.
 - ii. At lower electrode force (1.75-2.25) kN, it is required a large welding current value more than 27 kA to form the same nugget

- iii. Size, since the contact resistance will be increased as the electrode force decreases.
- iv. The best welding time is 9 cycles for all electrode force values. But there is a strange observation of a lower strength of the weldments at the time of 7 cycles even with all electrode force values. Probably this case occurred because of the critical value of heat dissipated related with size of the welding strips.
- Sheet 1.0 mm
 - i. The behavior of the relationship between the welding strength and the parameters of the RSW process nearly as same as the sheet of 1.5 mm.
 - ii. The best welding time is 5 cycles.
- Sheet 0.6 mm
 - i. Better welding strength was occurred at the lower electrode force.
 - ii. The best welding time is 2 cycle.

Generally, increasing electrode force will be decrease the welding strength for the soft aluminum alloys. Moreover, it will be decrease the welding range, and increase the separation of the strips, in addition of increasing the internal stresses that cause the indentation of the cracks at the nugget and the heat affected zone (HAZ).

Regression Analysis

Since there are a little published paper investigated the RSW relevance with a low strength commercial aluminum alloys and based on the experimental of this work, empirical equations were proposed to calculate the minimum shear tensile strength for a specific of the aluminum alloy AA1050.

There were several attempts to find the best proposed equations to estimate the welding strength. One of this attempt was three order power equation, but most of the proposed equations were inaccurate, therefore the focus was only on the below equations. The following equations are proposed for estimating the shear-tensile strength of the RSW process, one for a quadratic relationship (eq. 1) and the other for a linear relationship (eq. 2).

These equations were constructed from the available data of this experimental work using the

LabVIEW software program to calculate the RMS of current (I) and voltage, welding time (C), and the electrode force (P) during welding and the tests performed of the shear-tensile strength (F) to the weldment strips, and assistance with numerical solution in curve fitting which are demonstrated in the appendix.

$$F = a_0 + a_1 I^2 + a_2 I + a_3 C + a_4 P \quad (1)$$

$$F = a_0 + a_1 I + a_2 C + a_3 P \quad (2)$$

And the solutions of the above constants (a's) for each thickness are;

Sheet 0.6 mm:

$$F = 7 - 0.4I^2 + 54I - 17C - 144 \quad (3)$$

$$F = 169 + 36.5I - 17C - 145P \quad (4)$$

Sheet 1.0 mm:

$$F = 252 + 0.2I^2 + 48I - 10C - 264P \quad (5)$$

$$F = 183 + 54I - 10C - 264P \quad (6)$$

Sheet 1.5 mm:

$$F = -2425 - 0.3I^2 + 240I + 8C - 265P \quad (7)$$

$$F = -980 + 113I + 7.3C - 260P \quad (8)$$



When implementation the above empirical equations on the data of the experiments of this work was noted the absence of a large difference between linear equations and the quadratic equations. So, it will be suggest applying the linear equations because they are easier and will be quite sufficient to estimate the values of the welding strength.

Conclusions

It is important to know and evaluate the influence of the RSW process parameters on the welding strength especially where welding low strength of aluminum alloys since these alloys are very difficult to resistance welding due to the high thermal conductivity, low electrical resistance, the oxide film problems, and the low strength.

The most important conclusions can be summarized as follows;

1. The differences of the weldability between the thicknesses of the sheets were little, and the range of the weldability are 14, 12, 10 kA for the 0.6, 1.0, and 1.5 mm sheet thickness respectively. So, it shows inverse relation between the weldability range and the sheet thickness of a specific this alloy.
2. The best welding times are 2, 5, and 9 cycles for the 0.6, 1.0, and 1.5 mm sheet thickness respectively.
3. The range of the appropriate welding condition is large in the 5 cycles of a welding time.
4. Resistance spot weldability of AA1050 aluminum alloy is influenced greatly by the electrode force. When a lower electrode force is applied, the acceptable current range is the widest. The best amount of the electrode force is (1.75-2.25) kN.
5. The proposed empirical equation with linear relationship is quite enough to estimate the strength of the weldments.

Acknowledgement

This work is part of the cooperation between Baghdad University and Technical University of Denmark (DTU) for independent research. The authors would like to thank Department of

Mechanical Engineering at DTU, especially Professor Dr. Niels Bay and special thanks to Peter Sanderhoff, Lars Holmbaek, and Ph.D Chris V. Nielsen, for helping with all practical work, ordering and cutting out strips.

References

- Chao, Y. J. (2003), "Ultimate Strength and Failure Mechanism of RSW Subjected to Tensile, Shear, and combined tensile/Shear Loads", ASME, Journal of Engineering Materials and Technology, Vol. 125, 125-13.
- Cho, W., Li, and Hu (2006), "Design of Experiment Analysis and Weld Lobe Estimation for Aluminum Resistance Spot Welding", Supplement to the Welding Journal, sponsored by the American Welding Society and the Welding Research Council.
- Kim, D. C., Park, H. J., Hwang, I. S., Kang, M. J. (2009), "RSW of Aluminum alloy sheet 5J32 Using SCR type and Inverter Type Power Supplies", International Scientific Journal, Vol. 38, Issue 1, Pages 55-60.
- Kim, E. W., Eagar, T. W. (1988), "Parametric Analysis of Resistance Spot Welding Lobe Curve", International Congress and Exposition, Detroit Michigan, USA, SAE Technical Paper, Series No. 880278.
- RWMA (2003), "Resistance Welding Process, Resistance Welding Manuals", printed by George H. Buchman, Bridgeport, Nj USA.
- Senkara, J., Zhang, H., and Hu, S. J. (2004), "Expulsion Prediction in Resistance Spot Welding", Welding Research, Welding Journal, pp. 123-132.
- Zhang, H., Senkara, J. (2006), "Resistance Welding, Fundamental and Applications", Book published by CRC press, Taylor & Francis Group LLC.

Appendix

Multiple power regressions for the variables of shear tensile strength parameters;

$$f(F, I, C, P) = 0 \quad (A1)$$

Where:

F: Shear tensile strength in (N)

I: Welding current in (kA)

C: Welding time in (Cycles)

P: Electrode force (kN)

$$F \propto I, C, P \quad (A2)$$

$$F = f(I, C, P) \quad (A3)$$

Modified eq. (11) for the power relationship related variables, therefore:

$$F = a_0 + a_1 I^2 + a_2 I + a_3 C + a_4 P \quad (A4)$$

Or:

$$F = a_0 + \sum_{i=1}^n a_i x_i \quad (A5)$$

The best values of a's are determined by setting up the sum of squares of residual error.

$$Sr = \sum (F_i - a_0 - a_1 I_i^2 - a_2 I_i - a_3 C_i - a_4 P_i)^2 = Min. \quad (A6)$$

$$\frac{\partial Sr}{\partial a_0} = -2 \sum (F_i - a_0 - a_1 I_i^2 - a_2 I_i - a_3 C_i - a_4 P_i) = 0 \quad (A7)$$

$$\frac{\partial Sr}{\partial a_1} = -2 \sum [(F_i - a_0 - a_1 I_i^2 - a_2 I_i - a_3 C_i - a_4 P_i) I_i^2] = 0 \quad (A8)$$

$$\frac{\partial Sr}{\partial a_2} = -2 \sum [(F_i - a_0 - a_1 I_i^2 - a_2 I_i - a_3 C_i - a_4 P_i) I_i] = 0 \quad (A9)$$

$$\frac{\partial Sr}{\partial a_3} = -2 \sum [(F_i - a_0 - a_1 I_i^2 - a_2 I_i - a_3 C_i - a_4 P_i) C_i] = 0 \quad (A10)$$

$$\frac{\partial Sr}{\partial a_4} = -2 \sum [(F_i - a_0 - a_1 I_i^2 - a_2 I_i - a_3 C_i - a_4 P_i) P_i] = 0 \quad (A11)$$

Alternatively:

$$n a_0 + \sum a_1 I_i^2 + \sum a_2 I_i + \sum a_3 C_i + \sum a_4 P_i = \sum F_i \quad (A12)$$

$$\sum a_0 I_i^2 + \sum a_1 I_i^4 + \sum a_2 I_i^3 + \sum a_3 C_i I_i^2 + \sum a_4 P_i I_i^2 = \sum F_i I_i^2 \quad (A13)$$

$$\sum a_0 I_i + \sum a_1 I_i^3 + \sum a_2 I_i^2 + \sum a_3 C_i I_i + \sum a_4 P_i I_i = \sum F_i I_i \quad (A14)$$

$$\sum a_0 C_i + \sum a_1 I_i^2 C_i + \sum a_2 I_i C_i + \sum a_3 C_i^2 + \sum a_4 P_i C_i = \sum F_i C_i \quad (A15)$$

$$\sum a_0 P_i + \sum a_1 I_i^2 P_i + \sum a_2 I_i P_i + \sum a_3 C_i P_i + \sum a_4 P_i^2 = \sum F_i P_i \quad (A16)$$

In matrix form:

$$[A] \bar{a} = \bar{b} \quad (A17)$$

And the matrix to find (a's) is;

$$[A] = \begin{bmatrix} n & \sum I_i^2 & \sum I_i & \sum C_i & \sum P_i \\ \sum I_i^2 & \sum I_i^4 & \sum I_i^3 & \sum C_i I_i^2 & \sum P_i I_i^2 \\ \sum I_i & \sum I_i^3 & \sum I_i^2 & \sum C_i I_i & \sum P_i I_i \\ \sum C_i & \sum I_i^2 C_i & \sum I_i C_i & \sum C_i^2 & \sum P_i C_i \\ \sum P_i & \sum I_i^2 P_i & \sum I_i P_i & \sum C_i P_i & \sum P_i^2 \end{bmatrix}$$

Where n is the repeated experimental test.



To resolve the matrix to find (a's) values multiple by $[A]^{-1}$

$$F = a_0 + a_1 I_i + a_2 C_i + a_3 P_i \quad (A19)$$

$$[A]^{-1} [A] \bar{a} = [A]^{-1} \bar{b} \quad (A18)$$

And the matrix to find (a's) is

Where:

$$\bar{a} = \begin{pmatrix} a_0 \\ a_1 \\ a_2 \\ a_3 \\ a_4 \end{pmatrix} \quad \& \quad \bar{b} = \begin{pmatrix} \sum F_i \\ \sum F_i I_i^2 \\ \sum F_i I_i \\ \sum F_i C_i \\ \sum F_i P_i \end{pmatrix} \quad [A] = \begin{bmatrix} n & \sum I_i & \sum C_i & \sum P_i \\ \sum I_i & \sum I_i^2 & \sum I_i C_i & \sum I_i P_i \\ \sum C_i & \sum C_i I_i & \sum C_i^2 & \sum C_i P_i \\ \sum P_i & \sum P_i I_i & \sum P_i C_i & \sum P_i^2 \end{bmatrix}$$

$$\bar{b} = \begin{pmatrix} \sum F_i \\ \sum F_i I_i \\ \sum F_i C_i \\ \sum F_i P_i \end{pmatrix}$$

By the same procedure that is shown above, the linear relationship between the related variables is:

Table 1 Resistance spot welder (TECNA-8106) Specifications

Specification	Value	Specification	Value
Supply Voltage	380 V	Phases	1
Frequency	50 Hz	Max. welding Power	810 kVA
Nominal power at 50%	250 kVA	Max. welding current	68 kA
Max. welding force	18.85 kN	Electrode force per 1 bar	3.14 kN
Supply pressure	6.5 bar	Water cooling	12 ℓ / min
Throat depth	250 mm	Net weight	1000 kg

Table 2 Strip material specifications

Trade name	Thickness (mm)	Tensile (MPa)	Hardness (HV)	Nominal composition (wt-%)				
				Fe	Si	Mn	Others	Al
1050A	0.6	105	30	0.255	0.173	0.021	0.051	99.5
1050A	1.0	105	30	0.378	0.100	0.018	0.004	99.5
1050A	1.5	127	45	0.350	0.070	0.010	0.070	99.5

Table 3 Experiments setup (factors and their associated values)

Factors	Values	Units
Sheets thicknesses	0.6, 1.0, 1.5	mm
Current (RMS)	10 ~ 30	kA
Welding time	1 ~ 13	cycle
Electrode force	1.75 ~ 4.00	kN

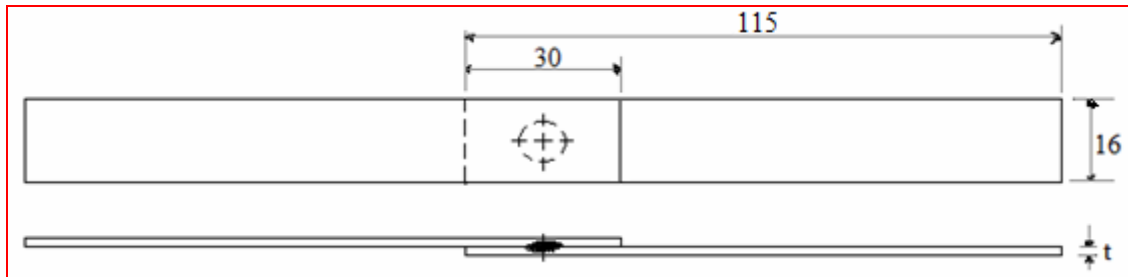


Fig. 1 Schematic illustration of tensile test specimen

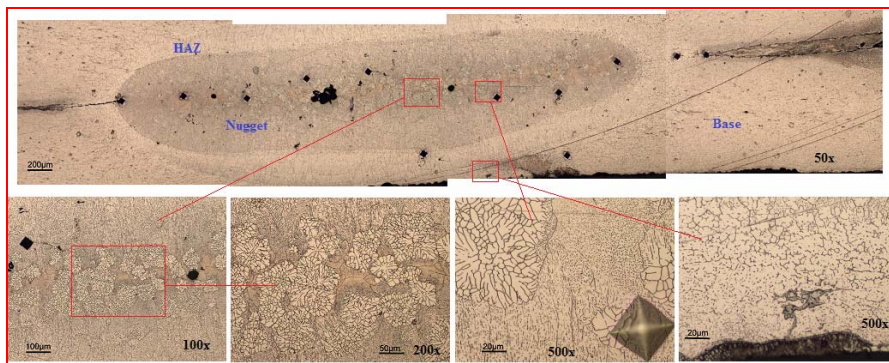


Fig. 2 Micrographs of RSW of 1.0 mm sheet, welding parameters (29 kA, 5 cycles)

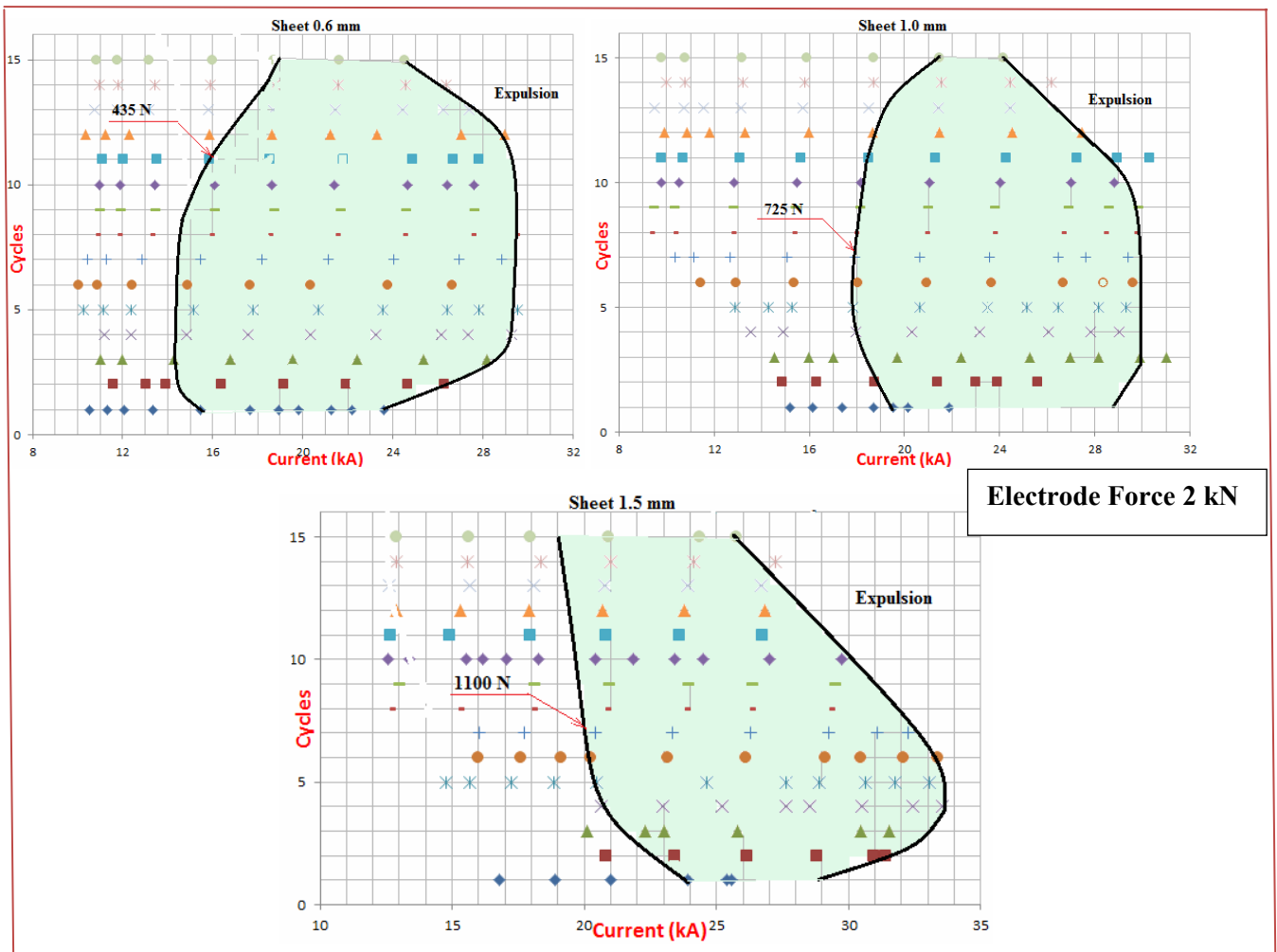


Fig. 3 Weld current-Weld time lobe diagram

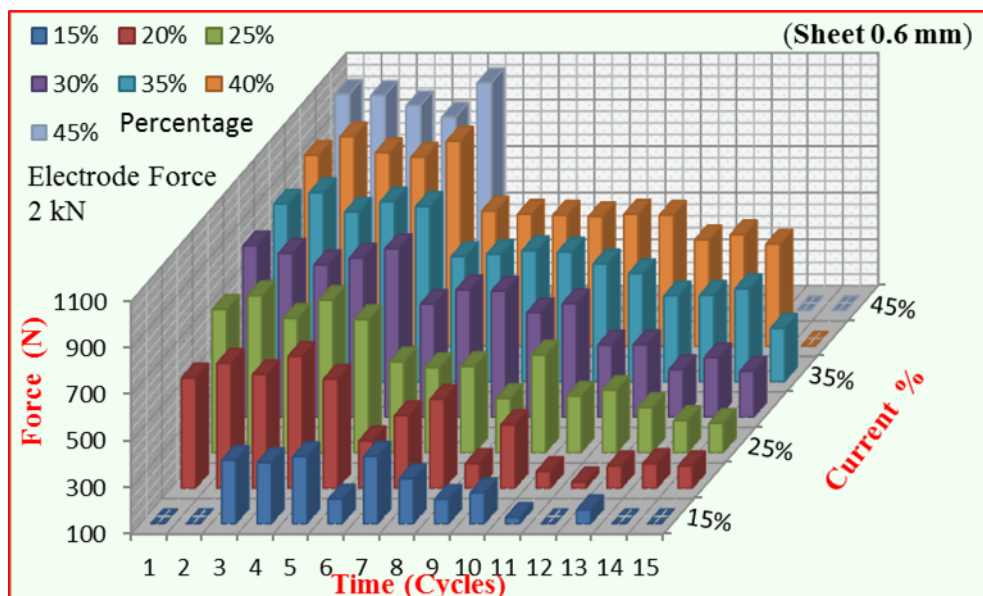


Fig. 4 The relationship between the shear tensile strength and the RSW parameters (0.6 mm)

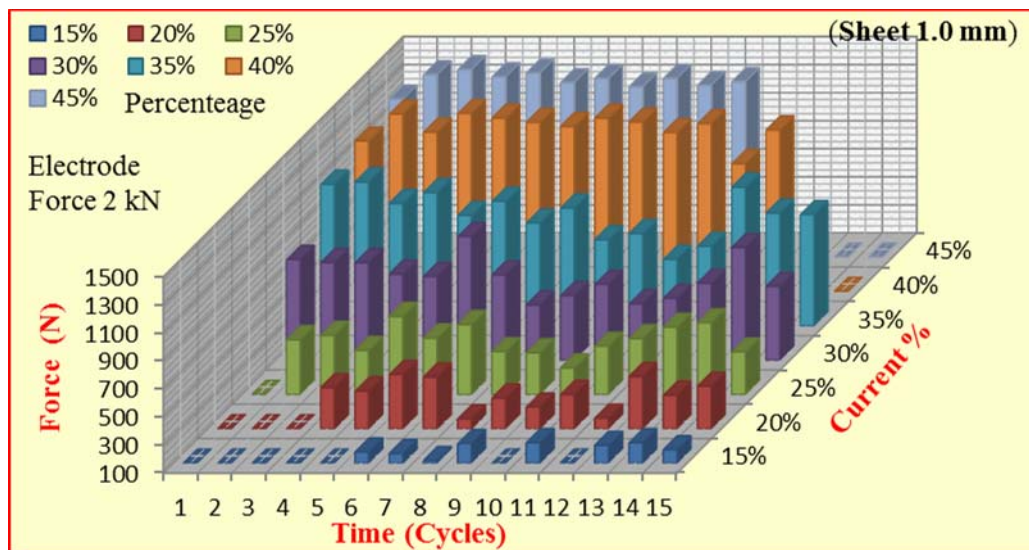


Fig. 5 The relationship between the shear tensile strength and the RSW parameters (1.0 mm)

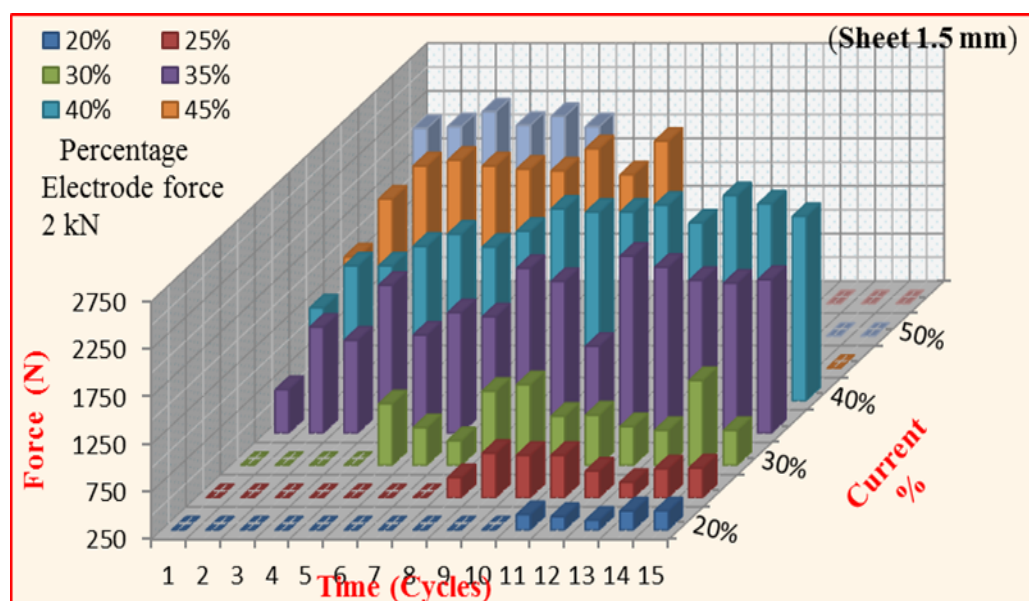


Fig. 6 The relationship between the shear tensile strength and the RSW parameters (1.5 mm)

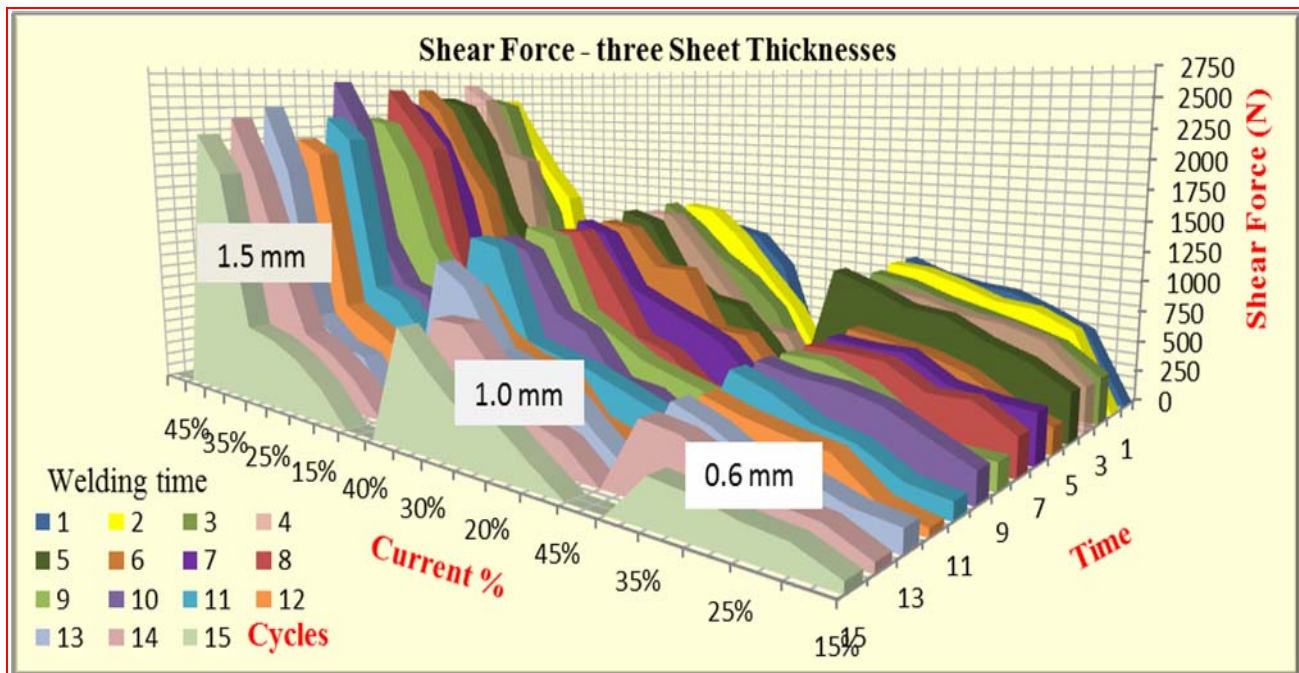


Fig. 7 The relationship between the shear tensile strength and the RSW parameters (three sheets)

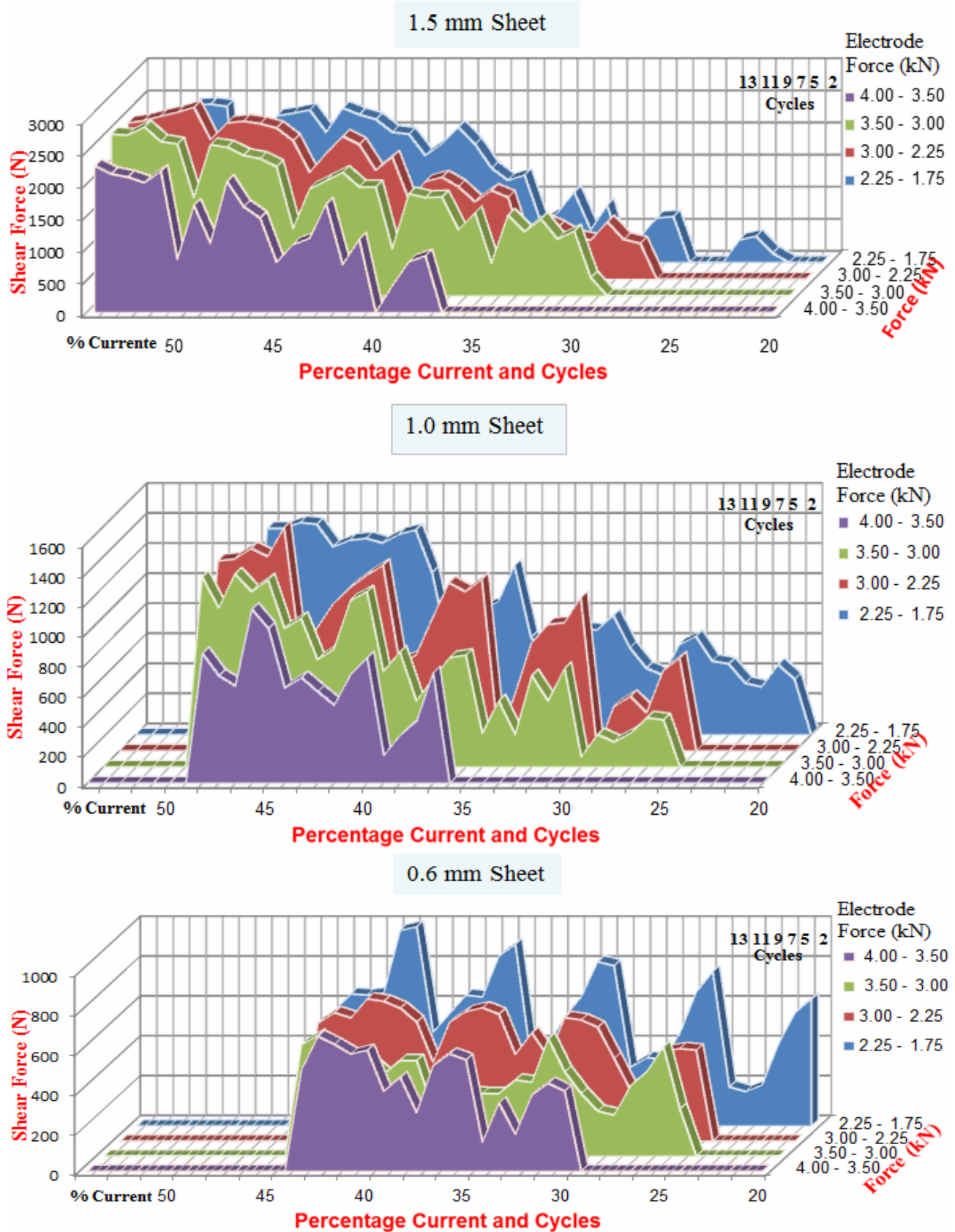


Fig. 8 The influence of the electrode forces on the shear tensile strength (three sheets).

قائمة المحتويات

:

207 - 187

سمات الهيئة الحضرية التقليدية للمدينة العربية ما بين الشكل والقيم المعنوية:
مدينة الكاظمية كحالة دراسية

أ.د. صبا جبار نعمة الخفاجي
م.د. سحر باسل محمود القيسي

232 - 208

استخدام نظم المعلومات الجغرافية لإنشاء قاعدة بيانات لإدارة المشاريع
في محافظة بغداد (الرصافة)

الدكتور سوسن رشيد محمد
أياد عبد الأمير